

RATIONAL MOLECULAR DESIGN ENABLES EFFICIENT ORGANIC  
SOLAR CELLS AND ORGANIC LIGHT EMITTING DEVICES

A THESIS SUBMITTED TO  
THE GRADUATE SCHOOL OF NATURAL AND APPLIED SCIENCES  
OF  
MIDDLE EAST TECHNICAL UNIVERSITY

BY

EDA ALEMDAR YILMAZ

IN PARTIAL FULFILLMENT OF THE REQUIREMENTS  
FOR  
THE DEGREE OF DOCTOR OF PHILOSOPHY  
IN  
CHEMISTRY

DECEMBER 2022



Approval of the thesis:

**RATIONAL MOLECULAR DESIGN ENABLES EFFICIENT ORGANIC  
SOLAR CELLS AND ORGANIC LIGHT EMITTING DEVICES**  
submitted by **EDA ALEMDAR YILMAZ** in partial fulfillment of the  
requirements for the degree of **Doctor of Philosophy in Chemistry, Middle East  
Technical University** by,

Prof. Dr. Halil Kalıpçılar  
Dean, Graduate School of **Natural and Applied Sciences**

Prof. Dr. Özdemir Doğan  
Head of the Department, **Chemistry**

Prof. Dr. Ali Çırpan  
Supervisor, **Chemistry, METU**

Prof. Dr. Levent Toppare  
Co-Supervisor, **Chemistry, METU**

**Examining Committee Members:**

Prof. Dr. Atilla Cihaner  
Chemical Engineering, Atılım University

Prof. Dr. Ali Çırpan  
Chemistry, METU

Prof. Dr. İrem Erel Göktepe  
Chemistry, METU

Prof. Dr. Dilber Esra Yıldız  
Physics, Hitit University

Assist. Prof. Dr. Erol Yıldırım  
Chemistry, METU

Date: 26.12.2022

**I hereby declare that all information in this document has been obtained and presented in accordance with academic rules and ethical conduct. I also declare that, as required by these rules and conduct, I have fully cited and referenced all material and results that are not original to this work.**

Name Last name : Eda Alemdar Yılmaz

Signature :

## ABSTRACT

### **RATIONAL MOLECULAR DESIGN ENABLES EFFICIENT ORGANIC SOLAR CELLS AND ORGANIC LIGHT EMITTING DEVICES**

Alemdar Yılmaz, Eda  
Doctor of Philosophy, Chemistry  
Supervisor : Prof. Dr. Ali Çırpan  
Co-Supervisor: Prof. Dr. Levent Toppare

December 2022, 149 pages

Organic conjugated polymers and organic small molecules have great potential to meet one of the world's most critical challenges, clean energy production, in the following decades. Owing to their semiconducting properties, organic conjugated molecules are promising candidates for clean energy applications such as organic solar cells (OSCs) and organic light-emitting diodes (OLEDs) due to their low cost, lightweight, and flexibility. This study covers the rational molecular design for efficient OLEDs and OSCs.

The first chapter covers the effect of mono-fluorine substitution of benzothiadiazole and replacing the alkoxy group with alkylthienyl on the performance of bulk-heterojunction (BHJ) OSCs. Among three benzodithiophene (BDT) and thieno[3,4-*c*]pyrrole-4,6-dione (TPD) bearing random polymers, the best-performing device (P-FBDT) exhibits a power conversion efficiency (PCE) of 9.21% with a fill factor (FF) of 60%, and 15.4 mA/cm<sup>2</sup> short circuit current density ( $J_{sc}$ ). The second chapter includes the observation of thermally activated delayed fluorescence (TADF) in conjugated systems. The effect of spin orbit coupling was demonstrated with the incorporation of a Selenium atom into the donor unit. In this

study, three different OLEDs were produced using three different emitters (SeDF-G, SeDF-B, and SeDF-YG) with green, blue, and yellowish-green colors, respectively. The maximum external quantum efficiency (EQE) is 30.8%, and the maximum lumen is 17000 cd/m<sup>2</sup> with SeDF-G based TADF OLEDs. In the third part, ternary OSCs were produced by using two polymer donors (P1 and PTB7-Th) whose absorption spectra were complementary in UV-VIS in the photoactive layer. Increasing  $J_{SC}$  with increased absorption caused an increase in device efficiency.

Keywords: organic light emitting diodes, organic solar cells, ternary solar cells, thermally activated delayed fluorescence

## ÖZ

### VERİMLİ ORGANİK GÜNEŞ PİLLERİ VE ORGANİK IŞIK YAYAN CİHAZLAR İÇİN AKILCI MOLEKÜLERİN TASARIMI

Alemdar Yılmaz, Eda  
Doktora, Kimya  
Tez Yöneticisi: Prof. Dr. Ali Çırpan  
Ortak Tez Yöneticisi: Prof. Dr. Levent Toppare

Aralık 2022, 149 sayfa

Organik konjuge polimerler ve organik küçük moleküller, önümüzdeki yıllarda dünyanın en kritik zorluklarından biri olan temiz enerji üretimini karşılama konusunda büyük bir potansiyele sahiptir. Yarı iletken özellikleri nedeniyle organik konjuge moleküller, düşük maliyetli, hafif ve esnek olmaları nedeniyle organik güneş pilleri (OSC'ler) ve organik ışık yayan diyotlar (OLED'ler) gibi temiz enerji uygulamaları için umut verici adaylardır. Bu çalışma, verimli OLED'ler ve OSC'ler için akılcı moleküler tasarımı kapsar.

İlk bölüm, benzotiyadiazolün mono-flor eklenmesinin ve alkoksi grubunun alkiltienil ile değiştirilmesinin yığımsal heteroeklem (BHJ) OSC'lerin performansı üzerindeki etkisini kapsar. Random polimerler taşıyan üç benzoditiyofen (BDT) ve tieno[3,4-c]pirol-4,6-dion (TPD) arasında, en iyi performans gösteren cihaz (P-FBDT), %9,21'lik bir güç dönüştürme verimliliği (PCE) sergiler: %60'lık bir doldurma faktörü (FF) ve 15,4 mA/cm<sup>2</sup> kısa devre akım yoğunluğu (J<sub>sc</sub>). İkinci bölüm, konjuge sistemlerde termal olarak aktive edilmiş gecikmeli flüoresansın (TADF) gözlemlenmesini içerir. Spin-orbital eşleşme sabitinin etkisi, donör ünitesine Selenyum atomunun dahil edilmesiyle gösterilmiştir. Bu çalışmada,

sırasıyla yeşil, mavi ve sarımsı yeşil renklerde üç farklı ışık yayan malzemeler (SeDF-G, SeDF-B ve SeDF-YG) kullanılarak üç farklı OLED üretilmiştir. SeDF-G tabanlı TADF OLED'ler ile maksimum harici kuantum verimliliği (EQE) %30,8 ve maksimum lümen 17000 cd/m<sup>2</sup>'dir. Üçüncü bölümde, fotoaktif katmanda UV-VIS'de ışığı soğurma spektrumları tamamlayıcı olan iki polimer elektron verici (P1 ve PTB7-Th) olarak kullanılarak çok eklemli OSC'ler üretildi. Işığın daha fazla soğurulması ile artan kısa devre akım yoğunluğu (J<sub>SC</sub>), cihaz verimliliğinde bir artışa yol açmıştır.

Anahtar Kelimeler: organik ışık yayan diyotlar, organik güneş pilleri, çok eklemli güneş pilleri, termal olarak aktifleştirilmiş gecikmeli floresan



I dedicate this thesis to the women who have been denied the opportunity to pursue education, in the hope that it may serve as a reminder of the importance of access to education for all and inspire efforts to break down the barriers that prevent girls and women from reaching their full potential.

## ACKNOWLEDGMENTS

Before anything else, I would like to thank my supervisor, Prof. Dr. Ali Çırpan, for always supporting me, believing in me, always listening, and making me feel like a member of the family. I feel extremely lucky to have such a wise, creative, and supportive advisor. PhD is a lengthy process, but I've always enjoyed what I've been doing throughout it. I thank Prof. Dr. Levent Toppare for his support and trust in me, it has been a great privilege to have him as my co-advisor and I am honored to have had the opportunity to work with him.

I would like to express my gratefulness to the members of the thesis monitoring committee, Prof. Dr. İrem Erel Göktepe and Prof. Dr. Atilla Cihaner for their valuable contributions, comments, and guidance that enlightened my horizons in this process.

I would like to thank Assoc. Prof. Görkem Günbaş for his creative ideas, inspiration, and sincere guidance. We performed an excellent job thanks to the well-thought-out design of the small molecules synthesized in the second chapter.

I would like to express my gratitude to Assist. Prof. Dr. Erol Yıldırım, my committee members, who contributed value to the research and widened our perspectives via his theoretical studies, and Prof. Esra Dilber Yıldız for valuable contributions. I am incredibly grateful for their assistance, time, and critical insight throughout the completion of my thesis.

I would like to thank Assist. Prof. Dr. Şevki Can Cevher, Duygu Cevher, Soner Öztürk, and Tuğba Haciefendioğlu for their help in the molecules synthesized and characterizations within the scope of this thesis. I would like to express my gratitude to Assoc. Prof. Dr. Murat Aydemir, Dr. Andrew Danos and Prof. Dr. Andrew Monkman for the photophysical studies in the thesis.

My beloved friend Gizem Atakan, who stayed by me through difficult times, never withheld her support, and inspired me with her talents, should not be forgotten. I

am incredibly lucky to have you as a friend; all obstacles are easily solved as long as you have friends that assist you in the process. Thank you for always being with me.

I would like to express my deepest gratitude to Dr. Gönül Hızalan and Mert Can Erer for their unwavering support and guidance throughout my journey. They have taught me everything I know and made laboratory work and experimentation not only manageable, but enjoyable. Their passion for their field and dedication to teaching is truly inspiring and I am forever grateful for their guidance. Additionally, I could not have made it through this journey without the constant support of my friends Parisa Sharif, Mustafa Yaşa, Elif Demirgezer and Ümran Işıl Biçer. They have been my rock, providing both emotional and practical support, and I am incredibly grateful for their friendship. I truly believe that the support and encouragement of these individuals has been instrumental in my success and I am incredibly grateful for all that they have done for me.

I want to express my deepest gratitude to Umut from the bottom of my heart. He has always been my biggest supporter, standing by me through every step of my journey. His unwavering support has been a constant source of strength for me, and I am so grateful to have him in my life. It's a great comfort to know that I can always count on him to be there for me, no matter what. He has been an incredible partner, and I feel incredibly lucky to have him in my life. Thank you for always being by my side and for supporting me in every way possible. Your love and support mean the world to me.

I would like to take this opportunity to express my deepest gratitude to my family for their love and support throughout my doctoral journey and instilling a love of learning in me. Their faith in me has been a constant source of inspiration and motivation. Their dedication and understanding allowed me to focus on my studies and research.

## TABLE OF CONTENTS

ABSTRACT .....	v
ÖZ.....	vii
ACKNOWLEDGMENTS .....	x
TABLE OF CONTENTS .....	xii
LIST OF TABLES .....	xvii
LIST OF FIGURES .....	xix
LIST OF ABBREVIATIONS .....	xxiii
CHAPTERS	
1 INTRODUCTION.....	1
1.1 Organic Optoelectronics for Renewable Energy .....	1
1.2 The Necessity of Using Renewable Energy .....	3
1.3 Organic Semiconductors.....	4
1.3.1 Conjugated Polymers.....	5
1.3.2 Conjugated Organic Small Molecules.....	8
1.4 Organic Solar Cells.....	11
1.4.1 History of Organic Solar Cells .....	11
1.4.2 Organic Solar Cells - Today and Tomorrow .....	11
1.4.3 Solar Cell Generations.....	14
1.4.3.1 First Generation Cells .....	14
1.4.3.2 Second Generation Cells .....	15

1.4.3.3	Third Generation.....	15
1.5	Organic Polymer Solar Cells.....	15
1.5.1	Binary Organic Solar Cells .....	17
1.5.2	Tandem Organic Solar Cells.....	19
1.5.3	Ternary Organic Solar Cells .....	19
1.5.4	Working Principle of BHJ Organic Solar Cells.....	20
1.5.4.1	Light Absorption and Exciton Formation.....	21
1.5.4.2	Exciton Diffusion and Charge Separation at the Donor/Acceptor interface .....	24
1.5.4.3	Charge Transport in the Donor and Acceptor Phases.....	25
1.5.4.4	Charge Collection at the Electrodes .....	27
1.5.5	Photovoltaic Characteristics of a Solar Cell .....	27
1.5.5.1	Power Conversion Efficiency (PCE).....	27
1.5.5.2	Short Circuit Current Density ( $J_{SC}$ ) .....	29
1.5.5.3	Open Circuit Voltage ( $V_{OC}$ ).....	29
1.5.5.4	Fill Factor.....	30
1.5.5.5	External Quantum Efficiency (EQE).....	30
1.5.6	Effect of Imbalance of Mobility and Traps on the Device Performance .....	31
1.5.7	Challenges of Organic Solar Cells.....	32
1.6	Organic Light Emitting Diodes (OLEDs).....	33
1.6.1	Emitter Generations .....	34
1.6.1.1	Design of TADF Molecules.....	36
1.6.2	Working Principle of TADF OLEDs.....	37

1.6.3	Measuring the efficiency of OLEDs.....	39
1.6.4	Challenges of OLEDs.....	41
2	EXPERIMENTAL .....	43
2.1	Materials .....	43
2.2	Solar Cell Fabrication .....	44
2.3	TADF OLED Fabrication .....	46
2.4	Characterizations .....	48
2.4.1	UV-VIS Spectroscopy .....	48
2.4.2	Photoluminescence Spectroscopy .....	48
2.4.3	Time-Resolved Photoluminescence .....	49
2.4.4	Cyclic Voltammetry .....	49
2.4.5	Atomic Force Microscopy .....	50
2.4.6	Transmission Electron Microscopy .....	50
2.4.7	OSC Characterization .....	50
2.4.8	OLED Characterization .....	51
3	AIM OF THE THESIS .....	53
4	EFFECT OF FLUORINATION STRATEGY AND SIDE CHAIN ENGINEERING .....	55
4.1	Introduction.....	55
4.2	Experimental.....	57
4.2.1	Synthesis.....	57
4.2.2	Device Fabrication.....	60
4.3	Results and Discussion .....	61
4.3.1	Characterization of Optical and Electronic Properties .....	61

4.3.2	Photovoltaic Properties .....	64
4.3.3	Morphological Studies .....	71
4.4	Conclusion.....	74
5	RATIONAL MOLECULAR DESIGN ENABLES EFFICIENT BLUE TADF-OLEDS WITH FLEXIBLE GRAPHENE SUBSTRATE.....	75
5.1	Introduction .....	75
5.2	Experimental .....	76
5.2.1	Molecular Design of TADF Molecules .....	76
5.3	Results and Discussion.....	79
5.3.1	Optical and Photoluminescence Properties.....	79
5.3.2	Computational Studies .....	85
5.3.3	Fabrication and Characterizations of TADF OLEDs.....	89
5.4	Conclusion.....	96
6	TWO COMPATIBLE POLYMER DONORS ENABLING HIGH EFFICIENCY TERNARY ORGANIC SOLAR CELLS .....	97
6.1	Introduction .....	97
6.2	Experimental .....	99
6.2.1	Optical Properties.....	99
6.2.2	Device Fabrication and Characterization.....	101
6.3	Results and Discussion.....	102
6.4	Conclusion.....	105
7	CONCLUSIONS.....	107
8	OUTLOOK .....	109
	REFERENCES .....	111

## APPENDICES

A. Synthesis, Materials and Characterization .....	125
B. Computational Studies.....	129
C. Device Fabrication and Characterization .....	135
Device Performance .....	136
D. NMR Spectra .....	137
CURRICULUM VITAE .....	147



## LIST OF TABLES

### TABLES

Table 4.1 Summary of electrochemical and optical studies of P-HTBDT, P-FBDT and P-FTBDT.....	64
Table 4.2 Photovoltaic properties of fabricated solar cells.....	66
Table 5.1 Decay parameters $k_f$ , $k_{ISC}$ , $k_{rISC}$ and lifetimes from kinetic fitting of decays.....	82
Table 5.2 The electrical and structural characteristics of SeDF-G, SeDF-B, and SeDF-YG, as well as the influence of phenoxazine (ODF) and phenothiazine (SDF) replacements, as calculated by DFT. Calculations for dipole and polarizability are expressed in Debye and a.u., respectively. In parentheses are calculations based on the Perdew–Burke–Ernzerhof (PBE0) functional.....	86

The second contribution provided by the heavy atom effect is sourced from electronic effects. The percentage of HOMO on the acceptor center increases, while percentage of the LUMO on the acceptor decreases with the heavy atom effect. Dipole moment, polarizability and hyperpolarizability increase generally in the order of O, S, Se. Positive atomic charges based on the electrostatic potential fitting is increased on the acceptor center and negative charge on the donor that means stronger electron density donating potential by sulfur and selenium substitution. The most significant enhancement is improvement in theoretically calculated  $k_{RISC}$  especially for the equatorial conformation of the phenothiazine and phenoselenazine substituted TADF materials determined for different  $\lambda_M$  values for  $T_1 \rightarrow S_1$  transition. The origin of this enhancement is determined mainly as the enhancement of  $H_{SO}$ , spin orbit coupling matrix element, that show more than tenfold increase by the replacement of O with Se atom.<sup>130</sup> Our results presented that structures only with equatorial conformations show significant improvement for  $k_{RISC}$  leading to the TADF properties (Table 5.3).  $k_{RISC}$  is significantly lower for the more stable axial conformations. This indicates multi-conformational structure by heavy atom substitution leading to the classical fluorescence by axial

conformations and TADF type emission by equatorial conformations that enhance EQE. Although percentage of the equatorial conformation responsible for the TADF properties decreases by PSeZ substitution, the efficiency is much higher due to the tremendous enhancement in the spin orbit coupling and dual emission by energy transfer between conformations. Table 5.3  $k_{\text{RISC}}$  for  $T_1 \rightarrow S_1$  transitions and the  $\Delta E_{S_1-T_1}$  and  $H_{\text{SO}}$  parameters used for the calculation of  $k_{\text{RISC}}$ ..... 87

Table 5.4 Summary of OLED characteristics of champion devices, (average in parenthesis ..... 91

Table 6.1 Key performance parameters of TB-OSCs comprising PTB7-Th:P1:PC<sub>71</sub>BM ..... 104

## LIST OF FIGURES

### FIGURES

Figure 1.1 Organic electronics and application regions.....	3
Figure 1.2 (a) Left to right: Hideki Shirakawa, Alan MacDiarmid and Alan Heeger and (b) powdery and silvery polyacetylene (before and after doping process) .....	7
Figure 1.3 Structures of typical conducting polymers .....	7
Figure 1.4 High efficiency small molecules employed in the field of optoelectronics <sup>21</sup> .....	10
Figure 1.5 National Renewable Energy Laboratory certified solar cell efficiency chart. Orange indicates record efficiencies for developing PV technologies (Dye cells, Perovskites, OSC, CZTS, and quantum dot solar cells) (from www.nrel.gov) .....	13
Figure 1.6 Molecular structures of P3HT and PC <sub>71</sub> BM.....	17
Figure 1.7 Structures of binary, tandem and ternary polymer solar cells .....	17
Figure 1.8 (a) bilayer heterojunction and (b) bulk heterojunction device structures .....	18
Figure 1.9 Efficiency evolution of ternary organic solar cells from 1.9% in 2009 to 18.9% in 2021. <sup>38</sup> .....	20
Figure 1.10. Schematically light absorption and exciton formation .....	21
Figure 1.11 Standard Solar Spectra (AM1.5G) for use in space and on Earth. ....	23
Figure 1.12 Schematically exciton diffusion and charge separation at the donor/acceptor interface.....	24
Figure 1.13 Schematically charge transport at the donor/acceptor interface.....	25
Figure 1.14 Schematically charge collection at the electrodes .....	27
Figure 1.15 Example of a J-V curve of a solar cell device .....	28
Figure 1.16 Typical recombination pathways in organic solar cells.....	32
Figure 1.17 Mechanism of 1 <sup>st</sup> , 2 <sup>nd</sup> and 3 <sup>rd</sup> Generation OLEDs, respectively. ....	36
Figure 1.18 Device architecture and working principle of OLEDs .....	37
Figure 1.19 Host-Guest mechanism for TADF OLEDs .....	39

Figure 1.20 CIELAB (x, y, z) and Hunter L, a, b color scales .....	41
Figure 2.1 Schematic representation of the experimental sequence of solar cell fabrication.....	44
Figure 2.2 Schematic representation of the experimental sequence of solar cell fabrication.....	46
Figure 4.1 Synthetic pathway of polymers.....	58
Figure 4.2 The energy level diagram of the fabricated P-HTBDT, P-FTBDT and P-FBDT based OSCs. ....	61
Figure 4.3 a) Cyclic voltammetry curves of polymers P-HTBDT, P-FTBDT and P-FBDT and b) absorption spectra of corresponding polymers (solid and thin film state) in UV-VIS region.....	62
Figure 4.4 J-V curves and EQE characteristics that summarize photovoltaic performance of P-HTBDT, P-FTBDT and P-FBDT.....	68
Figure 4.5 Natural logarithm of current density vs. light intensity characteristics for devices based on P-HTBDT, P-FTBDT and P-FBDT based OSCs.....	69
Figure 4.6 Open-circuit voltage vs. natural logarithm of light intensity characteristics for devices based on P-HTBDT, P-FTBDT and P-FBDT based OSCs.....	71
Figure 4.7 TEM images of a) P-HTBDT : PC <sub>71</sub> BM processed from <i>o</i> -dcb b) P-FTBDT :PC <sub>71</sub> BM processed from <i>o</i> -dcb with 2% DIO, c) P-FBDT :PC <sub>71</sub> BM processed from <i>o</i> -dcb d) P-HTBDT :PC <sub>71</sub> BM processed from <i>o</i> -dcb with 2% DIO e) P-FTBDT: PC <sub>71</sub> BM processed from <i>o</i> -dcb with 2% DIO f) ) P-FBDT :PC <sub>71</sub> BM processed from <i>o</i> -dcb with 6% DPE .....	72
Figure 4.8 AFM images of a) P-HTBDT :PC <sub>71</sub> BM processed from <i>o</i> -dcb b) P-FTBDT :PC <sub>71</sub> BM processed from <i>o</i> -dcb with 2% DIO, c) P-FBDT :PC <sub>71</sub> BM processed from <i>o</i> -dcb d) P-HTBDT :PC <sub>71</sub> BM processed from <i>o</i> -dcb with 2% DIO e) P-FTBDT: PC <sub>71</sub> BM processed from <i>o</i> -dcb with 2% DIO f) ) P-FBDT :PC <sub>71</sub> BM processed from <i>o</i> -dcb with 6% DPE. ....	73
Figure 5.1 Structures and the synthetic pathway of synthesized TADF molecules, SeDF-G, SeDF-B and SeDF-YG, respectively. ....	78

Figure 5.2 Luminescence images of SeDF-G, SeDF-B, and SeDF-YG in chloroform recorded under UV irradiation at  $\lambda_{ex}=365$  nm (above), normalized absorption (dashed line) and photoluminescence (PL, solid line) spectra of SeDF-G, SeDF-B and SeDF-YG in chloroform at room temperature (below)..... 79

Figure 5.3 Normalized photoluminescence spectra of Se-B, Se-G and Se-YG molecules in 10% mCBP drop-cast films at RT. Phosphorescence spectra were taken at 80 K at >80 ms delay after pulsed excitation. (above) Photoluminescence decay kinetics of the same films at RT (under vacuum) and at 80 K (under dry nitrogen). (below) ..... 81

Figure 5.4 Normalized time-resolved spectra at RT (left), with contour plots of normalized time-resolved spectra (right). The emission spectra change from Se-1LE- dominated at early times, to redshifted CT-dominated emission at later times ..... 83

Figure 5.5 The duration of applied oxygen plasma. After the oxygen plasma treatment, the substrates were transferred to the thermal evaporator, where each layer's thickness was optimized (HTL, EML and ETL). Due to its high triplet energy of 2.9 eV, aligned HOMO and LUMO energy levels, broad energy bandgap, and good morphological stability, m-CBP was chosen as the host material for all systems.<sup>132</sup> ..... 90

Figure 5.6 a) Current efficiency vs. luminance and EQE(%) vs. luminance characteristics of fabricated OLEDs, b) Current density–voltage–luminance (J–V–L) characteristics of ITO-based OLEDs. .... 92

Figure 5.7 (a) Photographs, (b) color coordinates on chromaticity diagram and (c) electroluminescence spectrum of fabricated OLEDs..... 93

Figure 5.8 Operation lifetime plot of ITO-**SeDF-G**, ITO-**SeDF-YG**, ITO-**SeDF-B**, devices. Lifetime was measured at an initial luminance of 1000 cd m<sup>-2</sup> ..... 95

Figure 6.1 UV-VIS spectra of P1, PTB7-Th and P1:PTB7-Th-PC<sub>71</sub>BM ..... 100

Figure 6.2 Structures of P1 and PTB7-Th ..... 101

Figure 6.3 Device architecture and energy level diagram of fabricated TB-OSCs ..... 102

Figure 6.4 J-V curves of PTB7-Th:PC <sub>71</sub> BM and PTB7-Th:P1:PC <sub>71</sub> BM.....	103
Figure 6.5 EQE graph for the best working device .....	104
Figure 6.6 TEM images of light-harvesting layers of PTB7-Th, P1 and PTB7-Th:P1 .....	105
Figure 6.7 AFM images of light-harvesting layers of PTB7-Th, P1 and PTB7-Th:P1 .....	105

## LIST OF ABBREVIATIONS

OSC: Organic Solar Cell

OLED: Organic Light Emitting Diode

OFET: Organic Field Effect Transistor

BHJ: Bulk Heterojunction

IEA: The International Energy Agency

SM: Small molecule

HOMO: Highest Occupied Molecular Orbital

LUMO: Lowest Unoccupied Molecular Orbital

$E_g$ : Band Gap

TADF: Thermally Activated Delayed Fluorescence

PCE: Power Conversion Efficiency

FF: Fill Factor

$V_{OC}$ : Open-Circuit Voltage

$J_{sc}$ : Short Circuit Current Density

EQE: External Quantum Efficiency

TB-OSC Ternary Organic Solar Cell

WF: Work function

IQE: Internal Quantum Efficiency

$V_{on}$ : Turn on Voltage

EL: Electroluminescence

PL: Photoluminescence

TRPL: Time Resolved Photoluminescence

ITO: Indium Tin Oxide

AFM: Atomic Force Microscopy

TEM: Transmission Electron Microscopy

IPCE: Induced Photon to Current/Charge Carrier Efficiency

PV: Photovoltaic

$\Delta E_{ST}$ : Energy gap between the S and T states

$H_{SO}$ : the spin-orbit coupling value

P3HT: poly(3-hexylthiophene-2,5-diyl)

PC<sub>71</sub>BM: [6,6]-Phenyl-C71-butyric acid methyl ester

ISC: Intersystem crossing

RISC: Reverse intersystem crossing



# CHAPTER 1

## INTRODUCTION

### 1.1 Organic Optoelectronics for Renewable Energy

Due to the multifunctionality, affordable cost, simple and solution processability, applicability on the large areas and flexibility of organic materials, the field of organic optoelectronics has seen a rise in the importance of multifunctional devices made of organic materials. This is because organic materials may be handled in several different ways. As a direct result, organic optoelectronics has produced a number of remarkable advancements. Exciting new breakthroughs in organic semiconductors with high mobility, with broad-spectrum absorption, and organic luminescent materials have enabled the construction of high-performance organic optoelectronic devices. Organic Solar Cells (OSCs),<sup>1-3</sup> and organic light-emitting diodes (OLEDs),<sup>4,5</sup> and organic field-effect transistors (OFETs)<sup>6</sup> are examples of these technologies. Organic electronics and their application areas were illustrated in Figure 1.1. Researchers in the fields of chemistry, physics, and microelectronics are making constant advancements in the creation of these devices via their collaborative efforts. Some of these technologies, such as OLEDs, are now in commercial usage. In recent years, research on integrated and multifunctional optoelectronic devices has gained popularity in response to the growing need for smaller and intelligent electronics. Optoelectronic material is usually thought to be related to the conversion of light into electrical energy in the form of current flow through semiconductors and vice versa. Organic optoelectronic materials have been studied for their optical and electronic properties since the 1910s.<sup>7</sup> In the mid-1960s, when electroluminescence in molecular crystals and conducting polymers were found, people became more interested in these kinds of materials. Indeed, interest in organic optoelectronics has exploded over the

past two decades as a result of considerable advancements in material design and purification that have led to a substantial improvement in the performance of the materials.

This thesis talks about two main types of organic semiconductors: Organic small molecules and Photoconductive polymers with advanced optoelectronic performance. Organic small molecules are promising because they can be purified easily, and their ability to form ordered structures has made it possible for charge carriers to move around quickly.<sup>8</sup> They have also been used as models for a wide range of basic studies of the movement of excitons and charge carriers. On the other hand, polymers are favorable for making large-area devices. They have made it possible to make both high-performance single-component devices and bulk heterojunction (BHJ) solar cells, which use a mix of different components with different functions.

The field of organic optoelectronics has experienced a significant growth in the past 10 years, with more than 16000 papers published on the subject in the year 2022.

Luminescence is a bright, limitless source of light in nature that has been used to meet a variety of human needs. Almost 20% of global electricity usage and 6% of global CO<sub>2</sub> emissions are attributable to lighting. The International Energy Agency (IEA) estimates that lighting accounts for around 3% of world oil demand. Unless immediate action is taken, the global energy consumption for lighting will increase by 60% by 2030.<sup>9</sup> OLEDs derived from organic materials are known to utilize significantly less energy than their inorganic counterparts, LEDs. This thesis mainly includes efficient OSCs and OLEDs, which are two types of optoelectronic devices that will help solve the problem of the rapidly rising energy demand in recent years.

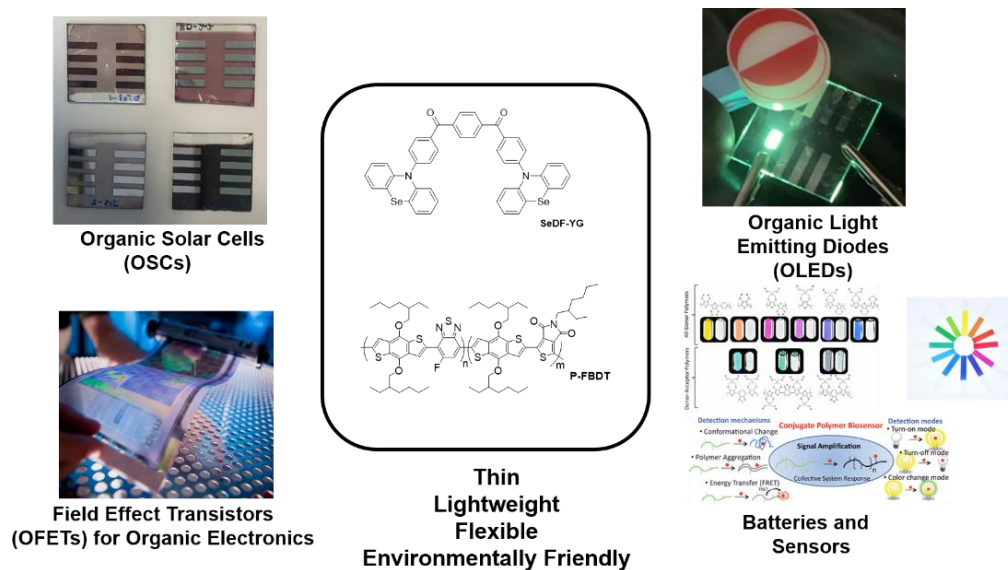


Figure 1.1 Organic electronics and application regions

## 1.2 The Necessity of Using Renewable Energy

Energy consumption has increased exponentially as a result of the fast growth of the world's population and technological progresses. Despite the fact that fossil fuels are not sustainable and cause serious environmental and health issues<sup>10,11</sup>, they remain the largest contributor to the energy industry.

Renewable energy is energy obtained from natural resources that are renewed at a rate greater than their consumption. Renewable energy sources are abundant and accessible. In contrast, fossil fuels, including coal, oil, and gas, are nonrenewable resources that need hundreds of millions of years to create. When fossil fuels are used to produce energy, they emit dangerous greenhouse gases like carbon dioxide.

Renewables are currently less expensive in the majority of countries and produce three times as many employment as fossil fuels.<sup>12</sup> Renewable energy is the energy obtained from an natural source. The proper usage of renewable energy resources (solar, bioenergy, wind, hydropower, ocean and geothermal energy) is currently a topic of heated dispute. It is crucial to decide which

energy source should be utilized with rational reasoning. The majority of aspects, including environmental impact, cleanliness, stability, effectiveness, and, affordability must be considered. It is an unfortunate reality that many sectors worldwide continue to rely on fossil fuels for energy generation. Without a doubt, these fuels are highly successful in terms of power generation quality, however they are not favorable in the long term. Fossil fuels will eventually run out; thus industry must quickly transition to sustainable energy sources. Furthermore, these fossil fuels constitute a significant danger to environmental equilibrium and are the source of several ecological risks.

The most important characteristic of renewable energy is its abundance. It is limitless. Renewable energy sources are clean energy sources that have a far smaller negative impact on the environment than traditional fossil energy technologies. The majority of renewable energy investments is spent on the construction and maintenance of facilities, rather than on expensive energy imports.

### **1.3 Organic Semiconductors**

On the basis of their molecular weight, known organic semiconductors may be roughly categorized into two groups: conjugated polycyclic compounds with a molecular weight less than 1000 and polymers with a molecular weight larger than 1000. As the primary classes of organic semiconducting materials, conjugated polymers and small molecules enable the fabrication of flexible and inexpensive electronic devices. Polymers are advantageous for usage in semiconductors due to their ability to generate thin films with a high surface area. Researchers are investigating the use of small molecules as semiconductors, despite their low solubility in organic solvents and loss of mobility upon functionalization to improve solubility. An advantage of using small molecules is that charge transfer may be more easily controlled by altering substituents. In contrast to polymeric semiconductors, the ability of these molecules to pack into well-organized polycrystalline films results in greater mobility. Small molecules, however, exhibit

more crystallinity than polymers and produce excessively large crystalline domains, which are unfavorable to charge separation.<sup>13</sup>

Organic electronics are currently competitive with conventional technologies and are contributing to meeting the demands of industry, the consumer market, and society in a variety of disciplines, including photovoltaics, information processing, data storage, display technologies, solid-state lighting, and semiconductor devices.

### 1.3.1 Conjugated Polymers

One of the first studies revealing photophysical effects and band like structures of an organic material was published in 1946<sup>14</sup>, in which it was shown that illumination improved the light driven conductivity of colored protein films. It was claimed in 1948 that  $\pi$  -  $\pi$  stacking (overlap of  $\pi$ -orbitals) between nearby molecules would generate crystals with band-like electrical behavior, similar to that of inorganic semiconductors<sup>15</sup>. In 1954, it was shown that conjugated polymers may be doped and that the polymer conjugation length is crucial for optimum conductivity<sup>16</sup>. In 1977, it was discovered that polymers could be doped to the point that they acted like conductors; as recently as the mid-1970s, everyone assumed that polymers acted as insulators. Then, in a stroke of luck, Shirakawa introduced too much catalyst to a batch of a plastic called polyacetylene that he was producing. The result of this procedure was a silvery film made from the previously powdery polyacetylene. Shirakawa, MacDiarmid, and Heeger wasted no time in altering and testing the polymers after making this discovery. They found that by adding more charges to the polyacetylene, the conductivity could be raised by a factor of 12 million. This finding hastened the development of organic electronics. The Nobel Prize in Chemistry was awarded for this discovery in 2000.<sup>17</sup>(Figure 1.2)

A polymer is a material or substance composed of macromolecules, which are large molecules that consist up of several repeating subunits. In order for a polymer to be electrically conductive, it must imitate a metal, meaning that its electrons must be

free to migrate. The first criteria is that the polymer consists of conjugated double bonds, which are single and double bonds that alternate.

Having conjugated double bonds is not sufficient, though. Plastic must be altered to become electrically conductive, either by taking electrons from (oxidation) or adding them to (reduction) the material. The term for this practice is doping. The pieces cannot move unless at least one "hole" is empty. Each fragment of the polymer is an electron that jumps to a vacancy left by another. This results in a flow of electricity along the molecule. When an external voltage is applied, an electric current occurs from the ordered movement of charges in a material as a consequence of forces acting upon them. Positive charges migrate in the direction of the applied electric field, whereas negative charges flow in the opposite direction. In the majority of materials, the flow of electrons results in a current known as electrical conduction.

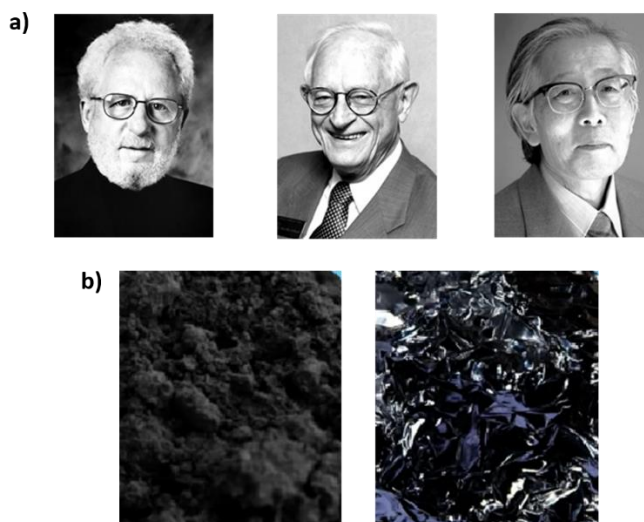


Figure 1.2 (a) Left to right: Hideki Shirakawa, Alan MacDiarmid and Alan Heeger and (b) powdery and silvery polyacetylene (before and after doping process)

The electrical and optical properties of a conjugated carbon chain are determined by its highly delocalized, polarized, electron-dense  $\pi$  bonds. Polyacetylene (PA), polypyrrole (PPy), polyaniline (PANI), poly(para-phenylene) (PPP), polythiophene (PTH), polyfuran (PF), and polyphenylenevinylene (PPV) are typical conducting polymers. The structures of abovementioned conductive polymers are listed in Figure 1.3.

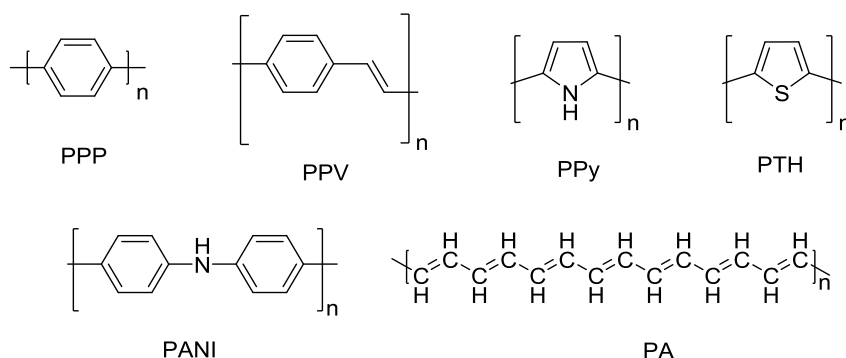


Figure 1.3 Structures of typical conducting polymers

### 1.3.2 Conjugated Organic Small Molecules

Polymer donors with polymer acceptors (all-polymer OSCs), polymer donors with small-molecule (SM) acceptors, SM donor with polymer acceptors, and SM donors with SM acceptors (all-SM OSCs) are the types of BHJ OSCs. Small molecules have potential benefits over polymers, including a known molecular weight, mass-scale synthesis, a defined molecular structure, simple purification, and excellent batch-to-batch repeatability.<sup>18</sup> This is promising for the future of small molecules, because the effect of a moiety in the molecular structure can be observed in more detail. However, the restricted solubility and high crystallinity of vapor-deposited small molecules makes their application in solution-processed BHJ OSCs undesirable.<sup>19</sup>

Currently, both small-molecule emitters and polymeric emitters may be used in OLEDs; however, small-molecule emitters often play a crucial function and provide active units to their polymeric counterparts; hence, it is crucial to research small-molecule emitters. One of the most important advantages of small molecules is that they can be deposited homogeneously on the substrates in thermal evaporators. New donor–acceptor compounds that combine aggregation-induced emission with delayed fluorescence are hot topics in OLED research. For thermally activated delayed fluorescence (TADF), the energy levels in the charge transfer state of a donor–acceptor molecule regulate the singlet–triplet energy gap, which may be accurately controlled for highly efficient device operation.

Recent interest in non-fullerene acceptors has grown due to the inherent drawbacks of fullerene derivatives such as fullerene-based OSCs, such as restricted tunability of absorption and energy level, expensive manufacture and purification, and poor stability. In this regard, small molecule acceptors and small molecule donors are utilized frequently in OSC fabrication.

A few examples of high-efficiency small molecules now employed in OLEDs and OSCs are shown below. (Figure 1.4) The crystallinity and crystalline packing of SM donors have been demonstrated to have a significant influence on the



development of an ideal microstructure that results in excellent power conversion efficiency in SM BHJ OSCs.<sup>20</sup> Conjugated organic small molecules are very effective for the fabrication of OLEDs because they do not require solvent drying processes and multi-layer device architecture can be easily accessible.

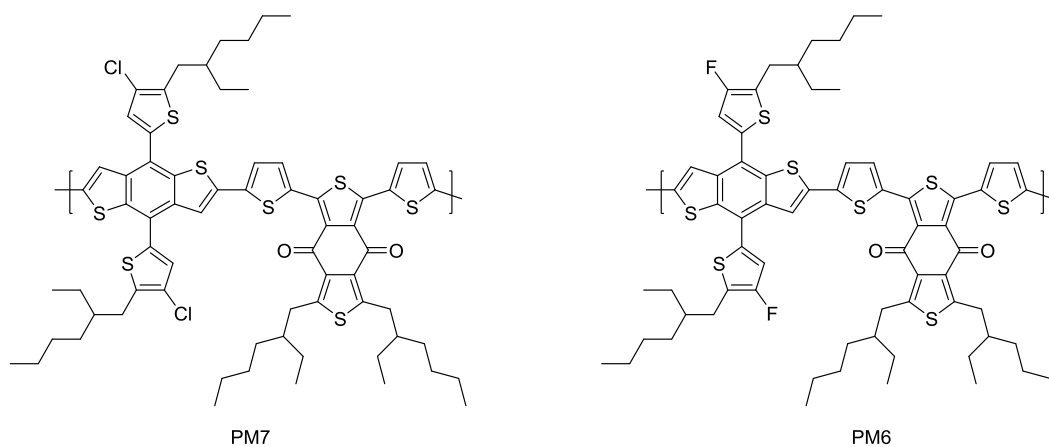
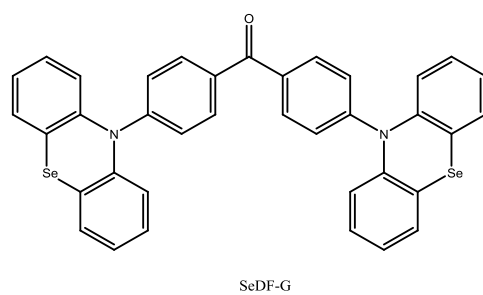
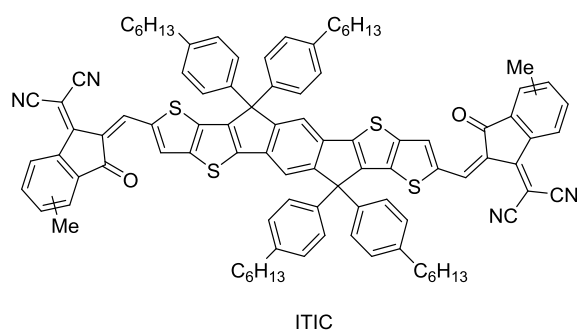
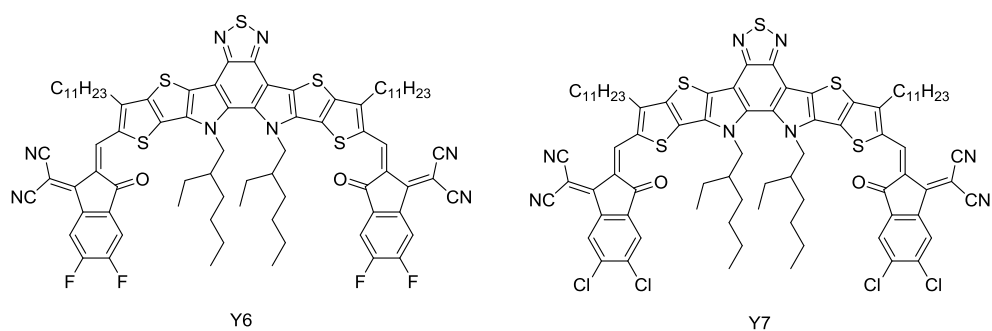


Figure 1.4 High efficiency small molecules employed in the field of optoelectronics<sup>21</sup>

## **1.4 Organic Solar Cells**

### **1.4.1 History of Organic Solar Cells**

The photovoltaic effect was originally identified in 1839 by a young French scientist named Alexandre Edmond Becquerel. He was doing electrochemical experiments when he saw this effect happening on silver and platinum electrodes exposed to sunshine. He conducted his experiment by combining silver chloride with an acidic solution and shining light on it through platinum electrodes. Consequently, it produced voltage and current. Initially, the photovoltaic effect was sometimes referred to as the "Becquerel effect". After a century, Russell Ohl developed the first modern solar cell shortly following development of the transistor. Ohl developed the "p-n junction" in 1939, which relates to the impact of impurities within electrical resistor crystals. Russell Ohl found that it was the impurities inside these crystals that made certain portions more resistive to electrical flow than others, and that it was the "barrier" between these areas of varying purity that allowed the crystal to function. Ohl subsequently discovered that super-purifying germanium was the key to producing reproducible and useable semiconductor material for diodes. Several patents were issued in the late 19<sup>th</sup> century for various solar energy inventions, leading some to believe that these individuals are the true inventors. However, early solar cells had energy conversion efficiencies of less than one percent, proving that energy could be generated from the electromagnetic radiation, but not efficiently enough for any practical application.

### **1.4.2 Organic Solar Cells - Today and Tomorrow**

Global energy consumption is increasing, while main energy sources such as fossil fuels are rapidly reducing. By producing greenhouse gases such as CO<sub>2</sub> and other air pollutants, fossil fuels also harm air quality and public health. Taking into account current economic growth projections, the globe will require 28 TW of

energy in 2050 and 46 TW in 2100.<sup>22</sup> Renewable energy should supply much of this energy. Thus, new energy sources for renewable and sustainable energy technologies must be investigated. Solar cells are the safest, cleanest, and most abundant energy source for future renewable and sustainable energy technologies, making them the most promising solutions for world energy demands.

Solar energy contributes 11.5% of the world's renewable energy. The main renewable source is now hydropower (57.7%) followed by wind (21.4%), according to the BP Renewable Energy Review. However, solar capacity is developing at a considerably greater rate than that of any other renewable energy source, suggesting that its proportion will rise in the future. If we look at the energy produced from solar energy in more detail, in 2021 about 4.4% of the total global energy came from solar energy.

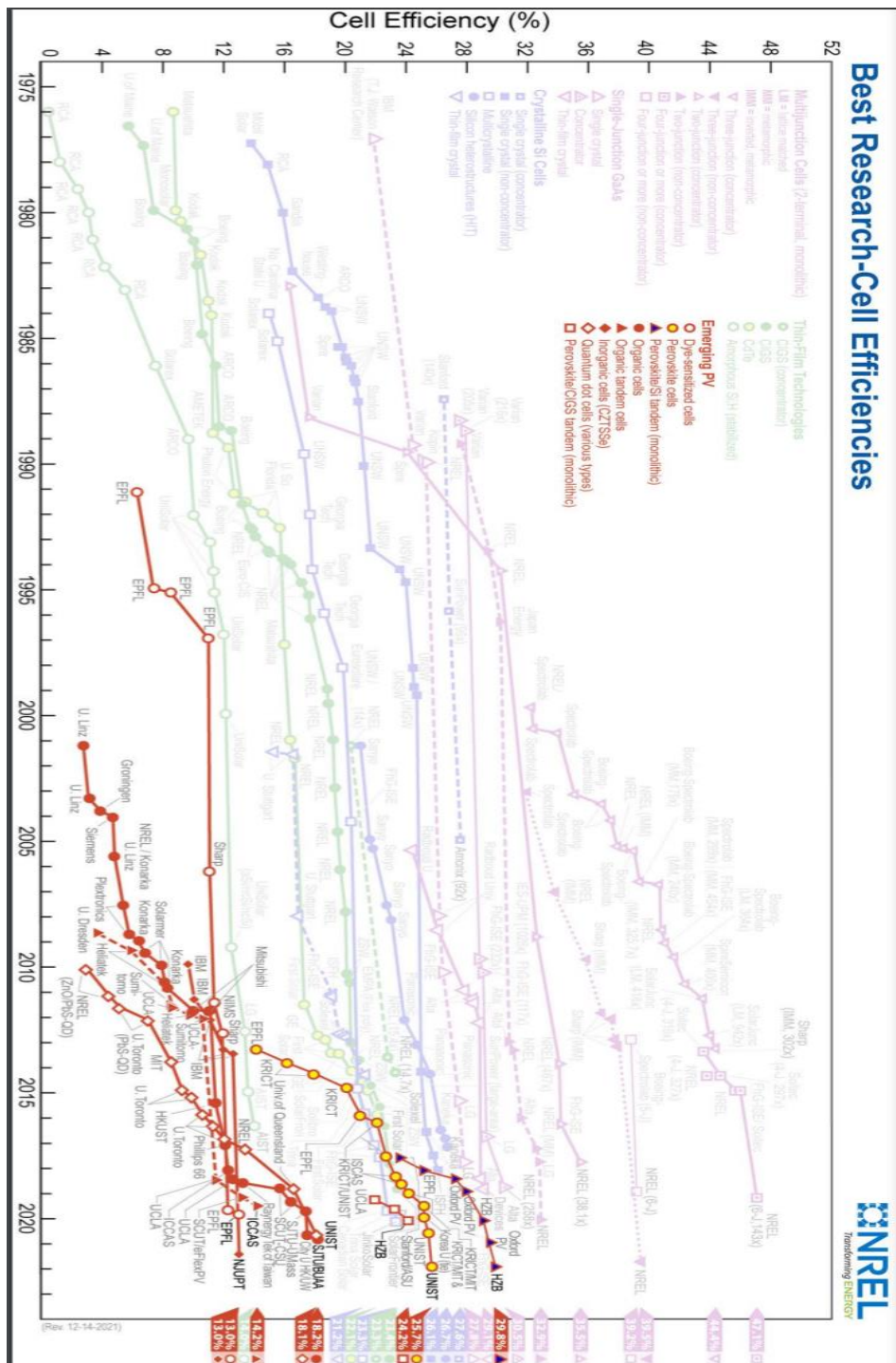


Figure 1.5 National Renewable Energy Laboratory certified solar cell efficiency chart. Orange indicates record efficiencies for developing PV technologies (Dye cells, Perovskites, OSC, CZTS, and quantum dot solar cells) (from [www.nrel.gov](http://www.nrel.gov))

A worldwide effort to increase the amount of energy that can be generated from solar cells is ongoing. The National Renewable Energy Laboratory (NREL) continually revises its chart of the most efficient solar cells. The up-to-date graph is shown in Figure 1.5. Liu et al. reported the highest power conversion efficiency (PCE) for OSCs to date as 18.2%. In the mentioned study, it was introduced quaternary devices including an extra donor PM7 and acceptor PC<sub>71</sub>BM to the PM6:Y6 donor:acceptor pair, in their paper presented in the Nature Communication in 2021.<sup>23</sup> According to the study, PM7 has a comparable molecular structure to that of PM6, but a lower HOMO energy level. Additionally, PC<sub>71</sub>BM demonstrated greater LUMO energy levels than Y6. Adding a donor and an acceptor to a device results in a stepwise alignment of energy levels and prolonged exciton diffusion periods. The study found that the mixing of PM6 and PM7 (Figure 1.4) adds to a fibrillary network and optimizes the packing of Y6 due to the differential interaction of PM7 with Y6 compared to PM6. (see Fig 1.4) It has also been found that the addition of PC<sub>71</sub>BM does not impact host morphology. In addition, the quaternary compound displayed outstanding photostability and storage stability. (After 1000 hours of illumination, the device retains 81% of its initial PCE, according to reports.) As a result, the PM6:PM7:Y6:PC<sub>71</sub>BM based quaternary device achieved an excellent PCE.

### **1.4.3 Solar Cell Generations**

#### **1.4.3.1 First Generation Cells**

This generation of solar cells consists of both single- and multi-crystalline silicon cells. These are the oldest, and Bell Laboratories introduced them. These cells are famous for their effectiveness. Solar Modules/Panels are composed of solar cells to boost their power and producing of these cells is a costly process.

### **1.4.3.2 Second Generation Cells**

Thin Film Cells, which include amorphous silicon-based thin-film solar cells, cadmium telluride/cadmium sulphide solar cells, and copper indium gallium selenide solar cells, are known as second generation cells. Their efficiency is lower than that of the first-generation cells, but they are inexpensive to manufacture. These cells are composed of consecutive layers ranging in thickness from 1 to 4  $\mu\text{m}$  and are formed on glass, polymer, or metal substrates. They are aesthetically pleasing and adaptable. Calculators employ cells made of amorphous silicon.

### **1.4.3.3 Third Generation**

The Third Generation of Cells contains exciting new and emerging technologies. The primary purpose of the generation is to develop the most efficient and cost-effective solar cells. Third generation solar cells are also searching for cells free of toxic. Polymer-based solar cells, organic–inorganic halide perovskite cells, nanocrystal-based solar cells and dye-sensitized cells are examples of third-generation cells. Research on polymer solar cells was conducted for this thesis.

## **1.5 Organic Polymer Solar Cells**

Organic polymer solar cells in which the photoactive layers are comprised of bulk-heterojunction (BHJ) blends of p-type polymer donors and n-type acceptor materials (small molecule or polymer acceptors), are potential electric utilities for flexible electronics.

In order for conjugated polymers to be utilized in OSCs, they should have low HOMO energy levels to, suitable LUMO energy levels for efficient electron transfer to the fullerene moieties, low bandgaps to increase the absorption range, and crystalline characteristics to ensure good charge mobility.

The dielectric constant measures a substance's capacity to store electrical energy in an electric field. The link between the exciton binding force and the dielectric constant "r" will be discussed in the next section. Excitons dissociate spontaneously in inorganic materials when "r" is extremely high ( $> 10$ ), however excitons are strongly linked in organic materials where "r" is very small ( $< 4$ ). Excitons diffuses in the organic semiconductor until the majority of excitons finally recombine, resulting in a very low photocurrent output.

Consequently, a different method is often utilized to separate excitons. By selecting an acceptor with an energy offset relative to donor semiconductors, it is possible to create a charge transfer state by transferring the electron from the donor to the acceptor. Most of the time, fullerenes are used as acceptors because they can accept electrons better than polymers or small molecules. On the basis of the discovery of a synthetic approach to phenyl-C<sub>61</sub>-butyric acid methyl ester, Sariciftci et al. demonstrated that charge transfer from a semiconductor polymer to buckminsterfullerene (C<sub>60</sub>) is achievable upon photon excitation in the polymer.<sup>24</sup> This material is also PCBM, a C<sub>60</sub> derivative that is solution-processable. Poly(2-methoxy, 5-(2'-ethylhexyloxy)-1,4-phenylene vinylene) (MEH-PPV) was combined with C<sub>60</sub> and its derivatives to produce the first polymer solar cell with a high power conversion efficiency of 2.9% under 20 mW/cm<sup>2</sup> light in 1995.<sup>25</sup> By far the most researched material system for organic solar cells is P3HT combined with PCBM. [6,6]-phenyl-C<sub>71</sub>-butyric acid methyl ester (PC<sub>71</sub>BM) is a fullerene electron acceptor that is often used in the most efficient organic photovoltaic systems. PC<sub>71</sub>BM's non-symmetrical C<sub>70</sub> cage permits energy transitions that are limited in C<sub>60</sub>, hence enhancing the visible solar spectrum absorption properties above PC<sub>61</sub>BM.<sup>26</sup> The molecular structures of P3HT and PC<sub>71</sub>BM were given in Figure 1.6. Polymer solar cells are composed of an electron-rich polymer donor and an electron-weak acceptor.



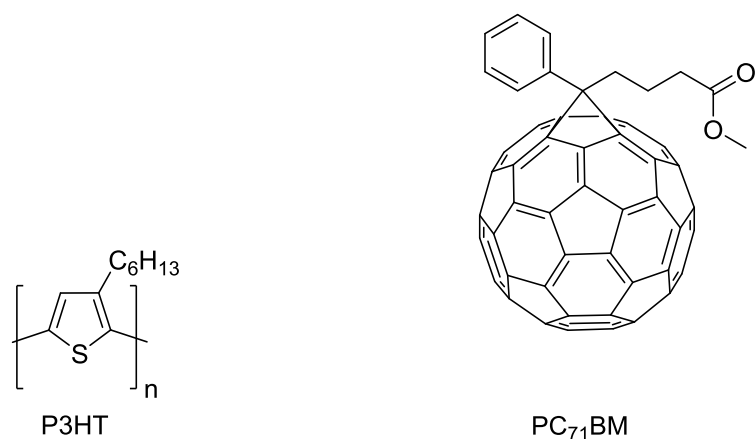


Figure 1.6 Molecular structures of P3HT and PC<sub>71</sub>BM

There are three different types of polymer solar cells described in this thesis; binary, tandem and ternary polymer solar cells. Structural differences are given in Figure 1.7.

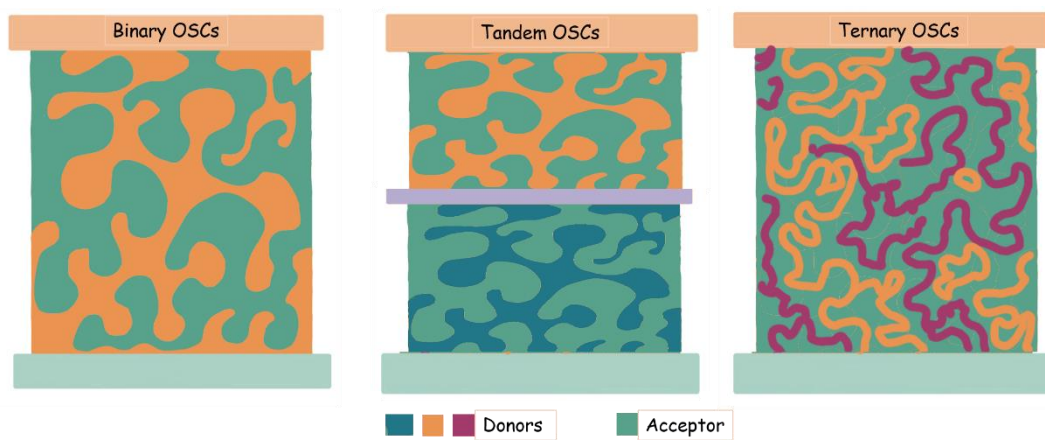


Figure 1.7 Structures of binary, tandem and ternary polymer solar cells

### 1.5.1 Binary Organic Solar Cells

As stated in the previous chapter, polymer solar cells require at least one donor and one acceptor to operate. According to the distribution of the donor and acceptor materials in the active layer, binary solar cells are classified as either bilayer or

bulk heterojunction (BHJ) solar cells. These two variations are displayed in Figure 1.8.

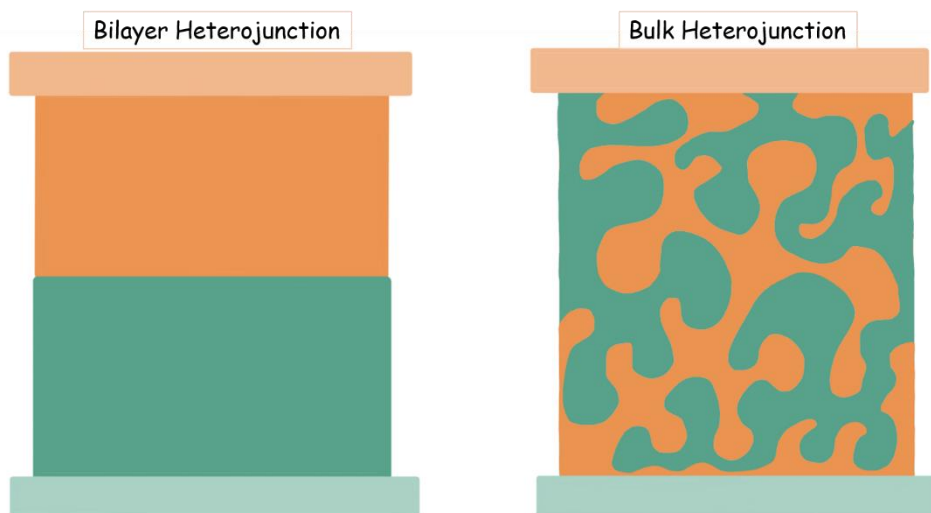


Figure 1.8 (a) bilayer heterojunction and (b) bulk heterojunction device structures

The two-layer heterojunction design is the simplest organic solar cell that uses a heterojunction. In this design, the interface between the donor and acceptor is created, and when charge carriers separate at this interface, they can move to their respective electrodes (anode and cathode). Nevertheless, such a bilayer architecture is restricted by the short exciton diffusion lengths ( $\sim 10$  nm) in polymers and the extremely narrow interface between the two materials. Therefore, in order to accomplish enhanced charge separation, the thickness of the active layer must be very thin in order to allow the majority of excitons to reach the donor-acceptor contact.<sup>27</sup> The thin active layer leads in reduced absorption and, thus, decreased device performance.

By blending the donor and acceptor molecules in the same solution, an alternate device structure is formed, and when this solution is coated as a single layer, a bulk heterojunction (BHJ) is obtained with the donor and acceptor molecules forming an interpenetrating network. The bulk heterojunction provides a very large donor/acceptor interface, enabling the free production of carriers and resulting in more efficient devices. Because this interface is long and covers the entirety of the

device, the possibility of recombination is significantly increased. To achieve high device efficiency, it is essential to extract free charge carriers as rapidly as possible. Additionally, thicker active layer can be coated to boost absorption compared to bilayer devices.<sup>28</sup>

### **1.5.2 Tandem Organic Solar Cells**

Stacking multiple photoactive layers with complementary absorption spectra in series to create a tandem OSC is an effective method for optimizing solar radiation utilization.<sup>29,30</sup> Tandem solar cells are designed to overcome limited absorption of polymers as well (by stacking components with complementary absorption), however the manufacturing process for these cells is typically more difficult than that of ternary cells.<sup>31</sup> This would obviously increase the cost, restricting their future capacity for mass manufacture. Organic tandem solar cells have reached a record efficiency of 19.6%.<sup>32</sup>

### **1.5.3 Ternary Organic Solar Cells**

In the last decade, ternary blend organic solar cells (TB-OSCs) have garnered significant interest as an elegantly alternative approach.<sup>33–35</sup> TB-OSCs generally consist of two donors and one acceptor (D1/D2/A) or one donor and two acceptors (D/A1/A2) with diverse absorption ranges in a single-junction device, which improves light harvesting capability equivalent to tandem devices but retains easy manufacturing. The ternary idea may utilize the enormous existing pool of resources to their maximum potential. The major photovoltaic properties of short circuit current density ( $J_{sc}$ ), open circuit voltage ( $V_{oc}$ ), and fill factor (FF) may be concurrently or separately enhanced by selecting the right third component and modifying its composition ratio to promote exciton dissociation, charge transfer, and blend morphological manipulation. Alternatively, device stability can be enhanced by morphological tuning.<sup>36</sup> In addition, TB-OSCs can benefit from all the techniques utilized to optimize the morphology of binary blend OSCs, including

mixed solvent, solvent additive, thermal annealing (TA), solvent vapor annealing (SVA), and hot spin-coating. With the fast advancement of donor and acceptor materials, their applications in TB-OSCs have increased PCEs to 19%, indicating a promising future.<sup>37</sup> The history of ternary organic solar cells is given in Figure 1.9.

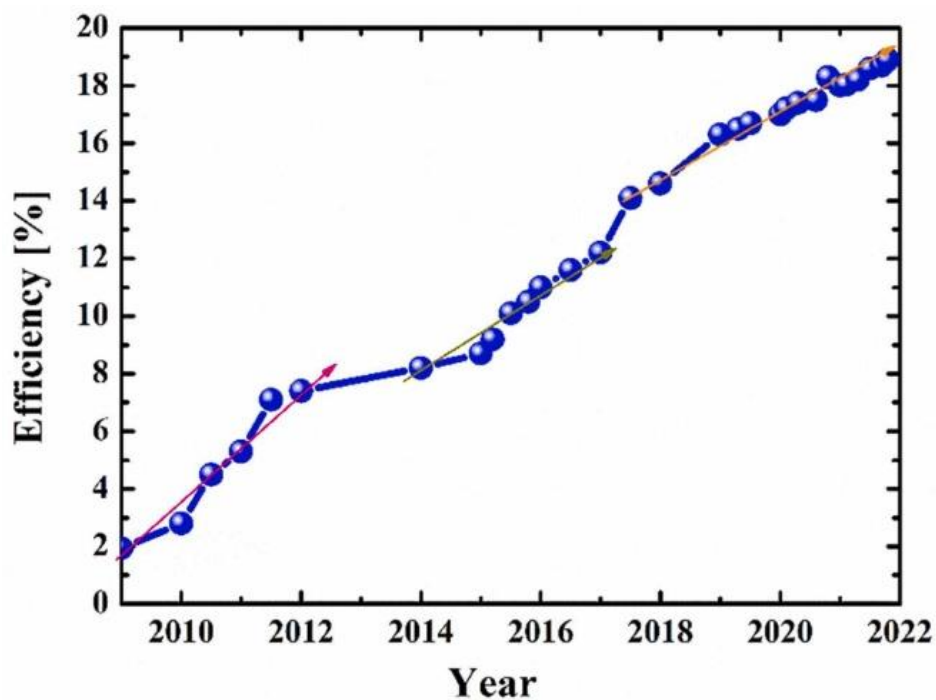


Figure 1.9 Efficiency evolution of ternary organic solar cells from 1.9% in 2009 to 18.9% in 2021.<sup>38</sup>

#### 1.5.4 Working Principle of BHJ Organic Solar Cells

Following is a summary of the stages that govern the OSC function:

### 1.5.4.1

### Light Absorption and Exciton Formation

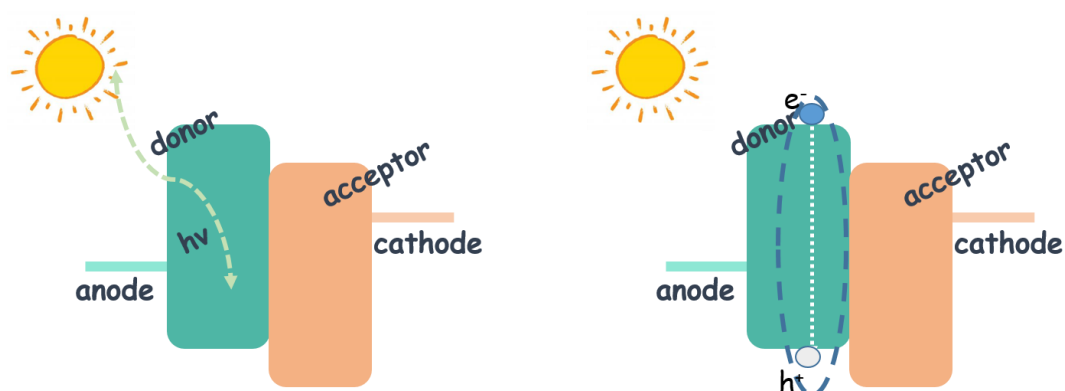


Figure 1.10. Schematically light absorption and exciton formation

To begin with, and most importantly, the photoactive layer must absorb as much sunlight as possible. Donor portion of the BHJ OSC photoactive layer typically absorbs light (Figure 1.10). Due to the high absorption coefficient of conjugated polymers, they may successfully absorb light at the maximum of their absorption spectrum with a relatively thin photoactive layer in contrast to its inorganic silicon based counterparts, which need thicknesses of hundreds of microns.

The exciton, which consists of a pair of coulombically bound electrons and holes;

- can then recombine radiatively and produce light
- can recombine non-radiatively and generate heat
- can dissociate and transform into free charge carriers that can move to their respective electrodes by generating current.

The intensity of the electric field ( $F_{e-h}$ ) between an electron and a hole determines whether an exciton dissociates spontaneously. The following is a description of the force that results from the strength of this field:

$$F_{e-h} = \frac{1}{4\pi\epsilon_r\epsilon_0} \frac{q_e q_h}{r^2}$$

$\epsilon_r$ : the dielectric constant

$\epsilon_0$ : the vacuum permittivity

$q_e$  and  $q_h$ : the electron and hole elementary charges, respectively.

$r$ : the distance between the electron and hole

The formula states that force is inversely proportional to the dielectric constant. Since the dielectric constant of inorganic materials is very high, the bonding energy between electron and hole is very weak, and excitons generally dissociate spontaneously; however, in organic materials, additional driving force is required for exciton dissociation due to the relatively low dielectric constant.

In addition, the thickness of the polymer-based photoactive layer can only be up to 100 nm due to the low charge-carrier mobilities that are present in the majority of polymers. This results in the polymers being able to absorb no more than 60% of the incident light when the absorption maximum is reached. The inorganic semiconductors, on the other hand, are able to efficiently absorb the whole visible sun spectrum. Therefore, the creation of a photocurrent in conjugated polymers is poor because of their poor absorption. Reducing the band gap of donor polymers increases light absorption, which in turn maximizes the number of photons absorbed and hence the PCEs are achieved.

The efficiency at which a solar cell absorbs light from the sun is determined by the degree to which its absorption spectrum overlaps with that of the sun's radiation (Figure 1.11). Air Mass 0 (AM0) radiation from the sun is a flux of photons

emitted with an energy distribution similar to that of a black body at 5960 K; at the Earth's surface, after passing through the atmosphere, the radiation is filtered but retains many of the same spectral features, though some wavelength regions are suppressed (Air Mass 1.5, or AM1.5).

As can be observed, about 50% of the total light output is located in the infrared area, which corresponds to the range of low energy radiations. Reducing the band gaps of semiconductors is another method for increasing absorption, since the amount of solar radiation absorbed by the active layer is dictated by the amount of overlap between the solar photons flux and the absorption coefficient summed across energies greater than  $E_g$ . Consequently, materials with a smaller band gap are required to maximize photon harvesting. For instance, a material having a band gap of less than 2 eV is regarded to have a low band gap, which can increase the efficiency of OSCs by a greater overlap with the solar spectrum. A band gap of 1.1 eV, for instance, can cover 77% of the AM1.5 sun photon flux, but a band gap of 1.9 eV can only cover 30% of the air mass 1.5 global (AM1.5 G) photon flux.<sup>39</sup>

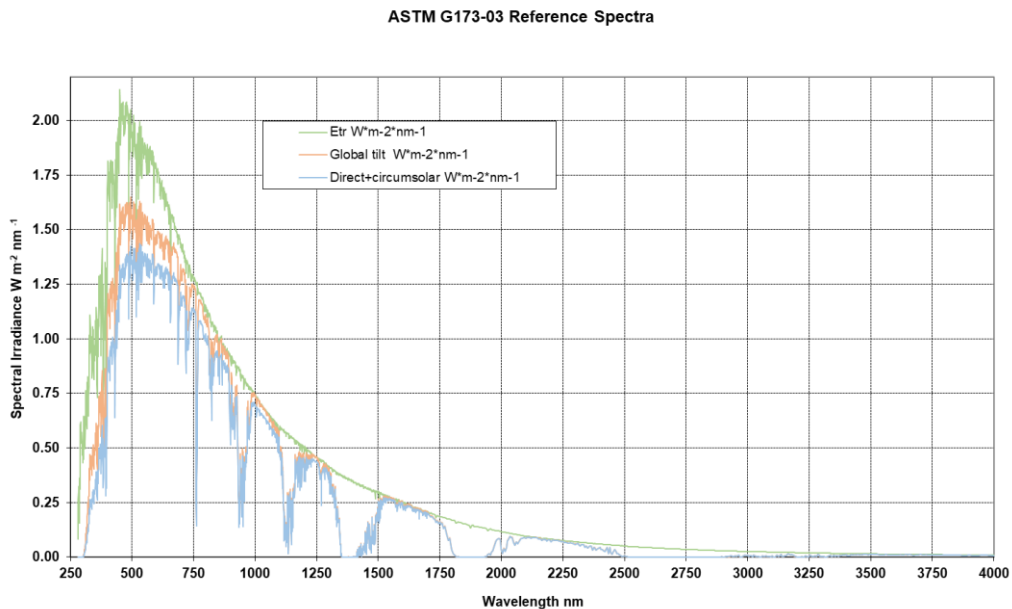


Figure 1.11 Standard Solar Spectra (AM1.5G) for use in space and on Earth.

When a photon is absorbed by the material, an electron is stimulated from the HOMO to the LUMO states when illuminated from the transparent electrode side. It is analogous to inorganic semiconductors in which electrons are stimulated from the valence band to the conduction band. A pair of electrons and holes, known as an exciton, is produced as a consequence of this process. The binding energy of excitons is typically in the range of 0.1 to 1.4 eV.

#### 1.5.4.2 Exciton Diffusion and Charge Separation at the Donor/Acceptor interface

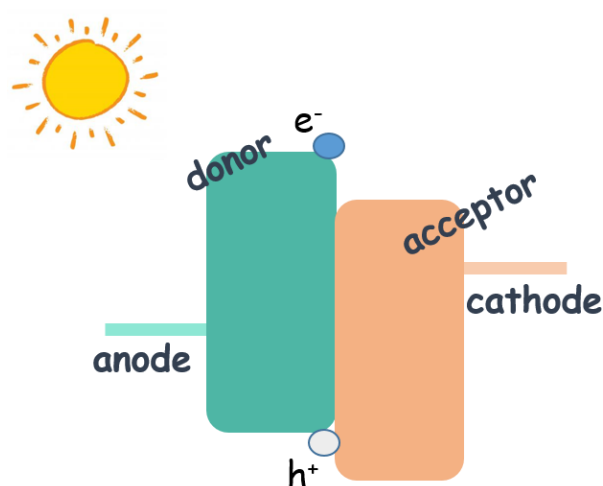


Figure 1.12 Schematically exciton diffusion and charge separation at the donor/acceptor interface

The difference in energy levels between the donor and acceptor materials in the LUMO region ultimately led the excitons to separate from one another because it breaks the Coulomb attraction. Since the excitons in the majority of conjugated polymers have a shorter lifetime, the diffusion lengths are restricted to a few nanometers (less than 20 nm), which is a significantly shorter distance than the optical absorption pass length (100–200 nm). In order to create charges in an effective manner, excitons have to be produced within their respective diffusion lengths. The distance that an exciton travels before recombining is referred to as its



"diffusion length". The reported excitons diffusion length for various conjugated polymers ranges from 5 to 20 nm. There is a large amount of variation across this range. Therefore, the depth of the photoactive layer is one of the most important factors that determines how effectively charge is generated. At the donor/acceptor interface in organic semiconductors, photogenerated holes and electrons are subjected to a high Coulomb binding energy (Figure 1.12). In order to get free charge carriers, it is necessary to separate these Coulomb-bound electron-hole pairs. When they break free of their mutual Coulomb affinity, however, they either reunite or dissociate into free charge carriers. Dissociation of excitons at the contact is crucial for fast charge transmission. Electrostatic forces are generated at the interface due to the dissimilarity in HOMO and LUMO levels of the donor and acceptor layers. Due to the electric field created by these differences, excitons are efficiently dissociated into electrons and holes when the right materials are used. The substance with a greater LUMO level accepts the free electrons, while the substance with a lower HOMO level accepts the holes. Unfortunately, on their way to the electrodes, these free charge carriers might undergo recombination or be trapped in a disordered interpenetrating organic substance.

#### 1.5.4.3 Charge Transport in the Donor and Acceptor Phases

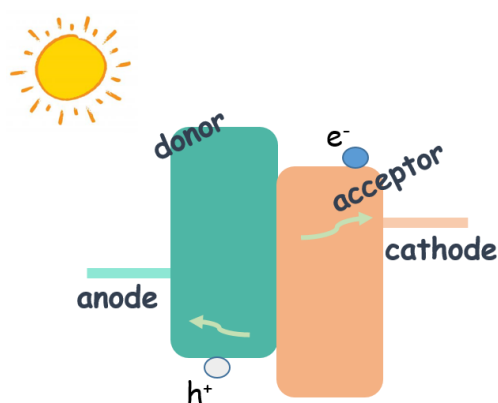


Figure 1.13 Schematically charge transport at the donor/acceptor interface

In order to reach their corresponding electrodes, the charges created when excitons dissociate into free charge carriers must first be transferred (Figure 1.13). In organic semiconductors, charge carriers often arrive from one localized state to the next. Because of the difference in Fermi levels between the electrodes, an internal electric field causes transport of free charge carriers towards the electrodes. The  $V_{OC}$  of a cell is established by the internal electric field produced by the cell's anode and cathode. Both carrier diffusion and electric field induced drift contribute to the movement of free charge carriers.

Recombination of free charge carriers in the interstitial space between the anode and cathode is the primary limiting factor in the efficiency of their passage to the electrodes. The photoactive layer's charge carrier mobility controls not only the transit of charge carriers but also the losses brought on by their recombination. For low mobility materials, the Coulomb potential continues to hold electrons and holes in place. Thus, they are unable to resist their mutual attraction and reform prior to charge collection at the electrodes. As a result, there is a drastic reduction in photocurrent generated by the solar cell. The photo-generated electrons and holes have a route length that is proportional to the thickness of the photoactive layer. Device performance degrades dramatically with increasing photoactive layer thickness due to charge carrier recombination. Therefore, the major challenges for high-efficiency devices are to overcome carrier sweep-out by the internal field and the loss of photo-generated carriers by recombination.

#### 1.5.4.4

#### Charge Collection at the Electrodes

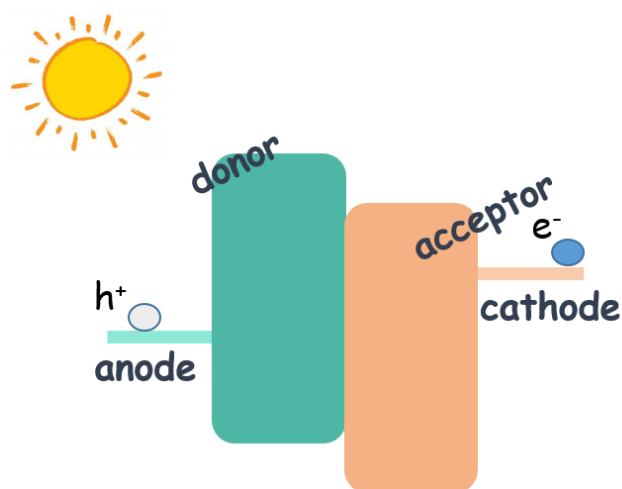


Figure 1.14 Schematically charge collection at the electrodes

Charge carriers produced by photoexcitation are removed from the photoactive layer and sent to their corresponding electrodes if they do not recombine (Figure 1.14). In order to get the most charges out of the photoactive layer, the potential barrier between the layer and the electrodes needs to be minimized. The work function (WF) of the anode should be in phase with the HOMO of the donor material, and the work function (WF) of the cathode should be in phase with the LUMO of the acceptor material. If the WFs line up as specified, the contacts are called Ohmic contacts. In contrast, no Ohmic connections would form if the donor HOMO and acceptor LUMO energies were mismatched at the anode and cathode. The efficiency of the solar cells will degrade over time.

### 1.5.5 Photovoltaic Characteristics of a Solar Cell

#### 1.5.5.1 Power Conversion Efficiency (PCE)

A solar cell's power conversion efficiency (PCE) is defined as its maximum power output divided by the total power input ( $P_{inc}$ ) from the sun. This value may be thought of as the theoretical maximum efficiency of a solar cell. However, in order

to completely comprehend the idea of PCE, it is necessary to specify a number of additional characteristics associated with the performance of a solar cell. After current-voltage evaluation of a solar cell under AM1.5G light, the PCE is determined. The PCE can be calculated with the help of the following relation using all the parameters shown in Figure 1.14.

$$PCE = \frac{FF \cdot V_{oc} \cdot J_{sc}}{P_{inc}}$$

$V_{oc}$ : the open-circuit voltage;

$J_{sc}$ : the short-circuit current density;

FF: the fill factor

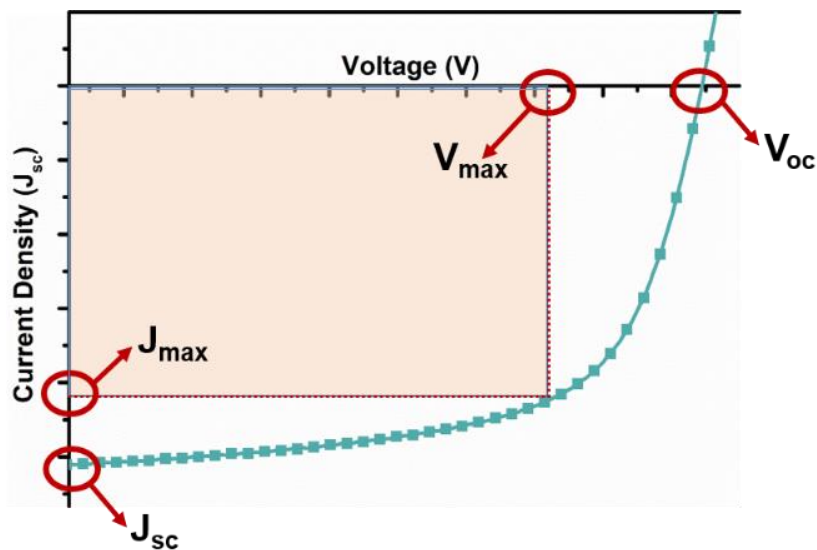


Figure 1.15 Example of a J-V curve of a solar cell device

### 1.5.5.2 Short Circuit Current Density ( $J_{sc}$ )

While there is no external voltage, this is how much current flows through a solar cell when it is exposed to sunlight. The greatest current that can flow through a device is called its short-circuit current. For any given voltage, the current density will always be lower than  $J_{sc}$ .

$J_{sc}$  is another crucial factor that impacts the effectiveness of an OPV device. By reducing the bandgap of the materials, the standard method for getting a high  $J_{sc}$  is to expand the absorption to include more solar radiation. Unfortunately, bandgap cannot be drastically reduced since  $V_{oc}$  is also affected by energy levels. Consequently, a bandgap between 1.3 and 1.8 eV is predicted. If the charges cannot reach the electrodes within the carrier life period, they will not contribute to the photocurrent.<sup>40,41</sup> In this instance, charge mobility of the material is also crucial for achieving more  $J_{sc}$ .

### 1.5.5.3 Open Circuit Voltage ( $V_{oc}$ )

The open circuit voltage is the highest voltage that the solar panel is capable of producing when there is no external voltage applied. Experimentally can be calculated and graphically it was indicated on the Figure 1.14, it is a voltage when the current density is zero.

The theoretical calculations of  $V_{oc}$  have been researched for many years, but basically it can be explained. Scharber studied a series of OSC devices<sup>42</sup> (26 polymer donor materials with different HOMO levels blended with a common acceptor) in depth in 2006 and proposed an empirical equation to express  $V_{oc}$ , where  $q$  is the elementary charge,  $E_{donor}^{HOMO}$  is the HOMO level energy of the donor, and  $E_{acceptor}^{LUMO}$  is the LUMO level energy of the acceptor. It should be emphasized that the  $V_{oc}$  loss of 0.3 eV is empirical and might be higher or less. Typically,  $V_{oc}$  is calculated by comparing the work functions of the electrodes.

However, with recently evolved OSC designs,  $V_{OC}$  levels are increased in the device architecture's interfacial layers, namely the active layer. As indicated earlier, in order to reduce losses from  $V_{OC}$ , the HOMO levels of conjugated polymers in OSCs should not be increased significantly to create a narrow band gap. Use of non-fullerene acceptors with variable LUMO levels is a further way for increasing  $V_{OC}$  in OSCs.

$$V_{OC} = (1/e)(|E_{donor}^{HOMO} - E_{acceptor}^{LUMO}|) - 0.3 V$$

#### 1.5.5.4 Fill Factor

Fill factor (FF) is the ratio of the actual maximum obtainable power to the product of short circuit current  $J_{SC}$  and open circuit voltage  $V_{OC}$ .

$$Fill\ Factor = \frac{V_{max}J_{max}}{V_{OC} \cdot J_{SC}}$$

#### 1.5.5.5 External Quantum Efficiency (EQE)

Light harvesting capacity in OSCs is represented by the external quantum efficiency (EQE) (or the incident-photon-to-converted-current efficiency, IPCE), which is the ratio of collected photogenerated charges to the number of incident photons of a particular wavelength. Notably, the peak EQE in the vast number of single-junction OSCs constructed of binary or ternary donor/acceptor bulk-heterojunction is never equal to 100% due to limited light absorption in a thin active layer and intense monomolecular and/or bimolecular charge recombination loss induced by low carrier mobility of organic materials and poor interface contact for charge collection. In this regard, boosting charge collection and light absorption become crucial factors in further improving the efficiency of OSCs.

$J_{SC}$  is an important measurable statistic for studying all existing solar cell technologies. Interpolation (for matching EQE data with AM 1.5G spectra) and

integration must be conducted precisely for this calculation to be accurate. For the calculation of  $J_{SC}$ , the EQE is measured under short circuit circumstances. Since  $J_{sc}$  may also be estimated from J-V measurements, EQE has the benefit of being independent of both the spectral structure of the light source and the cell area. In contrast to PCE, EQE measures the ratio of the number of extracted electrons and holes to the total photon flux incident on the device. In the case of internal quantum efficiency (IQE), the amount of light absorbed by the semiconductor layer at certain wavelengths is measured.

$$EQE = \frac{\text{excitons}}{\text{photons}}$$

$$IQE = \frac{\text{excitons}}{\text{absorbed photons}}$$

### 1.5.6 Effect of Imbalance of Mobility and Traps on the Device Performance

The  $J_{SC}$ , and the FF, are the organic solar cell parameters that are most heavily impacted by the magnitude and imbalance of the mobilities. There will be a significant effect brought about by the competition between non-geminate recombination and the collection of free charge carriers. (Figure 1.15) For instance, if the electron and hole mobilities of the material to form the active layer are too limited, recombination will take place over charge collection. Likewise, if there is a significant imbalance in the charge carrier mobilities of the materials, this will result in space charge build-up, which will lead to a greater degree of recombination. Both the  $J_{SC}$  and FF are susceptible to the effects of the presence of traps as well as the electrodes that are used. Because traps reduce the total density of free charge carriers in the device, extra losses result can be observed. This is because trapped charges increase the rate of non-radiative recombination, which is a process that does not involve radiation. Therefore, in order to probe these quantities in order to work towards limiting losses, it is convenient to use a charge transport method that can probe the charge carrier mobility, the trap characteristics,

and the injection properties. This is because such a method can probe the charge carrier mobility, the trap characteristics, and the injection properties.

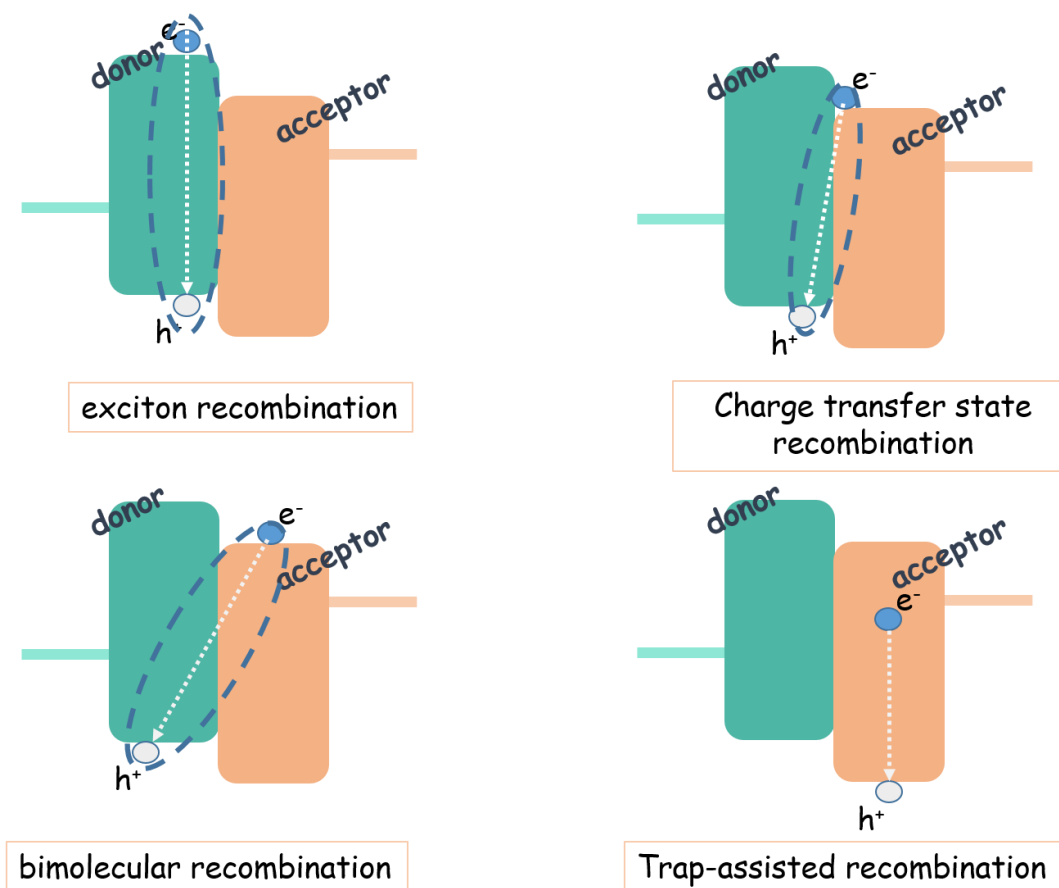


Figure 1.16 Typical recombination pathways in organic solar cells

### 1.5.7 Challenges of Organic Solar Cells

Organic solar cells (OSCs) have been identified as having enormous promise as alternatives to their inorganic counterparts, with devices that are low-cost, lightweight and have a lower environmental impact. Despite the tremendous progress made in OSCs in recent years, there are still several challenges to overcome. There are now several methods for boosting the performance and stability of OSCs. Stability is the capacity of an organic solar cell to sustain its performance over time when subjected to a variety of environmental factors, such



as temperature, humidity, and light. The kind of materials employed, the layout of the device, and the manufacturing method may all influence the stability of organic solar cells. Using more stable materials, such as conjugated polymers or small molecule compounds, can enhance the cell's stability. In addition, correct device design, such as the use of an encapsulating layer to shield the cell from moisture and oxygen, can enhance stability. Maintaining the cells' stability over time also requires proper storage and handling procedures. However, the challenge of controlling the morphology of the active layer in OSCs when scaling to larger areas remains an issue. This makes it difficult to create high-quality active layer thin films, therefore, to fine-tune the efficacy of the device. OSCs in the real world are susceptible to instability due to a number of reasons, as opposed to the laboratory environment. The metastable morphology may restrict the OSCs' stability during their whole lifespan due to diffusion of electrodes and buffer layers, oxygen and water, heating, mechanical strain and irradiation. Encapsulation inhibits the oxygen-induced degradation response by preventing the diffusion of oxygen into the device. However, encapsulation significantly raises manufacturing costs, hence diminishing commercialization possibilities. For this reason, it is essential to comprehend the deterioration processes of the solar cell components. The biggest obstacle for small molecule OSCs is the difficulty in producing spin-coated thin films, despite the batch-to-batch control of their structures.

## **1.6 Organic Light Emitting Diodes (OLEDs)**

OLEDs (Organic Light Emitting Diodes) consist of materials that emit light when an external voltage is applied. When compared to other display technologies, OLED displays provide benefits such as reduced power consumption while retaining a very high contrast ratio and broad viewing angles. In addition, OLED displays are small, lightweight, and may even be manufactured on flexible substrates, allowing for the development of novel and interesting applications. By vacuum thermal evaporation or inkjet printing, OLEDs may be manufactured utilizing small molecules or polymers. The color emitted by organic materials

changes based on their chemical structure. OLEDs are expected to be utilized in the future generation of lighting and displays. Because it comes in a variety of colors, forms, and sizes, it offers more design versatility for a variety of spaces and applications. General considerations must be considered while selecting materials for OLEDs:

- The HOMO-LUMO energy levels of each layer must be ideally aligned according to their unique role in the device.
- Materials must be morphologically stable and produce homogenous vacuum-sublimed films.
- The charge carrier mobility of each layer must be regulated appropriately for optimal performance.
- To avoid exciton quenching, the triplet energy of the layers must be studied, particularly in layers close to the emissive layer; balance by optimizing the thickness of each layer.

### **1.6.1 Emitter Generations**

Some features of the OLED concept should be carefully explained in order to comprehend clearly. Displays and future lighting should benefit greatly from OLEDs; however, until 2012, the only two feasible emission methods for these light-emitting devices were fluorescence and phosphorescence, both of which had drawbacks in terms of efficiency, cost, and instability. This situation changed in 2012 with the development of the efficient Thermally Activated Delayed Fluorescence (TADF) mechanism by Adachi et al. <sup>43</sup>

Excitons generated electrically either at singlets or triplets states, with around 25% being singlets and 75% being triplets. Due to the fact that only excitons in the singlet excited state produce light, the efficiency of the first generation of organic light-emitting diodes (OLEDs) was limited (Figure 1.16).

Emitters that effectively generate light from triplets were developed for the next generation (2nd generation OLED). By incorporating heavy metal into the molecule and converting singlets to triplets, phosphorescence occurs. Phosphorescent materials may generate light from all of their excitons, however the heavy metal, which is often a rare earth element such as iridium or platinum, limits chemical design flexibility and raises costs.

TADF allows for outstanding efficiency without the usage of a heavy metal. In OLEDs of the third generation, 100% internal quantum efficiency (IQE) is also achievable. According to the mechanism, singlet excitons first transfer to the triplet excited state through ISC. Then, with reverse intersystem crossing (RISC), all of the excitons return to the singlet excited state and undergo a radiative decay as they return to the ground state. The primary property of substances that release TADF is a small  $\Delta E_{ST}$ . By absorbing tiny amounts of thermal energy at room temperature, triplets in TADF materials can easily overcome the small  $\Delta E_{ST}$  and convert into singlets. This thermally activated conversion of triplets to singlets results in delayed fluorescence when the up-converted singlets release their energy as light.

$$\lambda = \frac{H_{SO}}{\Delta E_{ST}}$$

- $\lambda$ : is the first-order mixing coefficient
- $\Delta E_{ST}$ : the energy gap between the S and T states under consideration
- $H_{SO}$ : the spin-orbit coupling (SOC) value

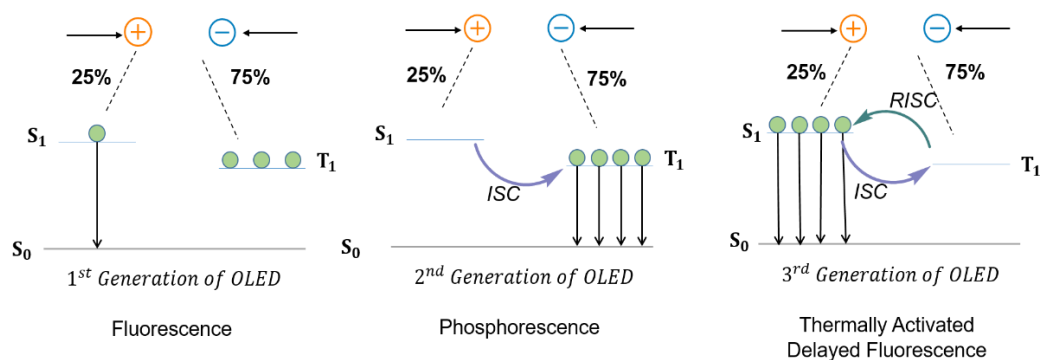


Figure 1.17 Mechanism of 1<sup>st</sup>, 2<sup>nd</sup> and 3<sup>rd</sup> Generation OLEDs, respectively.

### 1.6.1.1 Design of TADF Molecules

It has been observed that aromatic compounds such as nitrogen-containing carbazole, diphenyl amine, and phenoxazine, as well as their derivatives, are often employed as donors in the few number of TADF-type materials that have been published so far. Strong electron repulsion ability and stable, high-energy triplet states are the most significant factors in this selection.

On the other hand, several structures have been used as acceptors, and it has been noted that the variations between these structures impact the emission power, color, and performance of the device. As stated before, cyano (CN)-linked benzene derivatives were utilized as acceptors in the first ground-breaking publication on TADF emission.<sup>44</sup> The reason that these structures function as acceptors is owing to the CN group's great electron attraction. In addition to electron attraction, the presence of the -CN group has significant impact. The CN group inhibits non-radiative relaxations as well as changes in the excited state geometry of the material, resulting in a significant boost in photoluminescence efficiency. As shown in the structures depicted in Scheme 2, it is feasible to alter the color of the irradiation by varying the quantity and location of the donor group. Heterocyclic structures containing nitrogen are electron-poor because of the electronegative nature of nitrogen. Some of these structures have therefore been used as acceptors in TADF-type materials. Triazine<sup>45</sup>, oxadiazole and triazole<sup>46</sup>, heptazine<sup>47</sup>, and 1,4-

diazatriphenylene<sup>48</sup> are significant cases. As acceptor groups, high-efficiency TADF-type materials were designed by incorporating of diphenyl sulfone<sup>49</sup> and diphenyl ketone<sup>50</sup> structures.

### 1.6.2 Working Principle of TADF OLEDs

Anode and cathode are the contacts in OLED devices, and at least one of them must be transparent for light output. ETL is the electron transport layer while HTL is the hole transport layer. The emissive layer is where the emission process happens. For the arrangement of energy barriers, additional layers, such as hole injection layer (HIL), hole blocking layer (HBL), electron injection layer (EIL), and electron blocking layer (EBL), can be added.

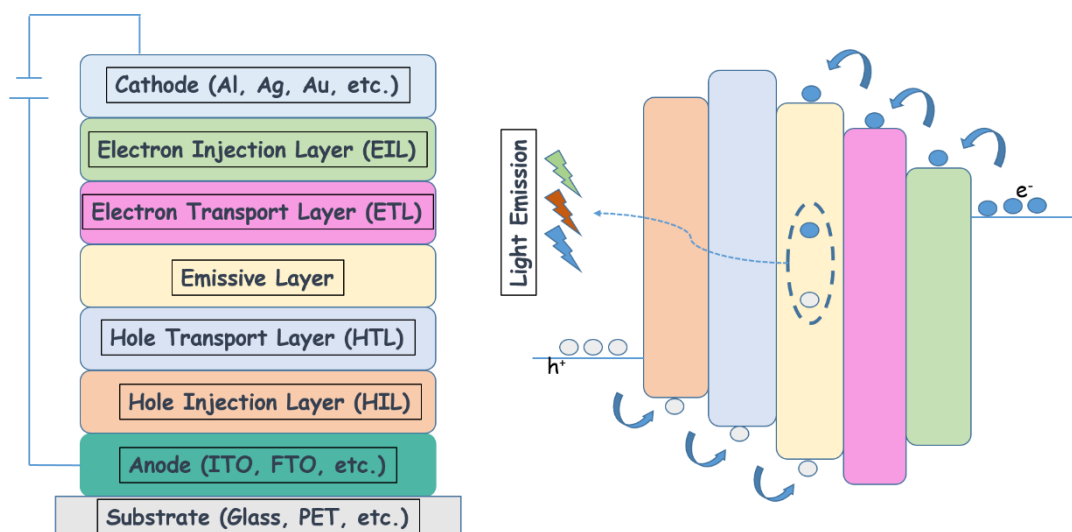


Figure 1.18 Device architecture and working principle of OLEDs

When an external voltage is introduced to an OLED, positive and negative charges are injected into the device, which is followed by charge transfer via the ETL and HTL. Certain energy levels are crucial while designing the architecture of an OLED. Due to a large energy barrier, electrons cannot leap from emissive layer (EL) to HTL, for instance. Finally, before light is released, a positive and negative charge on the same molecule combine to produce an exciton, an energetic state.

To improve the device's efficiency and stability, TADF emitters (guest) are often doped into an appropriate host material to counteract quenching phenomena such as concentration quenching, triplet–triplet annihilation, singlet-triplet annihilation (STA), and triplet-polaron annihilation (TPA).<sup>51–54</sup> The most significant is a theoretical 100% internal quantum efficiency (IQE) that may be obtained for electroluminescence (EL), that is, conversion into light of all excitons created by electron-hole recombination.<sup>55</sup> IQE is calculated using the formula  $\text{IQE} = \beta \times \gamma \times \Phi_{\text{PL}}$ , where  $\beta$  is the exciton production factor resulting in photons,  $\gamma$  is the hole-to-electron carrier balance ratio, and  $\Phi_{\text{PL}}$  is the photoluminescence (PL) quantum yield (PLQY). Electronic stimulation theoretically generates singlet and triplet excitons in a 1:3 ratio.<sup>56</sup> Typically, triplet excitons evaporate as heat as opposed to being transformed into photons. Due to the fact that only singlet excitons create photons, the IQE of fluorescent OLEDs is restricted to 25%. Even PLQY is 100%, the theoretical maximum EQE of the resultant OLED is just 5–7.5%. 25% of singlet excitons are capable of producing prompt fluorescence (PF;  $\tau$ , ns), while 75% of triplet excitons rehouse the singlet energy level by an endothermic RISC before deactivating via delayed fluorescence (DF;  $\tau$ ,  $\mu\text{s}$ ). As the TADF process requires more stages than the PF mechanism, the measured emission decay time ( $\tau$ ) of TADF emitters is greater than that of PF emitters, but shorter than that of phosphorescent molecules.<sup>57</sup>

Several features must be considered when selecting a host molecule for a particular guest emitter, such as a higher energy triplet state for the host than the emitter in order to prevent the quenching of the emitter triplet state, which quenches TADF. When selecting a molecule to operate as a host, the probability of energy transfer from host to guest and the bipolar charge transport capabilities must be taken into consideration.<sup>58,59</sup> Figure 1.19 depicts the working mechanism of TADF OLEDs and the components of the emissive layer.

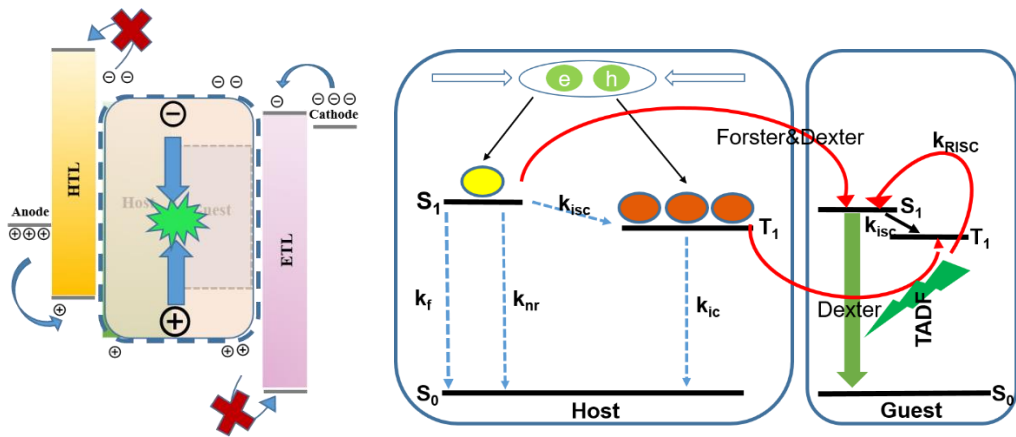


Figure 1.19 Host-Guest mechanism for TADF OLEDs

### 1.6.3 Measuring the efficiency of OLEDs

The external quantum efficiency (EQE) is the ratio of the number of photons produced in the focal plane by the OLED to the number of electrons injected. EQE and IQE have the following relationships.

$$EQE = \text{numbers of output photons} / \text{number of input electron}$$

$$EQE = IQE \cdot \eta_{coupling}$$

where  $\eta_{coupling}$  is the out-coupling efficiency (i.e. the proportion of photons radiated from the device's front surface). Assuming homogeneous emission in the organic layer and a completely reflecting cathode, the following equation describes the proportion of produced light that escapes the substrate.

$$\eta_{coupling} = \frac{1}{\xi \cdot \eta_{org}^2}$$

where  $\eta_{org}$  represents the refractive index of the organic layers and  $\xi$  is a constant that varies depending on the orientation of the radiative exciton dipole and the geometry of the OLED device.

The current efficiency CE, measured in candelas per amp (Cd/A), is the same as EQE, except that CE weighs the photons based on how the eye responds to photopic light.

$$\text{Current efficiency (CE)} = \frac{L \left( \frac{cd}{m^2} \right)}{\text{current density} \left( \frac{A}{m^2} \right)} = cd/A$$

The most often used efficiency unit is the lumens per watt power efficiency (PE). PE is the ratio between the luminous power output in the forward direction, L [lm], and the total electrical power needed to operate the OLEDs at a certain voltage, V.

$$\text{Power efficiency (PE)} = \frac{\left( L \left( \frac{cd}{m^2} \right) \cdot \text{device area} (m^2) \cdot \pi \right)}{i(A) \cdot V} = lm/W$$

Turn on voltage ( $V_{on}$ ) is the operating voltage at a brightness of 1 cd/m<sup>2</sup> and electroluminescence (EL) corresponds the luminescence produced electrically by the application of a voltage.

Two approaches are used in the literature to determine the color of the light emitted by OLED devices. One is the Commission International de l'Eclairage CIELAB (x, y, z) scale, while the other is the Hunter L, a, b (Figure 1.20). The use of these color scales facilitates the comprehension and reporting of color values. According to the CIELAB scale, each color has unique coordinates, which are shown on the diagram as illustrated. L indicates brightness, with values ranging from 0 to 100; a represents greenness to redness with values ranging from -128 to +127; and b represents blueness to yellowness with values similarly ranging from -128 to +127.



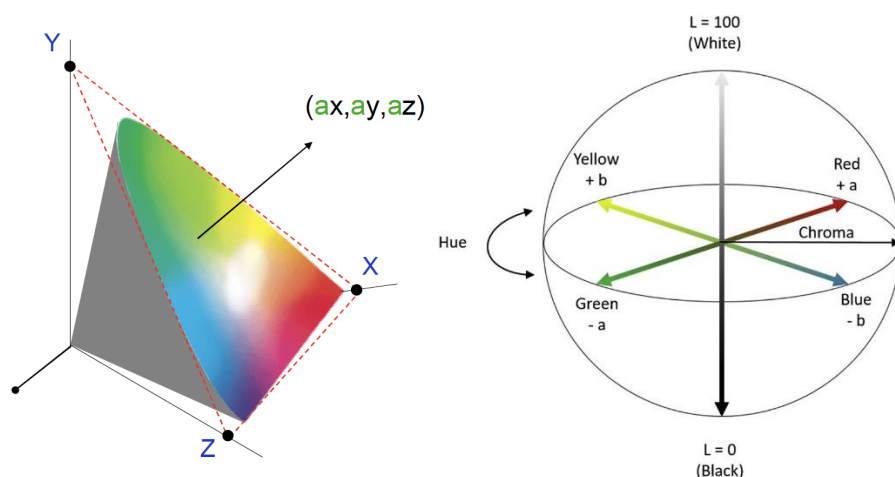


Figure 1.20 CIELAB (x, y, z) and Hunter L, a, b color scales

#### 1.6.4 Challenges of OLEDs

One of the greatest obstacles faced by OLED technology is their relatively high production cost. Commonly utilized thermal vacuum evaporation techniques are inefficient in terms of resource use, scalability, equipment costs, and process complexity.

Large-scale production, as well as the durability and efficacy of materials, provide the industry's greatest obstacles. The utilization of vacuum deposition methods for small-molecule OLEDs in the mass production of larger panels is not practical. The most prevalent panel size is 15 inches; however, industry players are working on screens bigger than 15 inches.

The host material for blue phosphorescent emitters has especially high requirements. Moreover, blue phosphors have issues with color purity and stability, which is why deep blue fluorescent emitters are still used in OLEDs despite their poor maximum IQE.

Using a TADF emitter, which does not include heavy atoms inside the organic material, allows for an IQE of 100%. Nonetheless, the high triplet energy and

extended triplet lifespan continue to be a source of trouble for blue-OLEDs, which limits their useful lifetime. It was suggested that RISC might occur at a more excited state through hybridized local and charge transfer (HLCT) emission, which could lead to both high efficiency and a short exciton lifetime (key for a long operation lifetime).<sup>60</sup> Primary researches are still being conducted.

## CHAPTER 2

### EXPERIMENTAL

#### 2.1 Materials

Indium tin oxide (ITO) was used on the glass substrate as a substrate in the OSC and OLED devices mentioned in this thesis, and it was purchased from Visiontek. The chemicals used in the etching and cleaning stages of ITO coated glass substrates were supplied from Sigma Aldrich. The acceptor PC<sub>71</sub>BM used in the active layer in OSC fabrication was supplied from Ossila. The donor and acceptor materials were blended and anhydrous solvents (1,2-Dichlorobenzene, chlorobenzene, chloroform, etc.) were used in the active layer solutions.

For OLED fabrication; TPBi is used as ETL, NPB is used as HTL and mCBP is acted as host in emissive layer were taken from Lumtec. These materials are deposited by using the thermal evaporator. Boron nitride (BN) crucible was used in the evaporation of organic materials and was purchased from Nanovak.

LiF and Al were used as a top contact in three chapters and they were coated on the devices with deposition controller in metal evaporator. The purchase of high-purity metals from Kurt J. Lesker. R.D. Mathis Company provided the tungsten boats used for evaporation. Using QCM sensors, the thicknesses of the coated metals were controlled.

Delta Technologies supplied coated glass slides (8 ohm/square) for electrochemical characterizations. Sigma Aldrich supplied the supporting electrolytes and solvents (acetonitrile, nitromethane, dichloromethane). Sigma Aldrich glass slides were utilized for UV-Vis and photoluminescence analyses.

## 2.2 Solar Cell Fabrication

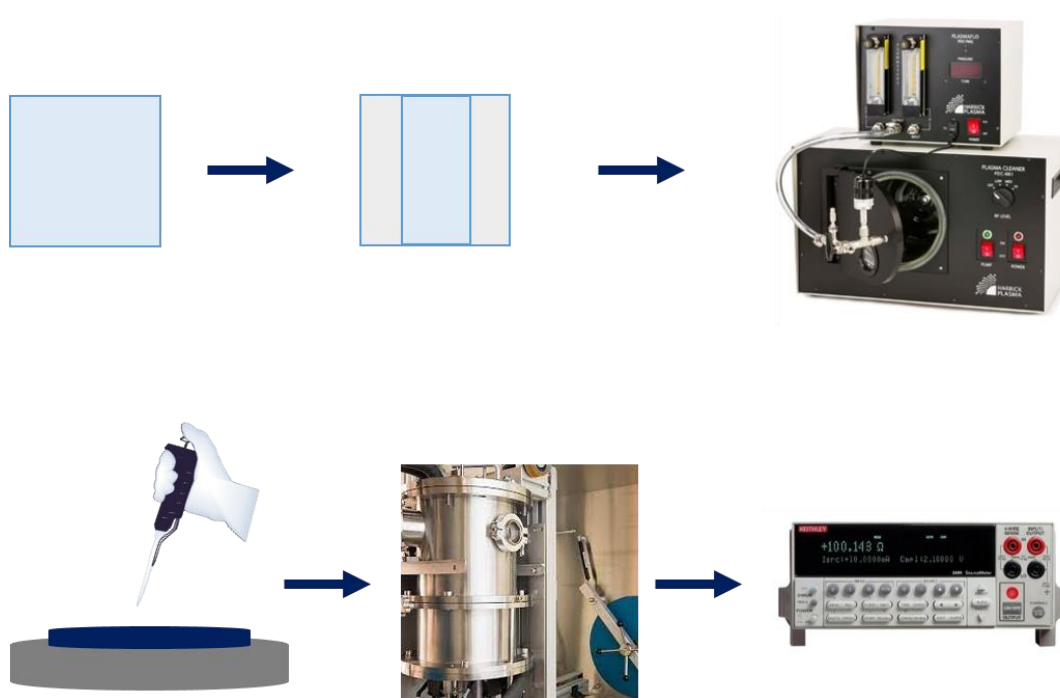


Figure 2.1 Schematic representation of the experimental sequence of solar cell fabrication

Solar cell fabrication involves multiple steps from beginning to end. Among these are the selection of layers discussed in the chapter of the working principle, the optimization of the active layer, and the selection of the proper top electrode. Since conjugated polymers are adversely impacted by oxygen and moisture in the air, numerous stages are carried out in gloveboxes filled with nitrogen. The selection and cleaning of the substrate is crucial following the selection of the proper substrate. Glass was used as the substrate and ITO as the anode in this thesis. First of all, ITO coated glasses are etched with Zn powder and dilute HCl. The purpose of the etch is to have the desired device area. After this process, 15 minutes of ultrasonication is performed with Hellmanex, distilled water, acetone and IPA, respectively. Oxygen plasma is applied to remove residual organic impurities, to reduce the surface tension of ITO and to increase the work function of ITO. Then the required layers are coated using a spin coater. For organic solar cells, PEDOT:

PSS is used for the hole-transport layer. As a cathode, the metal is evaporated at low pressure in the metal evaporator (Figure 2.1). All photovoltaic measurements are made with a device that simulates sunlight and a Keithley. The main distinction between binary and ternary devices' preparation is the active layer composition. In Binary BHJ solar cells, the active layer consists of a donor and an acceptor, however in this work, two polymer donors and an acceptor were employed to construct the ternary solar cell.

The sequence described above applies to both binary and ternary solar cells. There is only one difference in the preparation stage, and that is the preparation of the blend to be used in the active layer. In binary solar cells, a blend which contains the donor and acceptor material is dissolved in the appropriate solvent and coated in the desired thickness using a spin coater. In ternary solar cell fabrication, the active layer contains two donors and an acceptor, and the preparation stage of this blend is quite challenging. These three materials must be dissolved and matched in the same solvent. Organic solar cell fabrication has many active layer optimizations; these are;

- solvent optimization
- donor: acceptor ratio optimization
- concentration optimization
- thickness optimization
- adding solvent additives and optimizing their effects
- thermal annealing effects and optimization

### 2.3 TADF OLED Fabrication

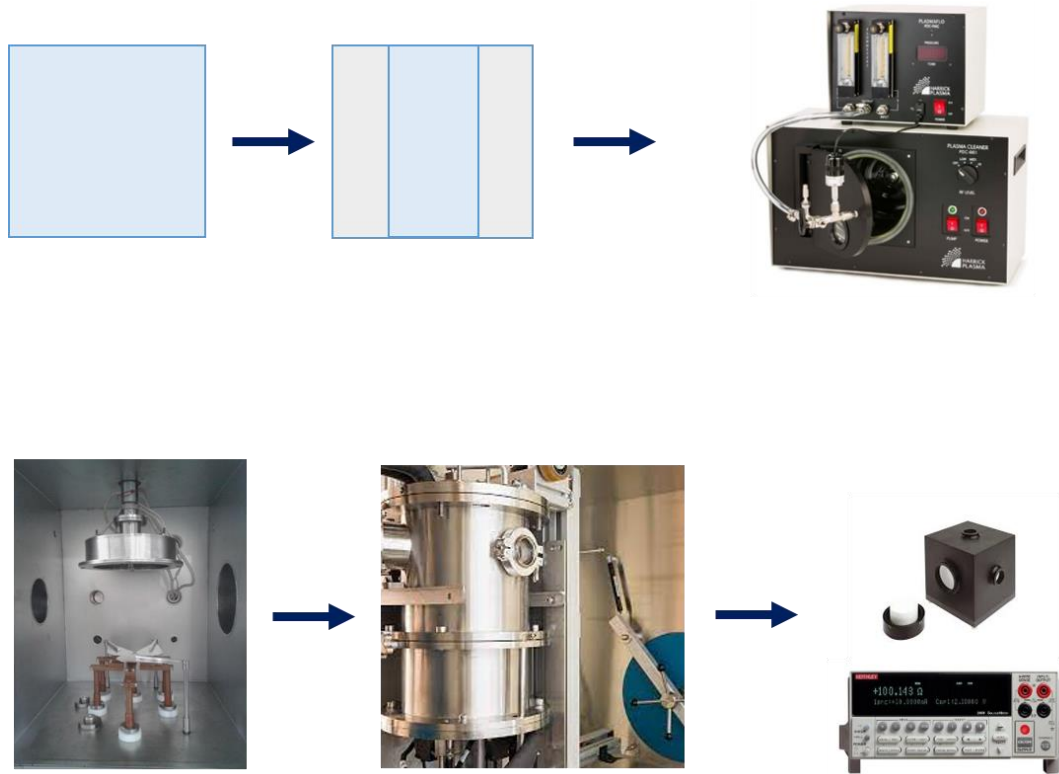


Figure 2.2 Schematic representation of the experimental sequence of solar cell fabrication

ITO coated glasses are firstly etched by using Zn powder and dilute HCl. Then, etched substrates are washed with Hellmanex detergent, distilled water, acetone and IPA, respectively, for 15 minutes in ultrasonic bath. In the manufacturing of OLED, unlike the production of solar cells, oxygen plasma is applied for a longer duration. This is because ITO and LUMO of alpha-NPD have a large energy barrier between them. As the duration of the oxygen plasma extended, the work function value of ITO increased and the energy barrier lowered.

Because of small molecules can be evaporated easily under the low pressure, organic evaporator was preferred as it does not require any solvent, provides a more homogeneous coating and consumes much less material than solution processing.

LiF and Al is deposited under the low pressure, approx.  $10^{-7}$  torr. Measurements and depositions are made in the  $N_2$  filled glovebox system. Then, OLED measurements are taken by using Keithley source meter and integrating sphere. There are some common optimizations during TADF-OLED fabrication, which are;

- Thickness optimizations: As it was mentioned previously, OLEDs have some layers to complete the electron and hole transportation to the emissive layer. These layers are ETL, HTL, EIL, HIL, EBL and HBL. The number of layers can be optimized in order to align energy levels. Because of the mobility of electrons and holes are different, the thickness of layers is so critical to achieve the best efficient OLED. During the fabrication, the thicknesses of layers should be optimized.
- Host-Guest ratio optimizations: The emissive layer contains two components in emissive layer: host and guest. The host must have a higher triplet energy than the TADF emitter (guest) to prohibit a reverse energy transfer. By contrast, when a low-triplet energy host is used, the triplet excitons are quenched, resulting in low EQE in the TADF-OLEDs. Then a high triplet energy host is employed, all singlet and triplet excitons are harvested, leading to a high EQE in the TADF-OLEDs. However, the large contribution of triplet excitons generally shortens the device lifetime of the devices, as does the poor device stability of the high triplet energy host. In order to solve the problems with conventional TADF devices,
- The choice of host material: The EML usually consists of a wide-energy-gap host material doped with a TADF guest. This enables the effective transfer of Forster and Dexter energy from the host to the guest, as well as the confinement of both singlet and triplet excitons to the guest.<sup>61,62</sup> Hole-transporting (p-type), electron-transporting (n-type), and ambipolar host materials are the three basic kinds of materials based on their charge transport capabilities.<sup>63</sup>
- Host-guest ratio in the emissive layer
- Proper top contact optimization

## **2.4 Characterizations**

Numerous characterizations are performed from beginning to end throughout the fabrication of optoelectronic devices, providing crucial information regarding device performance. Optoelectronic devices were characterized using the following instruments.

### **2.4.1 UV-VIS Spectroscopy**

Absorption of thin films and polymer and/or small molecule solutions was investigated using Perkin Elmer Lambda 25 UV-Vis spectrophotometer in all three chapters studied in this thesis. UV-VIS spectroscopy is a form of absorption spectroscopy in which the molecule absorbs light in the ultraviolet and visible areas (200-400 nm and 400-700 nm, respectively).

UV-VIS spectroscopy may be used to determine the degree of conjugation, functional groups, the arrangement of geometric isomers, and the substance's purity. This method, which is used in many fields, is in both the OLED and OSC sections of this thesis.

### **2.4.2 Photoluminescence Spectroscopy**

Solution (in chloroform) and thin film PL spectra of synthesized small molecules in the OLED part of this thesis were taken from Perkin Elmer spectrophotometer. Photoluminescence spectroscopy, often known as PL, occurs when photons or light energy trigger the emission of a photon from any substance. It is a non-contact and non-destructive technique for material inspection. Light is essentially focused onto a sample, where it is absorbed and where photo-excitation might occur. The photo-excitation causes the material to jump to a higher electronic state, and when it relaxes and returns to a lower energy level, it releases energy (photons). PL is the emission of light or luminescence that results from this process.



### 2.4.3 Time-Resolved Photoluminescence

As previously indicated, TADF molecules exhibit delayed fluorescence because the energy gap between their singlet and triplet excited states is small. Time-resolved photoluminescence is a crucial tool for characterizing TADF molecules (TRPL). Many different TADF molecules have been published in the literature with the goal of increasing the efficiency of OLEDs by converting non-emissive triplet states into emissive singlet states. Due to the reverse intersystem crossing process that is thermally engaged to enable up-conversion of low energy triplet states to the emissive singlet level, TADF emitters may collect both singlets and triplets by fluorescence (prompt and delayed).

The fluorescence (or, more commonly, photoluminescence) lifespan is an inherent property of a luminous species that may shed light on the excited state dynamics of the species. TRPL is the technique of choice for investigating fluorescence, the emission of photons caused by the rapid deactivation of electrons. Typically, the lifetime of a molecule in its lowest excited singlet state spans between a few picoseconds and a few nanoseconds. This fluorescence lifetime is affected by the molecular environment (e.g., solvent, presence of quenchers ( $O_2$ ), or temperature) and interactions with other molecules. The decay kinetics are additionally affected by processes such as Forster Resonance Energy Transfer (FRET), quenching, solvation dynamics, and molecule rotation. Consequently, variations during a lifetime may reveal information about the local chemical environment or insights into reaction processes.

### 2.4.4 Cyclic Voltammetry

CV, or cyclic voltammetry, is a method of electrochemistry that measures the current that flows in an electrochemical cell when the voltage in the cell is greater than what would be expected according to the Nernst equation. CV is accomplished by repeatedly cycling the voltage of a working electrode and then measuring the resultant current.

Cyclic voltammetry investigations were also performed for the purpose of electrochemical characterization of chemically produced polymers. The polymers were filtered through a 0.45m PTFE filter after being dissolved in  $\text{CHCl}_3$  at a weight concentration of 1mg/ml. The ITO glass electrodes were then coated with a polymer solution using a spray gun. The voltage was applied between the working and reference electrodes with the use of a Gamry potentiostat (Reference 600), which also has counter and reference electrodes attached. For its neutrality throughout a broad potential range, acetonitrile was chosen as the solvent.

#### **2.4.5 Atomic Force Microscopy**

Atomic Force Microscopy (AFM) was used to obtain topographic properties, surface smoothness and thickness information of fabricated OSCs. The device used is Veeco MultiMode V and this information was accessed by tapping mode. With the Tapping mode, it is possible to obtain the results with high resolution while observing the minimum damage to the sample.

#### **2.4.6 Transmission Electron Microscopy**

Transmission Electron Microscopy (TEM) was used to observe the morphological properties of the active layers of fabricated OSCs. The device used is the FEI Tecnai G2 Spirit BioTwin CTEM, and it is possible to conduct examinations at the nano-scale with this instrument.

#### **2.4.7 OSC Characterization**

Using a Keithley 2400 source measurement unit and an AM 1.5 solar simulator, the current density-voltage (J-V) characteristics were determined. Current measurements were taken from 8 cells in each device produced, in the voltage range from -0.2 V to 1.0 V. The calculated  $J_{SC}$  values were then verified with the incident photon to current / charge carrier efficiency (IPCE). IPCE is a measure of

how absorbed photons are efficiently converted to charge carriers and collected at electrodes. Under illumination, the photocurrent response of the cell was measured using a calibrated Si photodiode (Newport) as the standard. The IPCE curve resembles the polymer PCBM absorption spectrum. It is possible to estimate the  $J_{sc}$  values of the solar cells based on the curve.

#### **2.4.8 OLED Characterization**

As with OSC characterization, voltage vs current values are measured for OLED characterization, together with voltage versus luminescence measurements. The Maya spectrophotometer combined with a 100  $\mu$ m diameter fiber optic detects luminance. The software SpectraSuite processes data and using an integrating sphere, the EQE data of OLEDs was collected, simultaneously.



## **CHAPTER 3**

### **AIM OF THE THESIS**

The aim of this thesis is to improve the performance of optoelectronic devices, specifically organic solar cells (OSCs) and organic light-emitting diodes (OLEDs). The efficiency of these devices refers to their ability to convert absorbed light or electrical energy into useful output.

For OSCs, increasing efficiency means increasing the ability of the device to convert light energy into electrical energy. This can be achieved by using more efficient materials, improving the device architecture, and optimizing the manufacturing process.

For OLEDs, increasing efficiency means increasing the ability of the device to convert electrical energy into light. This can be achieved by using more efficient light-emitting materials, improving the device architecture, and optimizing the manufacturing process.

In summary, the main objective of the thesis is to increase the efficiency of both OSCs and OLEDs by exploring new materials, device architectures, and manufacturing techniques to make them more efficient in converting energy into useful output.



## CHAPTER 4

### EFFECT OF FLUORINATION STRATEGY AND SIDE CHAIN ENGINEERING

*This study has been patented by the Turkish Patent and Trademark Office (Turkish Patent Institute Application Number: PCT/TR2022/050835)*

#### 4.1 Introduction

Due to its low cost, ease of fabrication, applicability on flexible substrates, good film-forming properties, high morphological stability, and light weight, many scientists have been studying organic thin-film photovoltaics (PV) over the past two decades. Organic polymer one of the most popular third-generation PV cells, provide lower energy requirements, and the most efficient bulk heterojunction (BHJ) polymer solar cell has recently achieved 18% power conversion efficiency (PCE).<sup>64</sup> Nowadays, considerable efforts in materials engineering<sup>65-68</sup>, morphology control<sup>69-71</sup> and optimize the structure of the devices<sup>72-74</sup> have been expended to achieve the abovementioned record.

All BHJ OSCs contain n-type acceptor and p-type conjugated polymer donor. In this study, the acceptor was the PC<sub>71</sub>BM, and the donors were the P-HTBDT, P-FTBDT, and P-FBDT, random polymers. The PCE value depends on basically three parameters, which are open-circuit voltage ( $V_{OC}$ ), short circuit current density ( $J_{SC}$ ), and the fill factor (FF). The lower the HOMO level of the conjugated polymer, the higher the  $V_{OC}$  value, and thus the PCE value.<sup>75,76</sup> To obtain a high  $J_{SC}$  value, the absorption region of the conjugated polymer should be as broad as possible, and/or its bandgap should be close to the optimum level. Due to the "internal" nature of BHJ, it is challenging to improve FF in BHJ devices continuously. Some intrinsic variables in BHJ, including randomly mixed

morphology, imbalanced donor and acceptor mobility, and bimolecular recombination, are well recognized to influence FF.<sup>77</sup>

The D-A copolymers are characterized by their narrow bandgap, a wide range of light absorption wavelengths, controllable energy level, and photon absorption characteristics. They have an alternating electron-rich unit (D) and an electron-deficient unit (A).<sup>78</sup> In 2010, after the promising PCE (5.5%) obtained from the use of PBDTTPD polymer in solar cells, the interest in polymers containing TPD and BDT had increased considerably.<sup>79</sup> The random D-A copolymers containing TPD and benzothiadiazole as acceptors and BDT as donors in the backbone of the polymers discussed in this article. Because of its planar structure, which is beneficial for the electron delocalization, TPD can stabilize excited state energy; hence TPD-bearing conjugated polymers are expected to have high  $V_{OC}$  values. Moreover, TPD has a strong electron-withdrawing characteristic, significantly lowering the lowest unoccupied molecular orbital (LUMO).<sup>68,80</sup>

In this chapter of the dissertation, the impact of mono-fluorine substitution of benzothiadiazole will be investigated, and a comparison will be conducted between mono-fluorination and di-fluorination substitution of benzothiadiazole. According to Cevher et al., the addition of fluorine reduces the HOMO level and raises the  $V_{OC}$  value. In addition to deepening the HOMO level, the F substitution modifies interactions with neighboring rings, boosting planarity and inducing strong intermolecular interactions between chains, which can influence nanoscale morphology. Increased planarity of the polymer backbones facilitates the charge transfer mechanism, allowing for larger PCE values.<sup>81</sup> The fluorine substitution is a very effective way to lower the HOMO and LUMO energy levels of the polymer, resulting in higher  $V_{OC}$ .<sup>82</sup> Second, the effect of replacing the alkoxy group with alkylthienyl on the performance of BHJ OSCs is discussed. Since the introduction of 2-alkylthienyl as the conjugated side group in benzo[1,2-b:4,5-b']dithiophene (BDT) units,<sup>83</sup> alkylthienyl substituted BDT (BDT-T) units have been widely employed to design innovative photovoltaic polymers, enhancing power conversion efficiencies (PCEs) to new levels in the field of OSCs.<sup>84,85</sup> In 2013, Chen et al.



introduced a photovoltaic polymer (PTB7-Th) with improved photovoltaic characteristics by inserting a 2-(2-ethylhexyl)-thienyl group into the BDT unit of the well-known photovoltaic polymer, PTB7.<sup>86</sup> Because of the extended conjugation of the polymer, the resultant polymers exhibited narrower bandgaps and enhanced charge transport characteristics when the typically utilized alkyl- or alkoxy-based side chain on the benzodithiophene unit was replaced with an alkylthiophene unit. It's worth noting that this modification also leads to increased  $V_{oc}$  value by deepening the polymer's HOMO level.<sup>87</sup> To sum up, although the effects of different units are explored one by one, finding high  $V_{oc}$ , increased  $J_{sc}$ , and superior morphology all at the same time remains a significant issue in the literature.

## **4.2 Experimental**

### **4.2.1 Synthesis**

Chemicals used synthesis of polymers are purchased from Sigma-Aldrich and used without further purification unless otherwise noted. Toluene and tetrahydrofuran (THF) freshly distilled over sodium/benzophenone. BDTT was purchased from Solarmer (recently closed firm) and used as it is. BT-H, BT-F was synthesized according to the previously published methodologies<sup>88,89</sup>. Synthetic pathway of polymer synthesis was illustrated in Figure 4.1. Nuclear magnetic resonance spectra were recorded by Bruker Spectrospin Avance DPX-400 Spectrometer, Uv-Vis spectra were taken by Jasco V-770 spectrophotometer, gel permeation chromatography studies were performed by Shimadzu RID-20A electrochemical studies were investigated by Gamry 600 potentiostat.

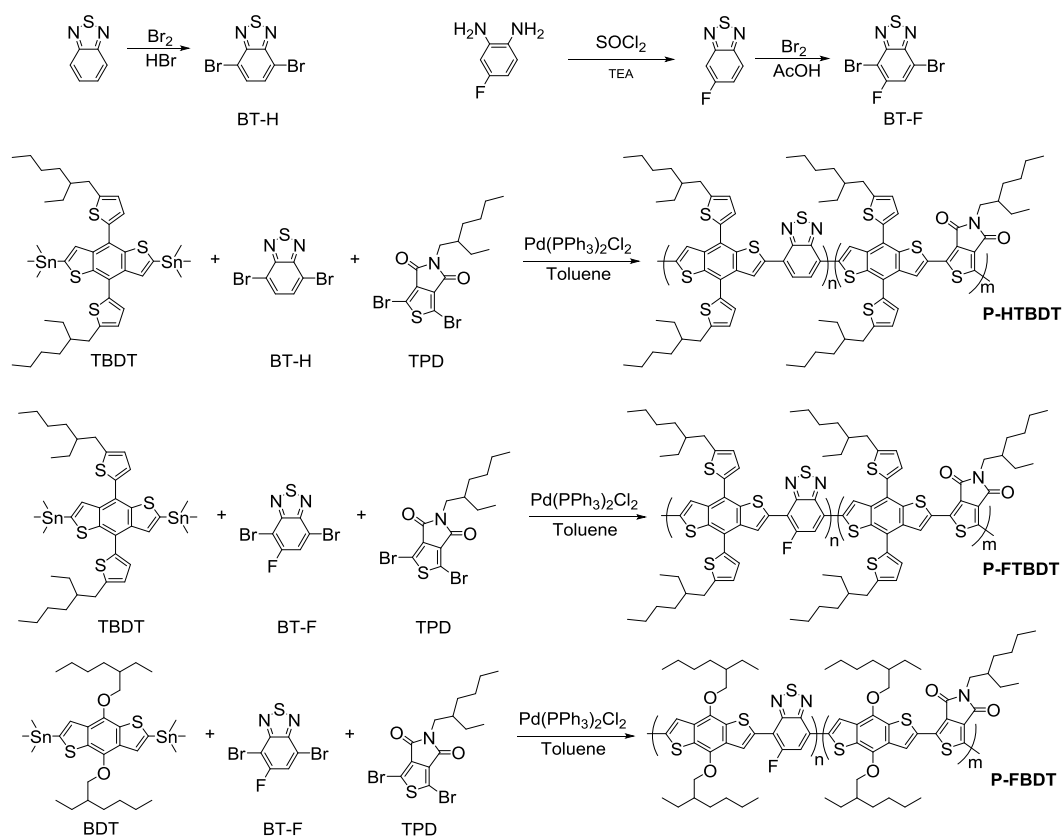


Figure 4.1 Synthetic pathway of polymers.

The polymer syntheses in this chapter were conducted by Şevki Can Cevher. Synthesis of BT-H with minor changes as follows; benzothiadiazole was brominated in hydrobromic acid (37%) with bromine under reflux overnight. After cooling the reaction mixture to the room temperature excess bromine was treated with saturated sodium bisulfide solution. Clear/almost transparent mixture was filtered and washed with excessive amount of water then with diethyl ether and the final product was recrystallized in ethanol.

Synthesis of BT-F with minor changes as follows; 4-fluorobenzene-1,2-diamine was reacted with thionyl chloride in triethylamine to obtain the 5-fluorobenzothiadiazole core. 5-fluorobenzothiadiazole was brominated with molecular bromine in  $\text{HBr}$  solution at reflux temperature. After workup, obtained solid was recrystallized from ethanol to give the desired product 4,7-dibromo-5-fluorobenzothiadiazole.

Synthesis of PH-TBDT: 337 mg (0.378 mmol) TBDT, 56 mg (0.189 mmol) BT-H, 80 mg (0.189 mmol) TPD were added in two ways round bottom flask and toluene was added via syringe needle under inert atmosphere ( $N_2$ ) and the solution was bubbled for 20 minutes. After that, palladium catalyst was added and temperature was set to reflux for two days. Next, 5 mol % palladium catalyst added with end gapper stannylated thiophene (0.756 mmol) and refluxed for 5 hours and then 1.512 mmol bromothiophene was added and refluxed overnight. Next day, the polymerization reaction mixture was cooled down and the solvent was evaporated to obtain dense liquid. This liquid was added into methanol drop wise to obtain solid polymer. Solid polymer was filtered and dried. Further purification was performed with Soxhlet extraction with methanol, acetone, hexane and the polymer solution was obtained from chloroform portion. To this chloroform portion 35 mg Quadrasil was added and stirred at room temperature for 1 hour. After filtering the chloroform portion, evaporation of chloroform solvent was performed to obtain dense liquid which was later dropped wise added into a methanol gave the desired polymer PH-TBDT was obtained as dark blue/black solid (257 mg 89% yield).  $^1H$  NMR of the polymer did not give an informative spectrum yet intense and broad aliphatic hydrogens were observed. GPC results gave Mw: 76kDa, Mn: 44 kDa and PDI: 1.73.

Synthesis of PF-TBDT: Similar methodology was followed with 337 mg (0.378 mmol) TBDT, 59 mg (0.189 mmol) BT-F, 80 mg (0.189 mmol) TPD. Desired polymer was obtained as dark blue/black solid (245 mg, 84% yield).  $^1H$  NMR of the polymer did not give an informative spectrum yet intense and broad aliphatic hydrogens were observed. GPC results gave Mw: 120 kDa, Mn: 46 kDa and PDI: 2.5.

Synthesis of PF-BDT: Similar methodology was followed with 286 mg (0.378 mmol) BDT, 59 mg (0.189 mmol) BT-F, 80 mg (0.189 mmol) TPD. Desired polymer was obtained as dark blue/black solid (213mg, 88 % yield).  $^1H$  NMR of the polymer did not give an informative spectrum yet intense and broad aliphatic

hydrogens were observed. GPC results gave Mw: 220 kDa, Mn: 59 kDa and PDI: 3.7.

Cyclic voltammetry technique was employed via three electrode systems to observe redox characteristics of conjugated polymers. Platinum wire, silver wire and polymer coated indium tin oxide (ITO) coated glass were chosen as CE, RE and working electrode, respectively. For preparation of working electrode, polymers were dissolved in chloroform (1 mg/ml) and coated on ITO surface via spray gun. The electrodes were immersed in 0.1 M TBAPF<sub>6</sub>/ACN electrolyte solution and their cyclic voltammograms were recorded at 100 mV s<sup>-1</sup> scan rate by using Gamry 600 potentiostat. Polymer coated indium tin oxide (ITO) coated glass was also used as a thin film in optical characterization which was carried by Varian Cary 5,000 UV-Vis spectrophotometer.

#### 4.2.2 Device Fabrication

In this study, OSCs were fabricated with the device architecture of ITO/PEDOT: PSS/Donor: PC<sub>71</sub>BM/LiF/Al. The thickness of photoactive layer was determined with AFM. Etched ITO-coated glasses were ultrasonicated with Hellmanex, distilled water, acetone, and water, respectively, for 15 mins. Then oxygen plasma was applied to regulate the work function and clean from the organic impurities. After cleaning processes, PEDOT: PSS was coated and annealed at 135 °C for 15 mins. The optimized weight concentration was 24 mg/ml for polymer P-FBDT, P-FTBDT, and P-HTBDT, and 1,2-dichlorobenzene (*o*-dcb) was chosen as a solvent. LiF and Al were deposited under low pressure at the top of the device. The IV characterizations of generated OSCs were performed with Keithley 2400 under simulated AM 1.5 G solar irradiation (100 mW/cm<sup>2</sup>) between -0.2 V and 1.0 V. The external quantum efficiency (EQE) is measured using a grating monochromator setup. The energy level diagram was given in Figure 4.2.

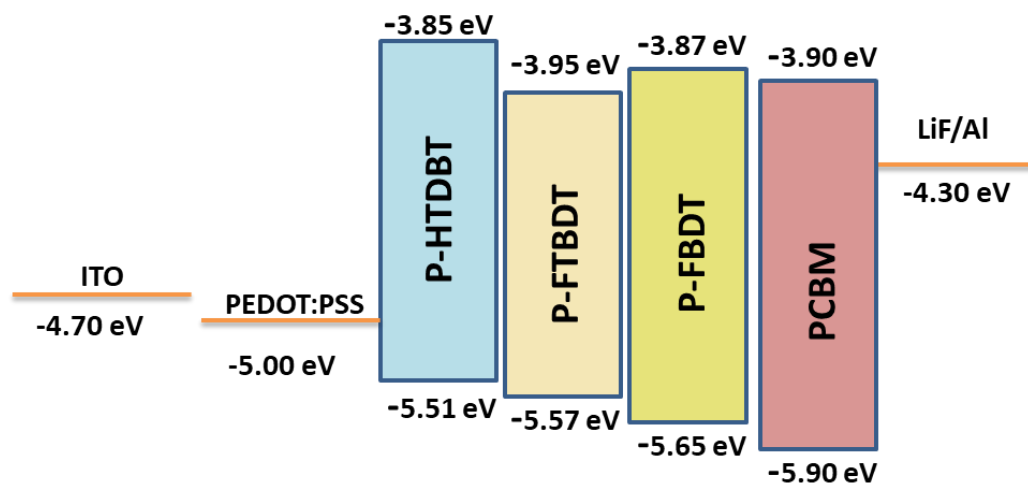


Figure 4.2 The energy level diagram of the fabricated P-HTDBT, P-FTBBDT and P-FBBDT based OSCs.

### 4.3 Results and Discussion

#### 4.3.1 Characterization of Optical and Electronic Properties

Some critical parameters such as band gap, HOMO and LUMO energy levels for organic solar cell applications were calculated by using cyclic voltammogram and following equations:  $E_g^{el} = -(\text{HOMO-LUMO})$ ,  $\text{HOMO} = -(4.75 + E_{\text{onset}}^{\text{ox}})$  and  $\text{LUMO} = -(4.75 + E_{\text{onset}}^{\text{red}})$ . As shown in Figure 4.3, all polymers exhibited p-type and n-type doping behavior (ambipolar character). When electrochemical properties of polymers were compared as shown in Table 4.1, P-FTBBDT has higher oxidation potential with respect to P-HTBBDT. Same behavior was valid for mono fluorinated P-FBBDT which has lower oxidation potential from two fluorinated PF given in our previous study.<sup>81</sup> These observations were resulted from different electron densities because electron withdrawing nature of fluorine atom causes to lower electron densities and lowering oxidation potential. HOMO levels of P-FTBBDT and P-HTBBDT were -5.65 and -5.57 eV, respectively. On the other hand, HOMO levels of mono fluorinated P-FBBDT and two fluorinated PF were -5.51 and

-5.78 eV, respectively. Deeper HOMO level caused by fluorine addition to backbone was also observed in literature.<sup>88,90,91</sup>

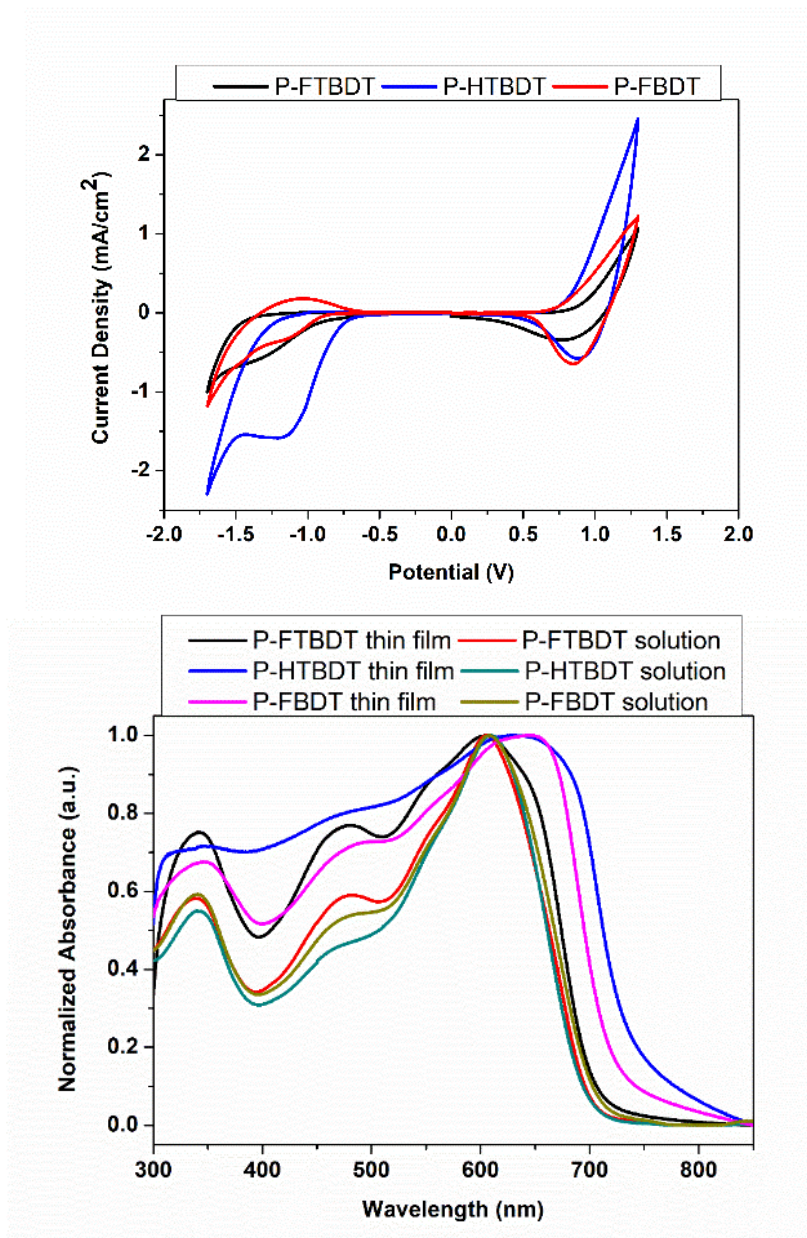


Figure 4.3 a) Cyclic voltammetry curves of polymers P-HTBDT, P-FTBDT and P-FBDT and b) absorption spectra of corresponding polymers (solid and thin film state) in UV-VIS region

Besides HOMO and LUMO energy levels, the absorption behavior of polymers in the UV-Vis region is also critical information for organic solar cell applications.

From UV-Vis absorption spectrum (Figure 4.3b), maximum absorption wavelengths ( $\lambda_{\max}$ ), onset of maximum absorption wavelengths ( $\lambda_{\max}^{\text{onset}}$ ), and optical band gaps ( $E_g^{\text{op}}$ ) the polymers were given in Table 4.1. The  $\lambda_{\max}$  values were determined as 635 nm, 640 nm and 605 nm for P-HTBDT, P-FBDT and P-FTBDT, respectively. This value was 703 nm for PF. Moreover, optical band gaps were 1.67, 1.71, 1.77, 1.79 eV for P-HTBDT, P-FBDT and P-FTBDT and PF, respectively. Increasing band gap with fluorine substituent was compatible with literature studies.<sup>92,93</sup> When compared to solution spectrum, thin film spectrum showed red-shift which was resulted from aggregation in thin film; because of the intermolecular  $\pi$ - $\pi$  interactions, its absorption peaks were widened and red-shifted.

Table 4.1 Summary of electrochemical and optical studies of P-HTBDT, P-FBDT and P-FTBDT.

	$E_{ox}$ (V)	$E_{red}$ (V)	$E_{ox}^{onset}$ (V)	$E_{red}^{onset}$ (V)	HOMO (eV)	LUMO (eV)	$E_g^{el}$ (eV)
<b>P-HTBDT</b>	1.15	-1.20	0.82	-0.80	-5.57	-3.95	1.62
<b>P-FTBDT</b>	1.25	-1.13	0.76	-0.90	-5.51	-3.85	1.66
<b>P-FBDT</b>	1.20	-1.30	0.90	-0.88	-5.65	-3.87	1.78
PF*	1.29	-1.52	1.03	-1.15	-5.78	-3.60	2.18

	$\lambda_{max}$ (nm)	$\lambda_{max}^{onset}$ (nm)	$E_g^{op}$ (eV)
<b>P-HTBDT</b>	635	745	1.67
<b>P-FTBDT</b>	640	725	1.71
<b>P-FBDT</b>	605	700	1.77

### 4.3.2 Photovoltaic Properties

BHJ OSCs were fabricated with a conventional device architecture based on ITO/PEDOT: PSS/Active Layer/LiF/Al. Details of device fabrication are emphasized in the experimental part. Donor-acceptor ratio, active layer thickness, solvent additives (CN, DIO, and DPE), and thermal annealing were performed during the device fabrication process to obtain the optimum morphology. The best working solvent was 1,2-dichlorobenzene (*o*-dcb) for all devices. Photovoltaic performances of the devices completed by using three polymers as donors were given in Table 4.2.



$$V_{OC} = (1/e)(|E_{Donor}^{HOMO} - E_{Acceptor}^{LUMO}|) - 0.3 \text{ V}$$

Before beginning the optimization studies, the given equation was used to calculate the theoretical  $V_{OC}$  from the HOMO values of the donor materials (P-HTBDT, P-FTBDT, and P-FBDT) and the LUMO value of the acceptor PCBM. The 0.3 V value in the formula, which is described by the Shockley-Queisser (SQ) theory for an idealized solar cell, represents the energy losses within the material or at the organic-electrode contacts.<sup>94,95</sup> Theoretical  $V_{OC}$ s are determined as follows: 0.91 V, 0.89 V, and 0.94 V. Theoretical  $V_{OC}$  values are nearly identical to experimental  $V_{OC}$  values, elucidating that the optimizations were completed successfully and that there were no other losses beyond theoretical losses. Theoretical  $V_{OC}$  of P-FBDT is higher than the experimental  $V_{OC}$  which is the evidence of emergence of a charge transfer state forming at the donor: acceptor interface.<sup>96</sup> A high  $V_{OC}$  observed in P-FBDT based OSC can be expected from the low-lying HOMO energy level of P-FBDT (-5.65 eV).

Table 4.2 Photovoltaic properties of fabricated solar cells.

Polymers	Polymer: PCBM ratio	PCE	FF	V <sub>oc</sub> (V)	J <sub>sc</sub> (mA/cm <sup>2</sup> )	Treatment
P-HTBDT	1:2	5.51	58.17	0.91	10.2	-
<b>P-HTBDT</b>	<b>1:2</b>	<b>7.35</b>	<b>63.11</b>	<b>0.90</b>	<b>12.8 (12.7)</b>	<b>2%DIO</b>
P-FTDBT	1:2	6.72	60.14	0.89	12.3	-
<b>P-FTDBT</b>	<b>1:2</b>	<b>7.76</b>	<b>59.46</b>	<b>0.92</b>	<b>13.9 (13.6)</b>	<b>2%DIO</b>
P-FBDT	1:2	7.17	57.83	0.95	12.3	-
<b>P-FBDT</b>	<b>1:2</b>	<b>9.21</b>	<b>60.33</b>	<b>0.95</b>	<b>15.4 (15.3)</b>	<b>6% DPE</b>
PF*	1:2	<b>7.32</b>	<b>57.76</b>	<b>0.88</b>	<b>14.40</b>	-

Among all polymers, P-FBDT based OSCs with the 6% DPE solvent addition has delivered PCE of 9.21% together with 60% FF and 15.4 mA/cm<sup>2</sup> J<sub>sc</sub>. The increased PCE can be attributed from the improved polymer morphology, probably because of the high solubility and high molecular weight of P-FBDT. The crystalline link tends to be excellent as the M<sub>w</sub> increases, which is advantageous for carrier transport.<sup>97</sup>

Although DPE was tested for P-HTBDT and P-FTDBT based OSCs, the addition of 2% DIO improved the morphology of these devices more effectively. While the highest PCE achieved without using any solvent additives for P-HTBDT was 5.51%, the PCE value has reached 7.35% at the use of 2% DIO. On the other hand, while the highest efficiency obtained without using DIO for P-FTDBT was 6.72%, this value increased to 7.76% at the use of DIO. Treatment with the addition of DPE and DIO enhanced the device performance up to 25% due to a simultaneous increase in all the photovoltaic parameters. As it is well known, DIO dissolves PCBM aggregates selectively in the BHJ film, allowing PCBM molecules to be intercalated into the polymer domains.<sup>98</sup> Moreover, DIO as an additive allows for a

slower crystallization process during spin-coating, resulting in improved morphology due to improved intermolecular ordering and phase separation.<sup>99</sup> DPE works as a theta solvent for photovoltaic polymers, assisting in the formation of optimal bulk-heterojunction film morphologies and reducing bimolecular charge recombination.<sup>100</sup>

In comparisons of alkoxy and alkylthienyl attached to the BDT unit in previous studies, it has been reported in the literature that the PCE value increased with the addition of the alkylthienyl group; however, in this study, the polymer P-FBDT with the alkylthienyl group had the highest PCE value. It should be noted that the polymeric backbone planarity, molecular packing, and film shape all significantly impact the performance of OSC devices; as a result, altering the side chain is a challenging subject. This study shows that polymer structure is not the only factor affecting PCE value; molecular weight and morphology also play an important role. Morphological analyzes will be processed with TEM images in the next section. The EQE measurement was performed to verify the value of the current density on the J-V curve and is shown in Figure 4.4 b. The integration of the EQE curves which are specified in the parentheses agrees with the  $J_{SC}$  value in Table 4.2.

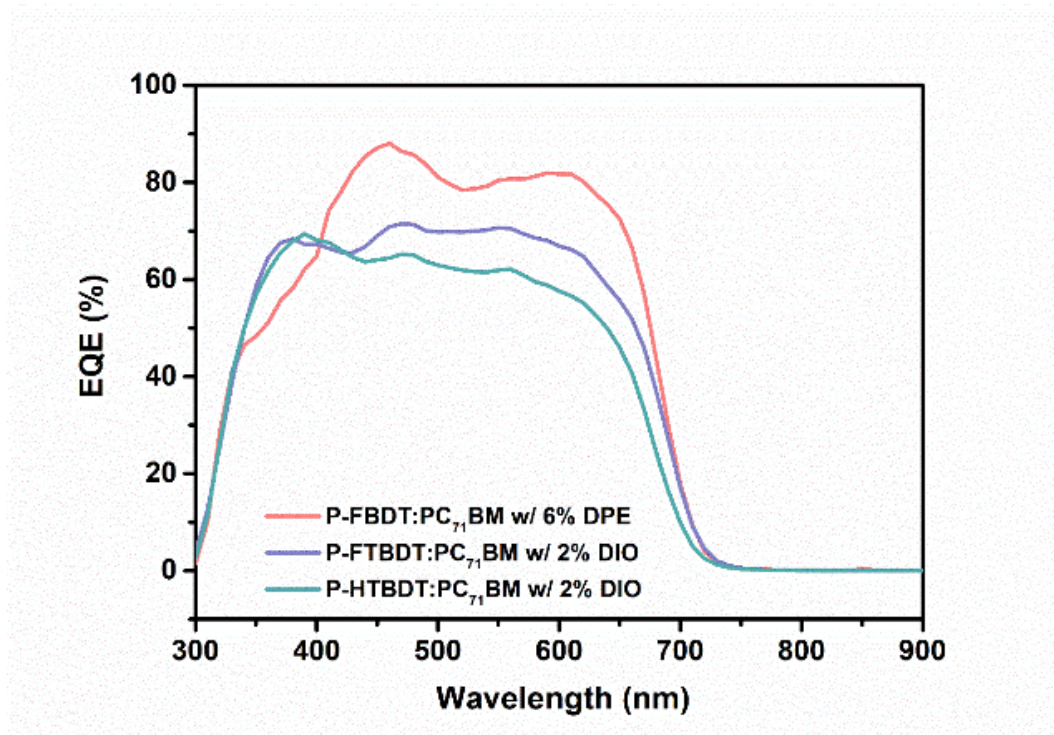
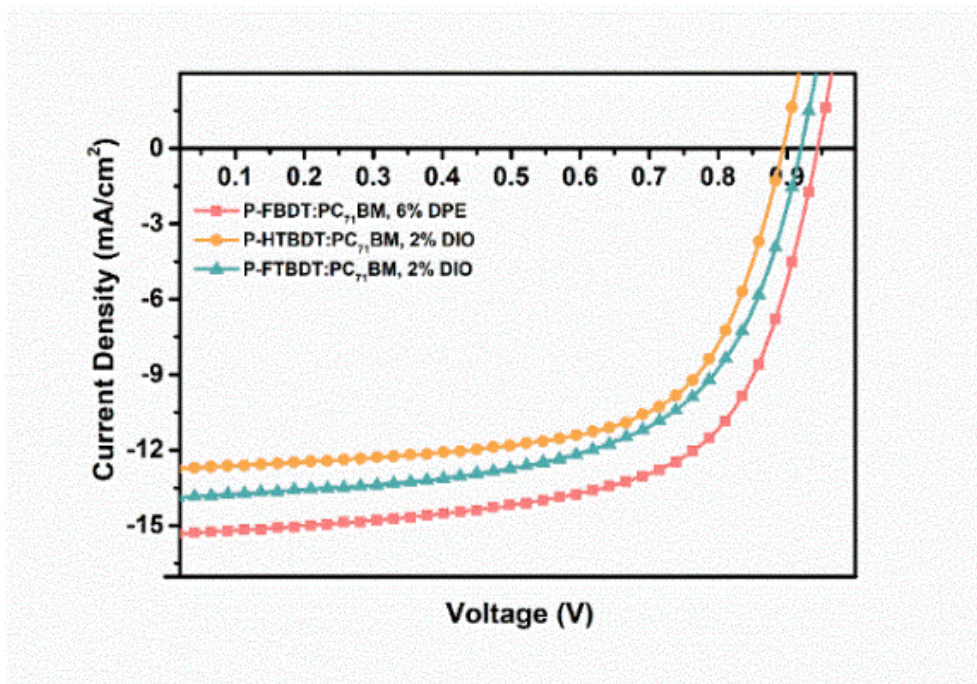


Figure 4.4 J-V curves and EQE characteristics that summarize photovoltaic performance of P-HTBDT, P-FTBDT and P-FBDT.

In order to describe the charge-recombination kinetics of the OSCs, the  $J_{SC}$  of each device was measured as a function of the illumination intensity  $P_{light}$  (Figure 4.5). In theory, the  $J_{SC}$  values of OSCs are proportional to the light intensity  $P_{light}$ .<sup>101,102</sup> Weak bimolecular recombination in the devices might provide a linear relationship between  $J_{SC}$  and  $P_{light}$ ; the slope  $\alpha$  is almost equal to 1. P-FBDT-based OSC exhibits the least bimolecular recombination compared to P-HTBDT-based OSC. P-HTBDT-based OSC exhibits the highest bimolecular recombination.

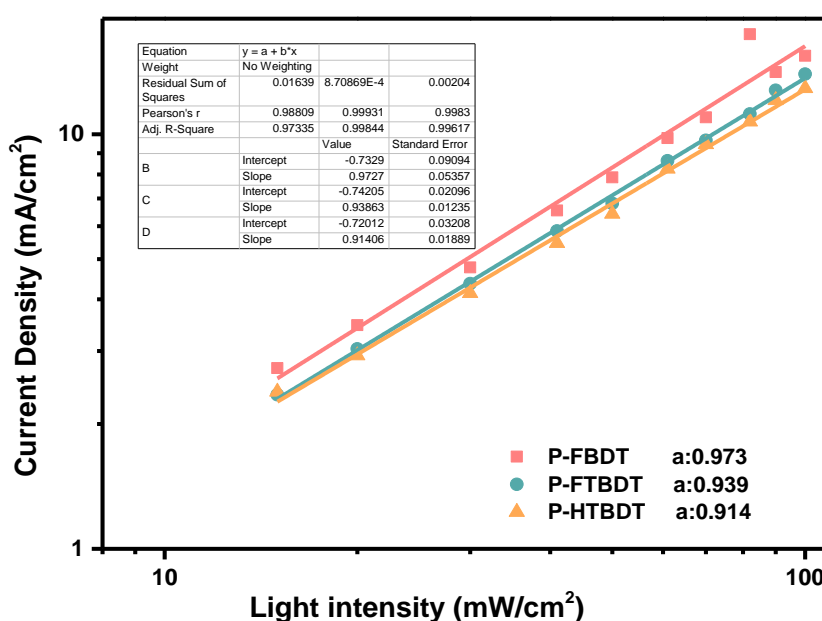


Figure 4.5 Natural logarithm of current density vs. light intensity characteristics for devices based on P-HTBDT, P-FTBDT and P-FBDT based OSCs

An expression for the open-circuit voltage  $V_{oc}$  is obtained by setting the current to zero in the Shockley equation<sup>103</sup>:

$$V_{oc} = n_{idL} \frac{k_B T}{q} \ln \left( \frac{j_{ph}}{j_s} + 1 \right)$$

$q$  the unit charge,  $T$  the temperature,  $k_B$  the Boltzmann constant,  $n_{idL}$  is the light ideality factor,  $j_{ph}$  the photocurrent and  $j_s$  the dark saturation current.

The slope of the  $V_{OC}$  vs logarithm of light intensity graph allows to assess the degree of trap-assisted recombination in the devices (Figure 4.6). Where  $k_B$  is Boltzmann's constant,  $T$  is absolute temperature, and  $q$  is elementary charge, the slope of  $k_B T/q$  indicates whether or not trap-assisted recombination is the predominant process.  $V_{OC}$  is highly sensitive on light intensity for trap-assisted or Shockley-Read-Hall recombination, with a slope of  $2.k_B.T/q$ .<sup>101,102,104</sup> Slope values that are closer to “1” suggest that there is more ideal recombination, while slope values that are larger than “1” indicate that there is more trap-assisted recombination occurring in the device.<sup>104,105</sup> While the same slope (1.58 kT/q) was observed for P-FBDT and P-FTBDT-based OSCs, the  $V_{OC}$  value of P-HTBDT-based OSCs was more reliant on light intensity than that of the others. The high slope value obtained from the P-HTBDT-based OSC (2.04 kT/q) indicates that monomolecular or trap-based recombination occurs more frequently in this device. This finding may explain why P-HTBDT underperformed.

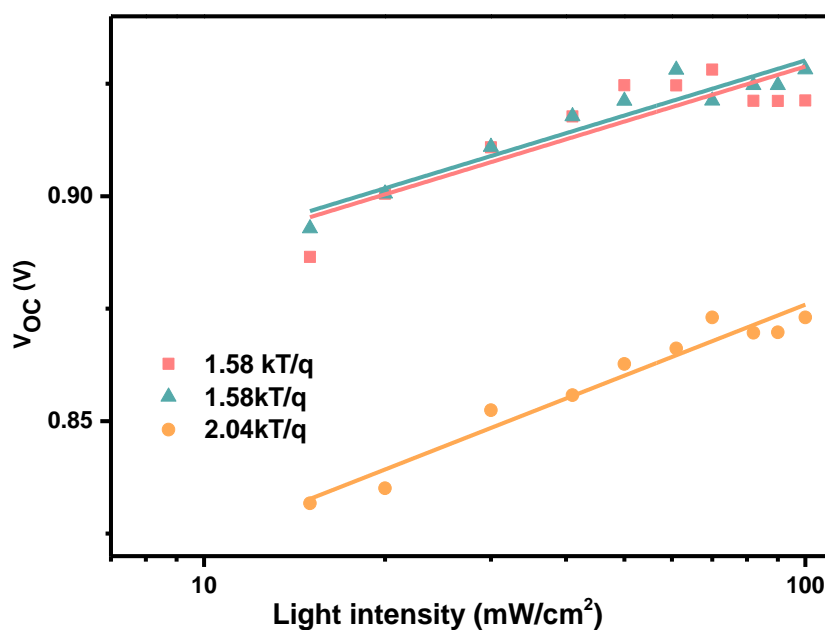


Figure 4.6 Open-circuit voltage vs. natural logarithm of light intensity characteristics for devices based on P-HTBDT, P-FTBDT and P-FBDT based OSCs.

### 4.3.3 Morphological Studies

For morphological and topographical examinations of active layers of P-HTBDT, P-FTBDT, and P-FBDT based OSCs, transmission electron microscopy (TEM) and atomic force microscopy (AFM) were utilized.

Figures 4.7a and 4.7b show TEM images of the optimized active layer of P-HTBDT and P-FTBDT, respectively, when the additive DIO is not used. The dark areas correspond to PCBM-rich regions, whereas the bright regions correspond to polymer-rich areas. These images have PCBM aggregations when viewed at the 50 nm scale. Diiodooctane (DIO) preferentially dissolves PCBM aggregates, according to the literature. The films created with the addition of 2% DIO, as shown in Figures 4.7d and 4.7e, underwent a drastic change due to the additive

inclusion. The interpenetrating bicontinuous network was seen after DIO was added, and the interpenetrated network shape allows superior exciton separation and charge transport, resulting in greater  $J_{sc}$ . When the polymer P-FBDT was utilized in the active layer, it was discovered that DPE, as compared to DIO, enhanced the film formed by this polymer. Figure 4.7f depicts the film obtained when the solvent additive DPE is used, while Figure 4.7c shows the film morphology without DPE. DPE is a well-known theta solvent; the enthalpy of mixing is equal to zero, making the solution perfect. A considerably more homogenous distribution between the donor and acceptor was observed when DPE was utilized. Ultimately, the polymer donor materials formed the ideal nano-scaled morphology with the acceptor in the blend.

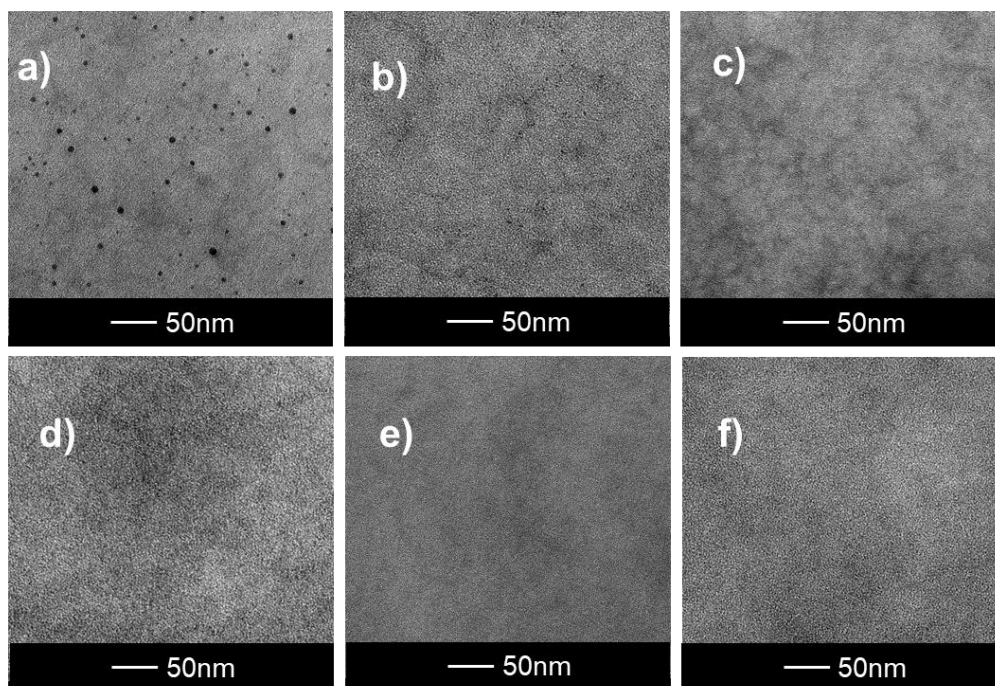


Figure 4.7 TEM images of a) P-HTBBDT : PC<sub>71</sub>BM processed from *o*-dcb b) P-FTBBDT :PC<sub>71</sub>BM processed from *o*-dcb with 2% DIO, c) P-FBDT :PC<sub>71</sub>BM processed from *o*-dcb d) P-HTBBDT :PC<sub>71</sub>BM processed from *o*-dcb with 2% DIO e) P-FTBBDT: PC<sub>71</sub>BM processed from *o*-dcb with 2% DIO f) ) P-FBDT :PC<sub>71</sub>BM processed from *o*-dcb with 6% DPE



The AFM images of the films are shown in Figure 4.8. The root mean square values of the films are located at the left bottom of each image. P-FBDT: PCBM with 6% DPE has the highest RMS value of 2.28 in Figure 4.8f, explaining why film P-FBDT based OSCs have the highest  $J_{SC}$ . Increased surface roughness in the active layer may increase the surface area of the device, internal reflection and light collecting, enhancing device efficiency.<sup>106–108</sup> The addition of the solvent additive causes the roughness values to increase or decrease, and there is no clear association between the roughness value and PCE. For all three polymers, the thickness of the film increased with the addition of an additive without any significant change in the roughness value. Thickening the film generates more significant absorption, resulting in a higher  $J_{SC}$  value. It is not unexpected that a thicker film is formed because the donor-acceptor blend is viscous due to the additives. It is believed that the active layer morphology of the solar cells fabricated for this study has almost reached its ideal based on the results of the AFM and TEM.

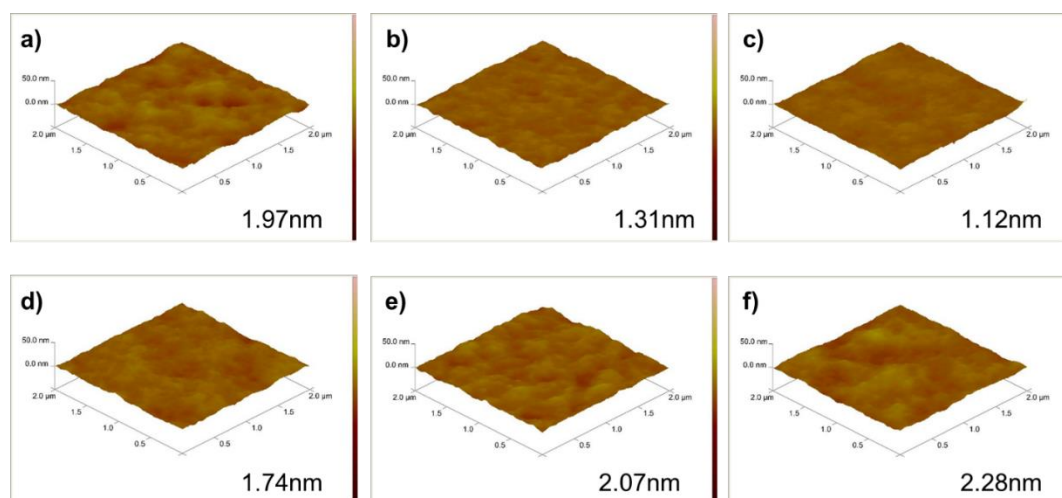


Figure 4.8 AFM images of a) P-HTBDT :PC<sub>71</sub>BM processed from *o*-dcb b) P-FTBDT :PC<sub>71</sub>BM processed from *o*-dcb with 2% DIO, c) P-FBDT :PC<sub>71</sub>BM processed from *o*-dcb d) P-HTBDT :PC<sub>71</sub>BM processed from *o*-dcb with 2% DIO e) P-FTBDT: PC<sub>71</sub>BM processed from *o*-dcb with 2% DIO f) ) P-FBDT :PC<sub>71</sub>BM processed from *o*-dcb with 6% DPE.

#### 4.4 Conclusion

The electrochemical, optical and photovoltaic properties of BDT and TPD containing three different polymers P-HTBDT, P-FTBDT and P-FBDT were investigated in this study. Beginning to end, the effects of fluorine groups attached to benzothiadiazole groups and alkoxy and alkylthienyl groups attached to benzodithiophene groups were examined in the study. In completed devices, P-FTBDT and P-FBDT yielded deeper HOMOs and higher  $V_{OC}$ 's than P-HTBDT, which lacks fluorine atoms, according to the scientific literature. This study also compares monofluorinated P-FBDT to its difluorinated counterpart, PF. P-FBDT, with values of 9.21% PCE, 60.33 FF, and 0.95V  $V_{OC}$ , exhibited the greatest photovoltaic performance among the synthesized polymers. Morphological and topographic examinations confirmed the reliability of the data. This study demonstrates that molecular weight and morphology are significant contributors to PCE value in addition to polymer structure.

## CHAPTER 5

### RATIONAL MOLECULAR DESIGN ENABLES EFFICIENT BLUE TADF– OLEDs WITH FLEXIBLE GRAPHENE SUBSTRATE

*This study has been published in Advanced Functional Materials.*

*Eda Alemdar\*, Parisa Sharif\*, Soner Ozturk, Omer Caylan, Tugba Hacıfendioglu, Goknur Buke, Murat Aydemir, Andrew Danos, Andrew P. Monkman, Erol Yildirim, Gorkem Gunbas, Ali Cirpan, Ahmet Oral, 2022. Rational Molecular Design Enables Efficient Blue TADF–OLEDs with Flexible Graphene Substrate. Adv. Funct. Mater., 32, 2207324.*

*\*The authors are equally contributed in this work*

#### 5.1 Introduction

Due to their processability, flexibility, pure color emission, low cost, low turn-on voltages, and high efficiency, organic conjugated molecules are excellent candidates for replacing their inorganic counterparts in color display technology.<sup>109</sup> Optoelectronic performance of highly effective OLEDs relies on the efficient exploitation of electrically produced non-emitting triplet excitons. Phosphorescent materials using heavy metals such as Ir and Pt enhance  $H_{SO}$  to permit direct triplet emission, while thermally active delayed fluorescence (TADF) enabled by an efficient  $R_{ISC}$  turns triplets back into emissive singlet excitons.<sup>110</sup> Appropriate heavy metals for use in efficient OLEDs have a number of disadvantages, including their unsuality and increased cost, their potential as pollutants, and the short operational lifetimes of blue emitters due to their weak metal-ligand bonds, all of

which hinder their widespread industrial application and prompted the development of TADF materials.<sup>111</sup> In addition to high efficiencies, one of the distinctive characteristics of OLEDs compared to other illumination sources is the ability to create flexible devices; thus, the OLED community has paid considerable attention to alternate flexible anodes and substrates in recent years.<sup>112,113</sup>

In this chapter, a new TADF emitter family with donor-incorporated selenium vertically connected to a number of acceptor units was developed and fabricated to concurrently boost  $H_{SO}$  and reduce  $\Delta E_{ST}$ . The method yielded increased EQEs in comparison to TADF emitters without heavy atom use. Notably, one of the variants resulted in near 20% pure blue emission EQEs.

## 5.2 Experimental

### 5.2.1 Molecular Design of TADF Molecules

The design approach suggests that increasing  $H_{SO}$  while retaining  $\Delta E_{ST}$  should increase  $\lambda$ , hence speeding RISC rate.

$$\lambda = \frac{H_{SO}}{\Delta E_{ST}}$$

$\lambda$  is the first-order mixing coefficient,  $\Delta E_{ST}$  is the energy gap between the S and T states that are being considered, and  $H_{SO}$  is the value of the spin-orbit coupling (SOC).

Therefore, we meticulously chose high-performance phenoxazine-based TADF materials already described in the literature and replaced the oxygen atoms in D units with selenium atoms, which have much higher  $H_{SO}$  than oxygen.<sup>114</sup> The structures and the synthetic pathway of synthesized three small molecules, SeDF-G, SeDF-YG and SeDF-B, containing phenoselenazine, are given in Figure 5.1. The use of large chalcogens was considered out since prior research has shown that the long-term buildup of the corresponding anions of the chalcogens at metal

contacts has a negative effect on OLED performance.<sup>115</sup> The literature emphasizes that the effects of heavy chalcogens in OLEDs are still not fully understood due to the lack of device-centered studies.<sup>116,117</sup> In 2019, Monkman et al. synthesized a D-A-D type TADF molecule using the same donor group used in this study and replaced the sulfur in the donor unit of the molecule with selenium,<sup>118,119</sup> causing dual emission.<sup>120</sup> In the above-mentioned study, it was observed that there was not much heavy atom effect on TADF as the Se atom allowed for more significant structural changes that opened up the CT emission from a different axial/ equatorial conformer. However, using selenium atom in this study significantly improved the TADF properties, and the heavy atom effect was revealed.

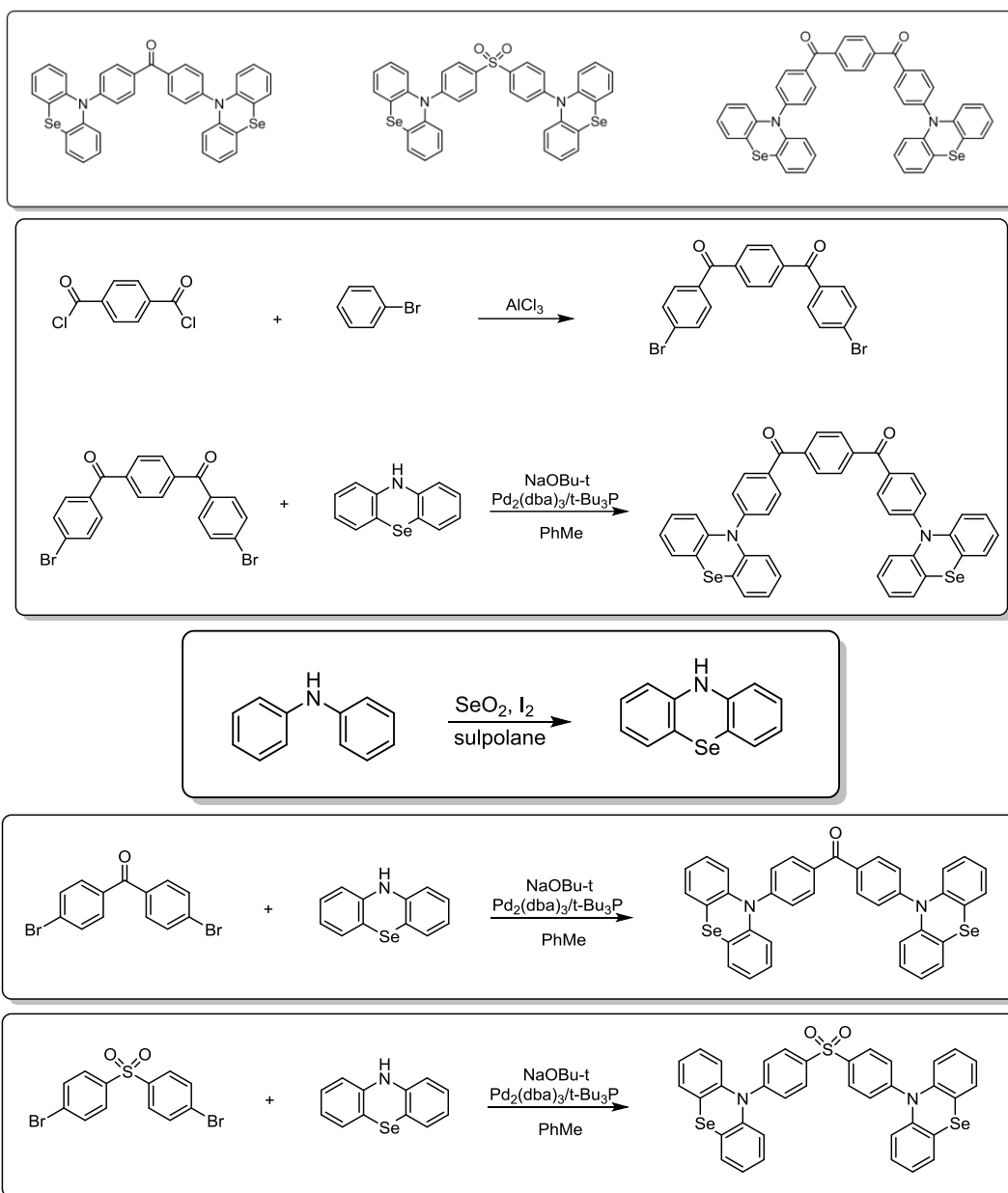


Figure 5.1 Structures and the synthetic pathway of synthesized TADF molecules, SeDF-G, SeDF-B and SeDF-YG, respectively.

## 5.3 Results and Discussion

### 5.3.1 Optical and Photoluminescence Properties

Ultraviolet-visible (UV-Vis) absorption and photoluminescence (PL) spectra of SeDF-G, SeDF-B, and SeDF-YG are given in chloroform solution (Figure 5.2), with various emission bands due to the different acceptor strengths.

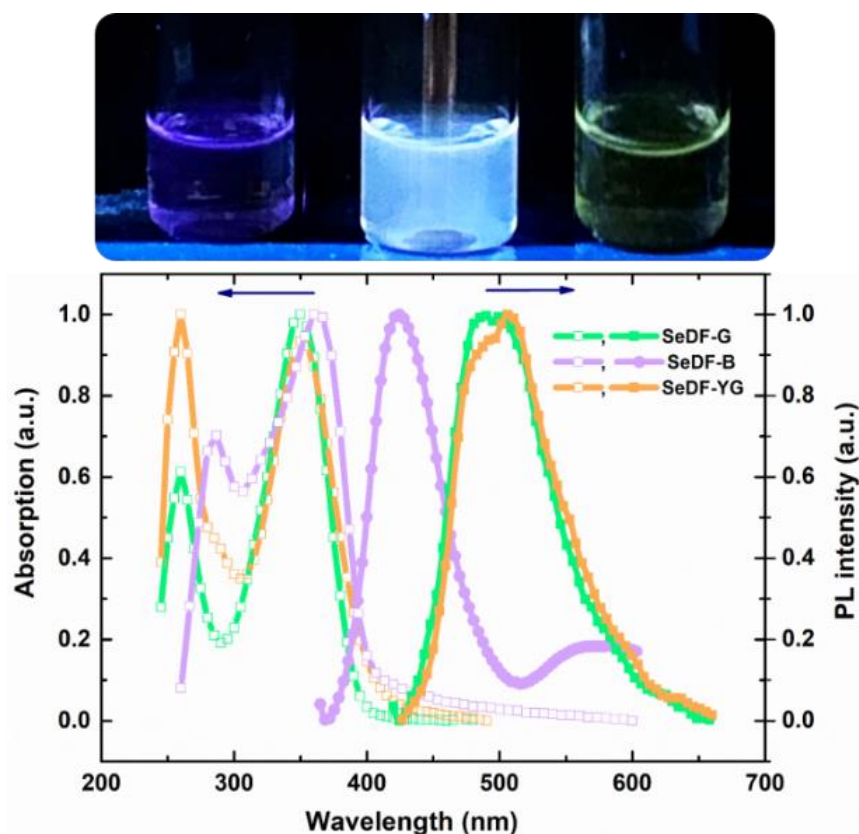


Figure 5.2 Luminescence images of SeDF-G, SeDF-B, and SeDF-YG in chloroform recorded under UV irradiation at  $\lambda_{\text{ex}}=365$  nm (above), normalized absorption (dashed line) and photoluminescence (PL, solid line) spectra of SeDF-G, SeDF-B and SeDF-YG in chloroform at room temperature (below).

Figure 5.3 shows the PL and phosphorescence (PH) spectra of the molecules in drop-cast films at room temperature (RT) and 80 K (10% w/w loading in mCBP

host), respectively. The blueshifted PH spectra for all three materials are nearly identical, and so most likely arise from the common D unit. The PL spectra occur at longer wavelengths than time-resolved PH (80 K, 80 ms delay) in the films, so we attribute the PH to a higher LE triplet state while the PL comes from a lower energy charge transfer (CT) state. Se-B has a weaker A unit, which results in blueshifted emission ( $E_S=2.84$  eV), but Se-G and Se-YG have approximately comparable  $E_S$  values ( $E_S=2.71$  eV). From the onsets of the PL and PH spectra,  $\Delta E_{ST}$  is smaller for Se-B ( $E_{ST}=0.08$  eV) and larger for Se-G and Se-YG molecules ( $E_{ST}=0.15$ eV).

The time-resolved emission spectra and intensity decays for the films were recorded as previously described<sup>121</sup> and are shown in Figure 5.3b, with representative individual spectra (and contours of the normalized time-resolved spectra) shown in Figure 5.4. Similar spectra and decays at 80 K are shown in appendix, revealing the phosphorescence spectrum, with significantly suppressed delayed fluorescence observed at lower temperatures. The decays were also fit entirely using a kinetic model,<sup>122</sup> as well as with double exponentials across the separate prompt fluorescence (PF) and delayed fluorescence (DF) time regimes, with fitting parameters given in Table 5.1.



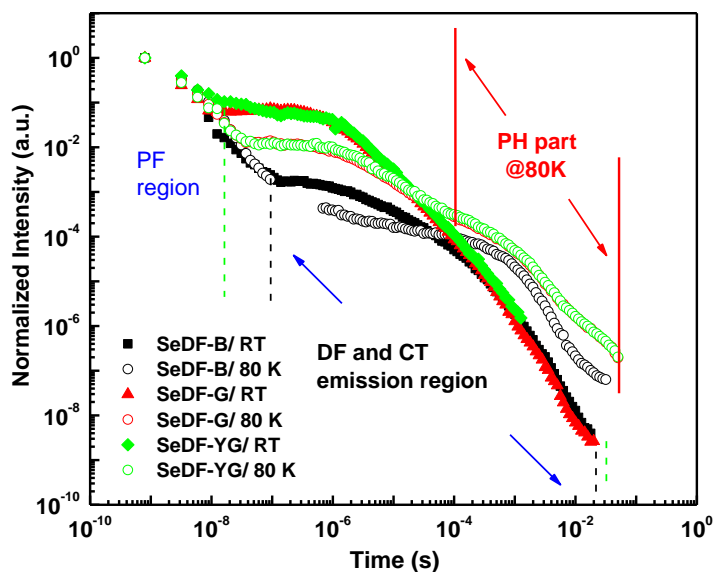
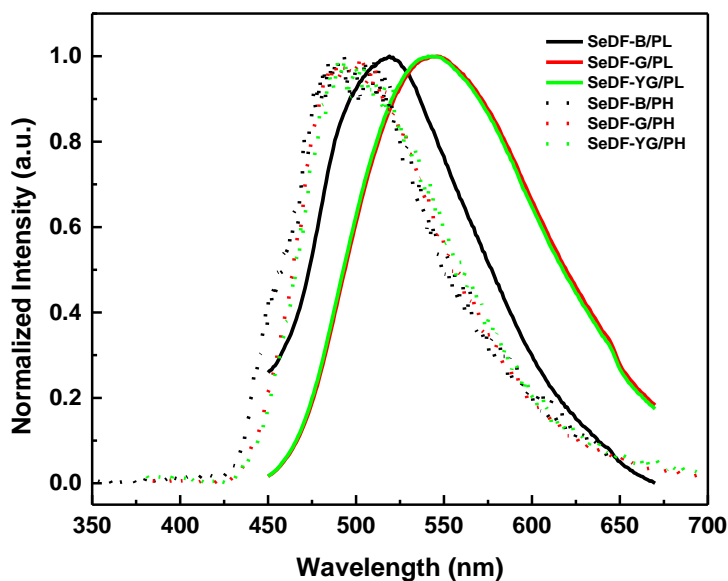


Figure 5.3 Normalized photoluminescence spectra of Se-B, Se-G and Se-YG molecules in 10% mCBP drop-cast films at RT. Phosphorescence spectra were taken at 80 K at >80 ms delay after pulsed excitation. (above) Photoluminescence decay kinetics of the same films at RT (under vacuum) and at 80 K (under dry nitrogen). (below)

Table 5.1 Decay parameters  $k_f$ ,  $k_{ISC}$ ,  $k_{rISC}$  and lifetimes from kinetic fitting of decays

	$k_f (x 10^7/s)$	$k_{ISC} (x 10^7/s)$	$k_{rISC} (x 10^6/s)$	$\tau_{prompt} (ns)$ <sup>[a]</sup>	$\tau_{delayed} (\mu s)$ <sup>[a]</sup>
SeDF-B	1.98	9.88	0.59	$\tau_1=2.47$ $\tau_2=8.6$ $\tau_{ave}=3.0$	$\tau_1=6.45$ $\tau_2=133$ $\tau_{ave}=18.5$
SeDF-G	0.49	9.22	5.69	$\tau_1=1.44$ $\tau_2=18.8$ $\tau_{ave}=1.5$	$\tau_1=3.1$ $\tau_2=90$ $\tau_{ave}=3.9$
SeDF-YG	0.27	9.7	10.6	$\tau_1=6.46$ $\tau_2=38.7$ $\tau_{ave}=9.7$	$\tau_1=3.6$ $\tau_2=95$ $\tau_{ave}=4.6$

<sup>[a]</sup> Lifetimes, and their weighted averages from double exponential fitting of either PF or DF regions.

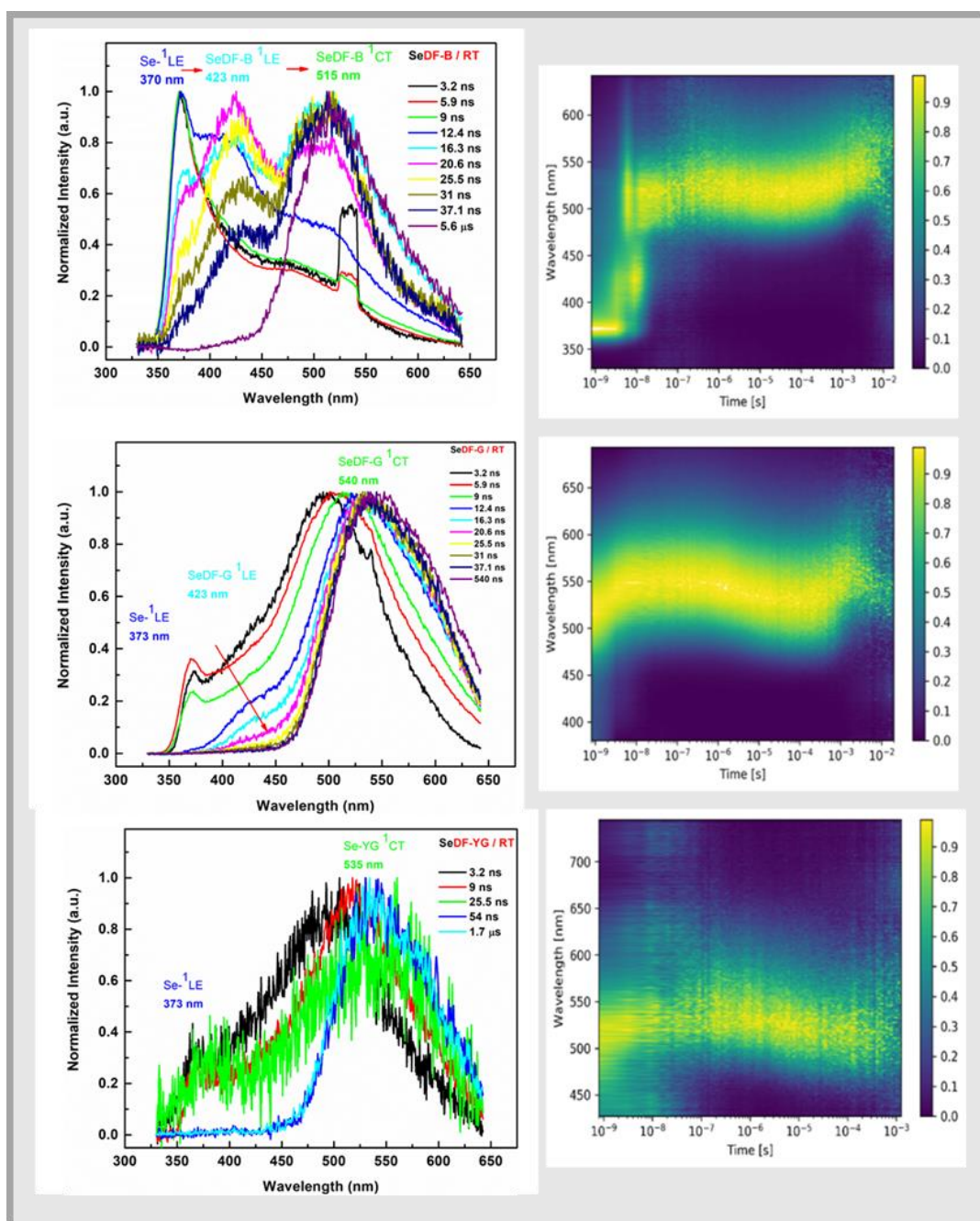


Figure 5.4 Normalized time-resolved spectra at RT (left), with contour plots of normalized time-resolved spectra (right). The emission spectra change from Se-<sup>1</sup>LE- dominated at early times, to redshifted CT-dominated emission at later times

Similar to the steady-state spectra in Figure 5.2, the time-resolved spectra and decays reveal similar TADF performance for **SeDF-G** and **SeDF-YG** (with strongly analogous acceptor units), but significantly different behavior in **SeDF-B**. In **SeDF-B** the PF spectra are in the near-UV region (~350 nm), corresponding to strong LE emission from the D unit. This UV emission decays rapidly, eventually being replaced with strongly redshifted CT emission (~500 nm). The rapid decay of the D emission contributes to the much larger value of  $k_f$  in the fitted decays of the blue emitter, as well as the seemingly lower DF contribution in the normalized decay (Figure 5.4). The same D emission is also observed in the PF of the other two materials, but to a significantly lower extent. Instead for these materials the LE and CT emission occur simultaneously at first, with the CT emission dominating throughout. At intermediate times we also observe an additional CT emission peak at ~425 nm. We suggest that this arises from the higher energy axial conformer in the as-deposited films. This emission is short-lived though, as both energy transfer to nearby axial conformers as well as geometry relaxation in individual molecules will quench this emission band while transferring energy to the equatorial band.

Amongst the other decay parameters, the intersystem crossing rates ( $k_{ISC}$ ) are noted to be rather high in all three materials. In **Se-G** and **Se-YG** this is likely due to the impact of the heteroatom ketone, which is able to generate triplet states efficiently, leading to large DF contributions. Although the ISC is also fast in **Se-B** -possibly due to spin conversion as charges separate from the PF-emissive LE state to form the CT state responsible for DF emission - its lower rate of RISC leads to a lower overall DF contribution. This slower RISC in **Se-B**, despite its smaller  $\Delta E_{ST}$ , further demonstrates that this energy gap is not the sole determining factor in predicting TADF performance.<sup>123,124</sup>

### 5.3.2 Computational Studies

Assist. Prof. Dr. Erol Yıldırım performed the computational studies for this section of the thesis. Planar or orthogonal conformations correspond to quasi-axial (*a*) and quasi-equatorial (*e*) conformers, respectively, among the two lowest energy structures determined for the proposed TADF materials. Although quasi-axial conformers have a lower energy than quasi-equatorial conformers by 0.1-0.2 eV, both structures have been found experimentally, as evidenced by prior researches.<sup>125-128</sup>

This suggests that TADF materials with selenium-substituted phenoxazine (Se-PXZ) derivatives may exhibit multiple conformations owing to the variation in C-N and C-Se bond lengths in the D group, as previously reported for the difference between P-N and P-Se bond lengths in P-N and P-TZ. The almost orthogonal equatorial conformers caused the lower energy excited states to have a smaller EST, whereas the axial conformers had a greater singlet state energy level, a stronger oscillator frequency, and more traditional fluorescence properties. In addition, axial conformations possess deeper HOMO and greater LUMO levels than the other two structures, resulting in more energetic S<sub>0</sub>-S<sub>1</sub> and S<sub>1</sub>-T<sub>1</sub> transitions.

Beneficial to TADF materials, equatorial conformations have reduced S<sub>0</sub>-S<sub>1</sub> and S<sub>1</sub>-T<sub>1</sub> ( $\Delta E_{ST}$ ) transition energies.  $\Delta E_{ST}$  was predicted to be less for SeDF-Be than for SeDF-Ba due to the fact that the singlet-triplet gap increases with increased overlap of the frontier orbitals. Due to electron delocalization, the axial conformations exhibit extensive delocalization with high HOMO-LUMO overlap. As expected for TADF materials, highly localized HOMO and LUMO orbitals and a significant charge density differential between D and A were instead reported for the equatorial conformers.

Table 5.2 The electrical and structural characteristics of SeDF-G, SeDF-B, and SeDF-YG, as well as the influence of phenoxazine (ODF) and phenothiazine (SDF) replacements, as calculated by DFT. Calculations for dipole and polarizability are expressed in Debye and a.u., respectively. In parentheses are calculations based on the Perdew–Burke–Ernzerhof (PBE0) functional.

	<b>HOMO</b>	<b>LUMO</b>	$\Delta E_{S0-S1}$	$\Delta E_{S0-T1}$	$\Delta E_{T1-S1}$	$\Delta E_{T2-S1}$	$\Delta E_{T2-S2}$	$\Delta E_{T1-T2}$
<b>SeDF-Ga</b>	-5.64 (-5.85)	-1.53 (-1.35)	3.33 (3.31)	2.85 (2.85)	0.48 (0.46)	0.33 (0.30)	0.56 (0.69)	0.15 (0.16)
<b>SeDF-Be</b>	-5.54 (-5.74)	-2.21 (-2.10)	2.79 (2.93)	2.76 (2.87)	0.03 (0.06)	-0.27 (-0.12)	0.31 (0.47)	0.30 (0.13)
<b>SeDF-Ba</b>	-5.73 (-5.94)	-1.30 (-1.14)	3.47 (3.38)	3.20 (3.15)	0.27 (0.23)	0.13 (0.10)	0.46 (0.65)	0.14 (0.13)
<b>SDF-Be</b>	-5.53 (-5.94)	-2.25 (-2.13)	2.73 (2.89)	2.71 (2.84)	0.02 (0.04)	-0.27 (-0.10)	0.31 (0.50)	0.30 (0.50)
<b>SDF-Ba</b>	-5.74 (-5.98)	-1.30 (-1.14)	3.47 (3.38)	3.19 (3.15)	0.28 (0.24)	0.14 (0.11)	0.47 (0.65)	0.14 (0.13)
<b>ODF-Be</b>	-5.33 (-6.31)	-2.30 (-2.15)	2.46 (2.46)	2.45 (2.62)	0.01 (0.02)	-0.37 (-0.19)	0.23 (0.43)	0.38 (0.21)
<b>SeDF-YG</b>	-5.82 (-6.03)	-2.09 (-1.93)	3.01 (3.02)	2.45 (2.62)	0.29 (0.28)	0.26 (0.23)	0.56 (0.69)	0.03 (0.04)

	$\mu$	$\alpha$	$\beta$	$\lambda_{\text{hole}}$	AIP	VIP	VEA	$\delta_{\text{acceptor}}$
<b>SeDF-G</b>	4.14	538.00	2519.67	0.13	6.60	6.67	-0.44	0.44
<b>SeDF-Be</b>	3.29	527.52	111.80	0.39	6.35	6.54	-1.00	0.93
<b>SeDF-Ba</b>	6.92	528.21	1136.02	0.15	6.68	6.76	-0.36	0.27
<b>SDF-Ba</b>	6.72	514.47	1362.42	0.16	6.68	6.78	-0.36	0.24
<b>SDF-Be</b>	2.98	513.78	25.33	0.41	6.33	6.53	-1.03	0.76
<b>ODF-Be</b>	2.80	483.46	24.95	0.17	6.24	6.34	-1.05	0.07
<b>SeDF-YG</b>	0.00	643.96	1.00	0.13	6.65	6.71	-0.95	0.39

As a consequence of theoretical calculations, we identified two major discrepancies resulting from the heavy ion impact while utilizing phenoxazine (PXZ), phenothiazine (S-PXZ or PTZ), and phenoselenazine (Se-PXZ or PSeZ) derivatives for the blue OLED TADF material. First is the structural difference, where it has been observed that whereas phenoxazine prefers equatorial conformation, phenothiazine and phenoselenazine derivatives have multiple conformations, resulting in dual emission owing to energy transfer between conformations.<sup>125,126,129</sup> In addition to the axial and equatorial variations, sulfur and selenium atoms favor to position significantly out of the aromatic plane compared to the planar phenoxazine, which increases the number of possible conformations with energy differences as small as the thermal energy of the room temperature, which are depicted as two distinct axial conformations in appendix.

The second contribution provided by the heavy atom effect is sourced from electronic effects. The percentage of HOMO on the acceptor center increases, while percentage of the LUMO on the acceptor decreases with the heavy atom effect. Dipole moment, polarizability and hyperpolarizability increase generally in the order of O, S, Se. Positive atomic charges based on the electrostatic potential

fitting is increased on the acceptor center and negative charge on the donor that means stronger electron density donating potential by sulfur and selenium substitution. The most significant enhancement is improvement in theoretically calculated  $k_{RISC}$  especially for the equatorial conformation of the phenothiazine and phenoselenazine substituted TADF materials determined for different  $\lambda_M$  values for  $T_1 \rightarrow S_1$  transition. The origin of this enhancement is determined mainly as the enhancement of  $H_{SO}$ , spin orbit coupling matrix element, that show more than tenfold increase by the replacement of O with Se atom.<sup>130</sup> Our results presented that structures only with equatorial conformations show significant improvement for  $k_{RISC}$  leading to the TADF properties (Table 5.3).  $k_{RISC}$  is significantly lower for the more stable axial conformations. This indicates multi-conformational structure by heavy atom substitution leading to the classical fluorescence by axial conformations and TADF type emission by equatorial conformations that enhance EQE. Although percentage of the equatorial conformation responsible for the TADF properties decreases by PSeZ substitution, the efficiency is much higher due to the tremendous enhancement in the spin orbit coupling and dual emission by energy transfer between conformations. Table 5.3  $k_{RISC}$  for  $T_1 \rightarrow S_1$  transitions and the  $\Delta E_{S_1-T_1}$  and  $H_{SO}$  parameters used for the calculation of  $k_{RISC}$ .

	$\Delta E_{S_1-T_1}$ (eV)	$H_{SO}$ (cm <sup>-1</sup> )	$k_{RISC}$ ( $\lambda_M=0.1$ eV)	$k_{RISC}$ ( $\lambda_M=0.2$ eV)
<b>O-DF-Be</b>	0.01	9.2	2.13E+10	5.72E+09
<b>S-DF-Be</b>	0.02	21.4	9.22E+10	2.51E+10
<b>S-DF-Ba</b>	0.28	3.1	6.21E+03	7.52E+04
<b>Se-DF-Be</b>	0.03	90	2.35E+12	6.56E+11
<b>Se-DF-Ba</b>	0.27	3.6	1.74E+04	1.61E+05
<b>Se-DF-Ge</b>	0.01	110	4.42E+12	1.21E+12
<b>Se-DF-Ga</b>	0.48	4.1	8.35E-05	1.65E+00
<b>Se-DF-YGe</b>	0.02	52	1.10E+12	3.00E+11
<b>Se-DF-YGa</b>	0.29	2.9	2.57E+03	4.11E+04



According to theoretical calculations, all three materials would possess dual conformations including a quasi-axial conformer with classical fluorescence emission behavior and a quasi-equatorial conformer with TADF characteristics that was further supported by the natural transition orbitals for the first singlet and triplet excitations. Improved planarity of the donor unit was observed for these excitations. Among equatorial conformers, SeDF-Ge exhibits higher molar absorptivity<sup>125,126</sup>

We concluded that similar to the previous studies conducted for PTZ,<sup>[34–36]</sup> having a nonplanar six-membered phenothiazine ring leading to a high EQE due to the presence of sulfur atom; efficient OLED materials can also be designed by selenium substitution in PTZ to utilize control of dual conformations. Dual emission and energy transfer between these two conformations could combine due to the structural and electronic heavy atom effect by the selenium atom leading to enhanced performance in TADF-OLED materials.<sup>131</sup>

### 5.3.3 Fabrication and Characterizations of TADF OLEDs

The ITO coated glass substrate is used as the anode, and the device architecture is Glass/ITO/  $\alpha$ -NPD (40nm)/EML(20nm)/TPBI(40nm)/LiF(0.6nm) /Al(100nm). ITO coated glass substrates were first washed in an ultrasonic bath for 15 minutes with Hellmanex detergent, distilled water, isopropyl alcohol and acetone. Afterwards, oxygen plasma was applied for 15 minutes in order to overcome the energy barrier between ITO's work function and  $\alpha$ -NPD. Oxygen plasma is applied to remove residual organic impurities, to reduce the surface tension of ITO and to increase the work function of ITO. The applied oxygen plasma time has been optimized and the times used during the optimization are given in Figure 5.5. The 15-minute oxygen plasma was chosen because it had a significantly lower turn-on voltage than other durations, which indicates a successful hole injection.

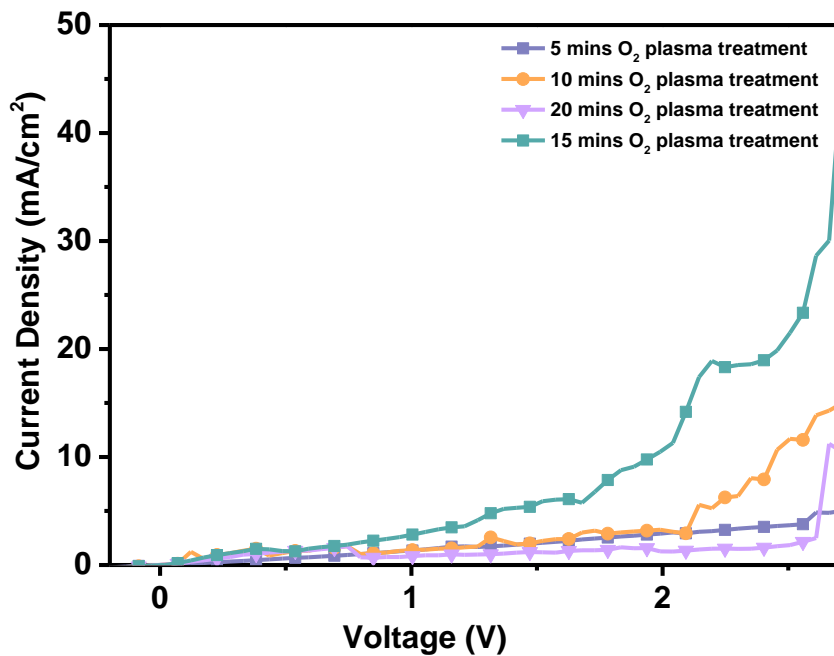


Figure 5.5 The duration of applied oxygen plasma. After the oxygen plasma treatment, the substrates were transferred to the thermal evaporator, where each layer's thickness was optimized (HTL, EML and ETL). Due to its high triplet energy of 2.9 eV, aligned HOMO and LUMO energy levels, broad energy bandgap, and good morphological stability, m-CBP was chosen as the host material for all systems.<sup>132</sup>

Table 5.4 Summary of OLED characteristics of champion devices, (average in parenthesis)

Device	Dopant	$L_{MAX}$ ( $cd/m^2$ ) <sup>a</sup>	$\eta_c$ ( $cd/A$ ) <sup>b</sup>	$\eta_{EXT}$ (%) <sup>c</sup>	$V_{on}$ (V) <sup>d</sup>	CIE (x, y) <sup>e</sup>
A	SeDF-G	17007 (16896)	64.0	30.8	4.3	(0.31,0.53)
C	SeDF-B	9662 (9641)	27.3	25.6	5.8	(0.17, 0.14)
E	SeDF-YG	16833 (16697)	73.5	18.8	5.4	(0.33, 0.48)
Ref <sup>[116]</sup>	Px2BP*	86100	35.9	10.7	3.2	(0.37, 0.58)
Ref <sup>[116]</sup>	P- PxBBP**	57120	20.1	6.9	3.6	(0.49, 0.51)

<sup>a</sup>((Peak luminance)); <sup>b</sup>((Peak current efficiency)); <sup>c</sup>((Peak external quantum efficiency (%))); <sup>d</sup>((The operating voltage at a brightness of  $1cd/m^2$ )); <sup>e</sup>((Commission International L'Eclairage coordinates at  $\sim 1000cd/m^2$ ));

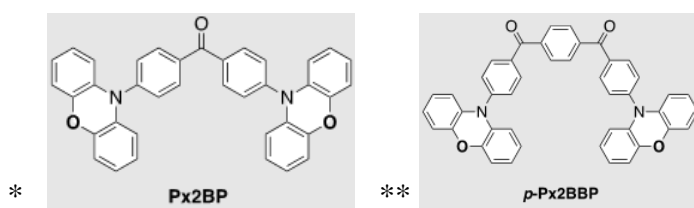


Figure 5.6 depicts the EQE-current efficiency against Voltage and I-V-J graphs for the constructed devices, while Table 5.4 provides a summary of the major findings. 10% (v/v) of emitter dopant was scattered in order to avoid exciton annihilation and high current density, and to provide a direct comparison to the photophysical data obtained with the same host and doping ratio.

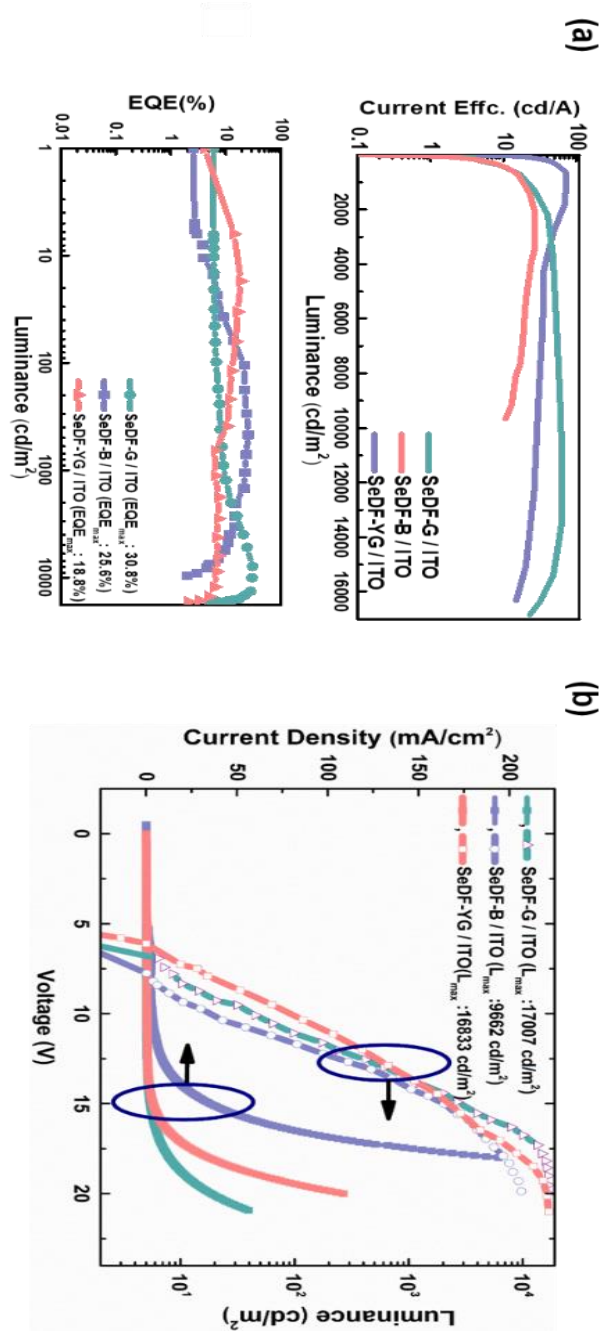


Figure 5.6 a) Current efficiency vs. luminance and EQE(%) vs. luminance characteristics of fabricated OLEDs, b) Current density–voltage–luminance (J–V–L) characteristics of ITO-based OLEDs.

Photographs of the operational devices are depicted in Figure 5.7a, while the color coordinates (x,y) are indicated on the chromaticity diagram in Figure 5.7b. Among all device designs, SeDF-G-based OLEDs had the highest measured EQE value (30.8% maximum). This study demonstrates the influence of spin orbit coupling via EQE values, since the greatest EQE values for sulfur-substituted compounds could not surpass 20% EQE.<sup>125,126</sup> This discovery correlates with the reduced current density values reported for the aforementioned device design when it is in operation. In addition, better hole injection from the anode to the emissive layer in SeDF-G/ITO may be another cause for the lower turn-on voltage of SeDF-G/ITO.

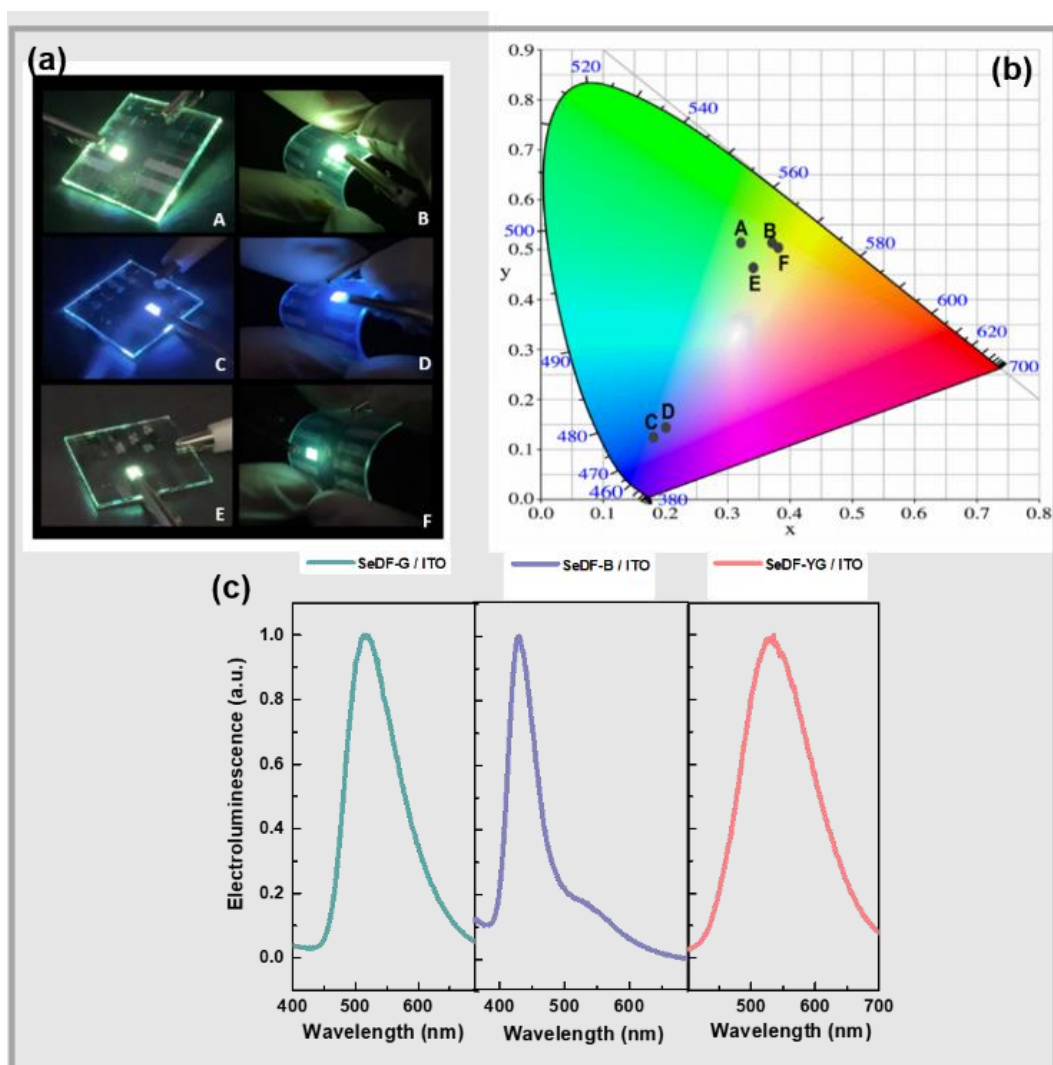


Figure 5.7 (a) Photographs, (b) color coordinates on chromaticity diagram and (c) electroluminescence spectrum of fabricated OLEDs

According to Figures 5.6 and 5.4, when SeDF-B is utilized as the emitting dopant, the EQE values of OLEDs deteriorate fast once they reach high luminance. This efficient decrease at high current density is mostly attributable to the accumulation of excessive T1 excitons in the emitting layer, which produces exciton quenching through triplet-triplet and/or singlet-triplet annihilation.<sup>133</sup>

The stability of all devices is evaluated with an initial luminance ( $L_0$ ), 1000 cd/m<sup>2</sup> to determine the operational lifetime (Figure 5.8). For ITO-based devices LT80 values were determined to be 283 h for SeDF-G, 29 h for SeDF-B and 289 h for SeDF-YG where for graphene-based devices LT80s were recorded as 178 h, 10 h, 114 h for SeDF-G, SeDF-B and SeDF-YG respectively. For green and yellow-green emitters LT80 values between 200-500 h were commonly demonstrated in literature which is consistent with our results. However much higher performances have also been realized (over 15000 h) with lower operational  $L_0$ . For blue emitters stabilities are generally much lower with a commonly observed range between 20 and 100 h. Even though significantly high device performance was observed with materials introduced in this work, stability of the devices could still be improved through interface engineering and our work along these lines is currently underway. One important point to note here is the fact that although high doped flexible graphene electrodes were utilized, the stabilities observed for these devices are quite compatible to ITO-based counterparts which is quite encouraging for utilization of these flexible devices in future relevant applications.<sup>129,134-137</sup>

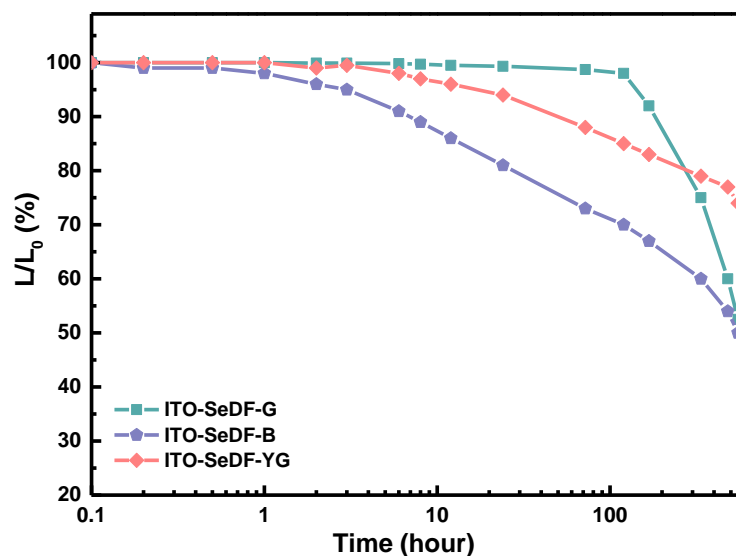


Figure 5.8 Operation lifetime plot of ITO-SeDF-G, ITO-SeDF-YG, ITO-SeDF-B, devices. Lifetime was measured at an initial luminance of  $1000 \text{ cd m}^{-2}$ .

To further support our device results, PLQYs of equivalent films (10% TADF emitter in m-CBP host, under nitrogen in integrating sphere with 330 nm excitation) were investigated. The measured values are surprisingly low considering the efficiency of the devices, at only 2.6%, 7.6%, and 8.5% for SeDF-B, SeDF-G, and SeDF-YG, respectively (Table 5.5). A strong correlation between PLQY and device EQE has been clearly demonstrated in the literature.<sup>138</sup> We believe the possible explanation is that the evaporation of the films causes a difference in the contribution of axial/equatorial conformers, with the more efficient and narrower conformer dominating in the evaporated films. To the best of our knowledge this is the first example where a high energy conformer has been exclusively stabilized in evaporated films. This exclusivity is evident by considering that if a mixture of conformers were present, then FRET would quench all the high energy states.<sup>139,140</sup> We suggest that precisely this occurs in the drop-cast films and in solution, where the efficiency is lower, and the emission band is

lower-energy and broader than the EL of the devices (Figure 5.2 and 5.7c). Further work to determine the conformation differences in the evaporated and drop-cast films is currently underway in our laboratories.

Last but not least, EQEs observed from OLEDs utilizing SeDF-G and SeDF-YG (ITO/Glass) are almost three times higher than devices using their selenium free analogs (Px2BP and *p*-Px2BBP) with practically the same device structures (Table 5.4). This clearly demonstrates the success of the rational design approach introduced in this work, and the efficiency improvements that can be accessed using the heavy-atom effect to improve  $H_{SO}$ .

## 5.4 Conclusion

In TADF systems, the effectiveness of  $R_{ISC}$  is proportional to  $H_{SO}$  and inversely proportional to  $E_{ST}$ . Although numerous strategies for decreasing  $E_{ST}$  have been attempted with great success, the impact is not as straightforward to examine. In this study, TADF materials with heavy-atom selenium inclusion (SeDF-G, SeDF-B, and SeDF-YG) were developed and fabricated. The materials demonstrated outstanding performance, with EQEs exceeding 30% and SeDF-G outperforming both oxygen- and sulfur-based compounds. OLEDs containing SeDF-G and SeDF-YG are about three times efficient than devices containing their selenium-free phenoxazine analogs, while having nearly identical device architectures.



## CHAPTER 6

### TWO COMPATIBLE POLYMER DONORS ENABLING HIGH EFFICIENCY TERNARY ORGANIC SOLAR CELLS

#### 6.1 Introduction

Due to the rising worldwide use of fossil fuels and the severity of energy scarcity issues, the utilization of renewable and ecologically friendly energy resources has become an important global concern. Solar energy is regarded as the ideal alternative source of energy owing to its limitless reserves and clean nature. Numerous techniques, including the discovery of new materials and modifications to the device's mechanics, have been used to create OSCs with greater power conversion efficiencies (PCEs).<sup>141,142</sup>

To boost the PCEs of OSCs, it is also possible to construct cells with tandem and ternary architectures.<sup>143–145</sup> Due to the comparatively limited absorption site (100 nm) of organic materials, single-junction binary OSCs with one donor and one acceptor material capture insufficient photons from their active layers.<sup>146</sup> Thus, multi-junction designs, notably tandem OSCs, have been created to produce solar cells with a greater PCE and a larger absorption spectrum than their single-junction binary counterparts. However, tandem OSCs have complicated device architectures that need sophisticated manufacturing procedures, which may hinder their industrialization potential. OSCs may be constructed using ternary structures in order to build high-performance materials that display both increased photon harvesting of multiple organic materials, as seen in tandem OSCs, and the simplicity of the fabrication conditions utilized to fabricate single-junction BHJ OSCs. In general, the first concern when inserting a third component into OSCs is the increase or complementarity of the active layer's absorption capabilities. Ternary OSCs are extremely straightforward to fabricate because of their single-

junction device layout and lack of numerous stacks. In addition to photon energy harvesting, however, energy levels and nano-morphology should also be addressed when choosing a third component. In addition, the influence of the third component of OSCs might present itself in a variety of qualities. Compared to binary OSCs, the mechanism behind the photovoltaic process in ternary OSCs is drastically different. Adding a third component to a binary mix involves far more than the simple combination of the separate components.

The active layer of the OSCs fabricated in this study consists of two donors and an acceptor. (D1/D2/A) P1, one of the materials used as a donor, is a random conjugated polymer containing benzotriazole, bistriphenylamine and benzodithiophene. This polymer absorbs in the red region of the UV-VIS spectrum ( $\lambda_{\text{max}}$ : 488nm) and a maximum of 3.5% PCE was obtained when binary OSC was fabricated with the PC<sub>71</sub>BM acceptor. As the second donor in this study, the widely known and utilized PTB7-Th was incorporated. PTB7-Th has a small optical band gap ( $E_g$ ) of 1.58 eV despite its extensive absorption (600–800 nm) in the visible spectrum. Moreover, the intermolecular interaction and hole mobility can be significantly enhanced thanks to the incorporation of two conjugated thiophene side chains. With an open-circuit voltage ( $V_{\text{OC}}$ ) of 0.83 volts, the PTB7-Th:PC<sub>71</sub>BM combination that has been used the most frequently was able to achieve a power conversion efficiency (PCE) of 9.21%.<sup>147</sup> As a result, PTB7-Th is widely acknowledged as being among the most traditional donor polymers for the production of OPV. This polymer donor's absorption region and polymer P1's absorption region are complementary. Thanks to these complementary absorption ranges, nearly the entire visible spectrum will absorb when combined. PC<sub>71</sub>BM was used as an acceptor in this study because its HOMO-LUMO energy values are suitable with two polymers.

## 6.2 Experimental

### 6.2.1 Optical Properties

The absorption of light in this layer is crucial for the device's performance. The photoactive layer absorbs light, and the energy from the absorbed light excites electrons to a higher energy level, creating a flow of electrical current known as the  $J_{SC}$ .

When the absorption of light in the photoactive layer increases, it means that more photons are being absorbed by the organic compounds in the layer. This in turn leads to an increase in the number of excited electrons, which results in an increase in the  $J_{SC}$ . This is because  $J_{SC}$  is directly proportional to the number of photons absorbed by the photoactive layer.

In other words, when the absorption of light in the photoactive layer increases, the TBOSC device will have more electrons flowing through it, which means that the  $J_{SC}$  will increase. This is an important factor to consider when designing and optimizing TBOSCs, as increasing the  $J_{SC}$  can help to improve the overall efficiency of the device. Figure 6.1 displays the thin film absorption spectra of P1 and PTB7-Th, which were utilized to determine the compatibility of these two donors in the UV-VIS spectrum.

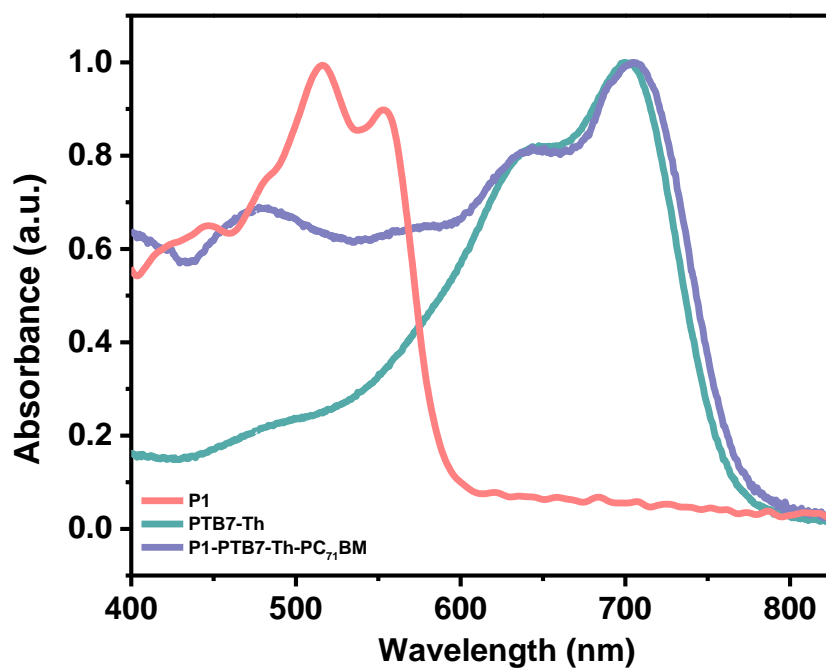


Figure 6.1 UV-VIS spectra of P1, PTB7-Th and P1:PTB7-Th-PC<sub>71</sub>BM

The molecular structures of polymer P1 and PTB7-Th are shown in Figure 6.2.

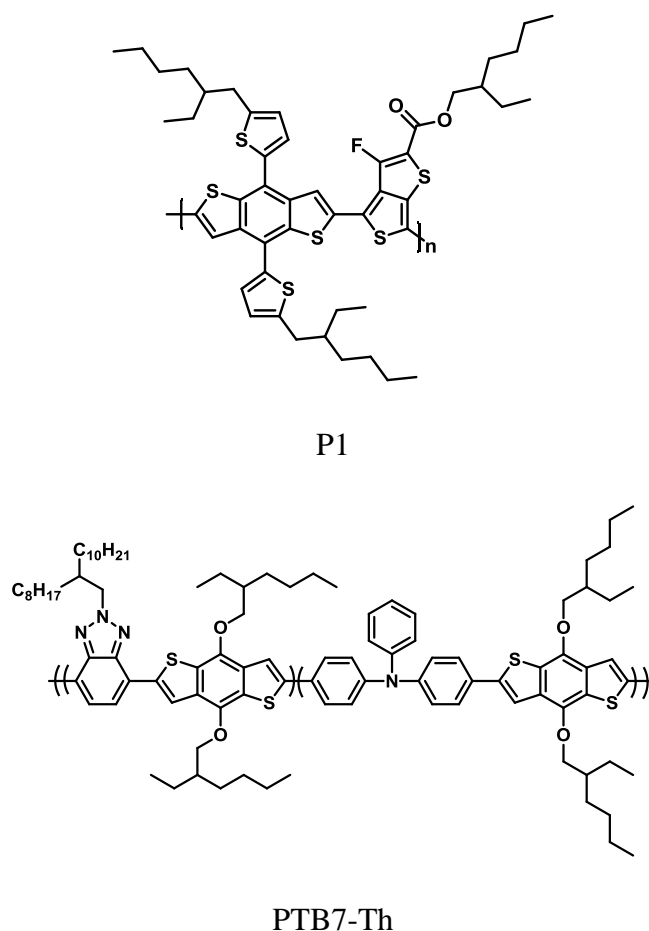


Figure 6.2 Structures of P1 and PTB7-Th

### 6.2.2 Device Fabrication and Characterization

Due to its transparency and low surface resistance, ITO coated glass substrates are utilized in solar cell applications. Ternary Organic Solar Cells (TB-OSCs) were manufactured in a nitrogen-filled glove box system with the ITO/PEDOT:PSS/(D1/D2/A)/LiF/Al configuration. In an ultrasonic bath, ITO-coated glass substrates ( $10\text{-}20 \Omega / \text{cm}^2$ ) were washed with Hellmanex detergent, distilled water, acetone, and isopropyl alcohol. After the ITOs were dried using a nitrogen gun, the surface of the ITOs were treated with oxygen plasma for 5 minutes to eliminate any

organic contaminants. After the oxygen plasma was applied, the PEDOT: PSS was filtered with a 0.45  $\mu\text{m}$  polyether sulfone (PES) filter and spincoated to serve as an intermediary layer in the transfer of positively charged ions to the ITO surface. PEDOT: PSS-coated ITO substrates were annealed at 135  $^{\circ}\text{C}$  for 15 minutes on a hot plate. The active layer containing D1/D2/A was applied to the surface by spin-coating at 2700 rpm. In the last stage, metal connections were fabricated via thermal evaporation under extremely low pressure ( $10^{-7}$  mbar). Device architecture and energy level diagram were given in Figure 6.3

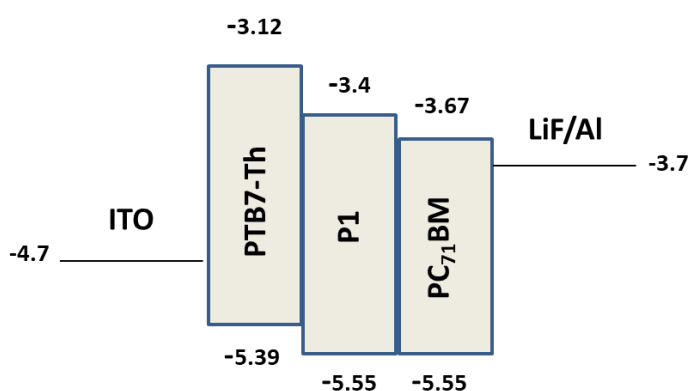


Figure 6.3 Device architecture and energy level diagram of fabricated TB-OSCs

### 6.3 Results and Discussion

The production of TB-OSC includes two donors and an acceptor. Architecture of the device is ITO/PEDOT: PSS/Active layer/LiF/Al. By maintaining a constant ratio of 1:1.5 between PTB7-Th and PC<sub>71</sub>BM, the weight content of polymer P1 was changed from 0% to 20%. The binary inverted OSCs based on PTB7-Th: PC<sub>71</sub>BM have a PCE of 7.12%, a  $J_{\text{SC}}$  of 14.41  $\text{mA}/\text{cm}^2$ , a  $V_{\text{OC}}$  of 0.76 V, and an FF of 65.0%. In Table 6.1, the device parameters are summarized. In comparison to the binary inverted OSCs, the addition of 7% polymer P1 to the ternary blend layers dramatically enhanced the values of the following parameters:  $J_{\text{SC}}$  from 14.41  $\text{mA}/\text{cm}^2$  to 19.80  $\text{mA}/\text{cm}^2$ ,  $V_{\text{OC}}$  from 0.76 V to 0.78 V, and therefore, the PCE from 7.12% to 9.26%. Even while the  $J_{\text{SC}}$  value increased as the number of

photons absorbed increased with a further increase in the P1 content, the FF value declined substantially, which decreased the PCE. Figure 6.4 depicts the current-density–voltage (J–V) curves of the TB-OSCs based on PTB7-Th:PC<sub>71</sub>BM and PTB7-Th:P1:PC<sub>71</sub>BM that exhibit excellent photovoltaic performance.

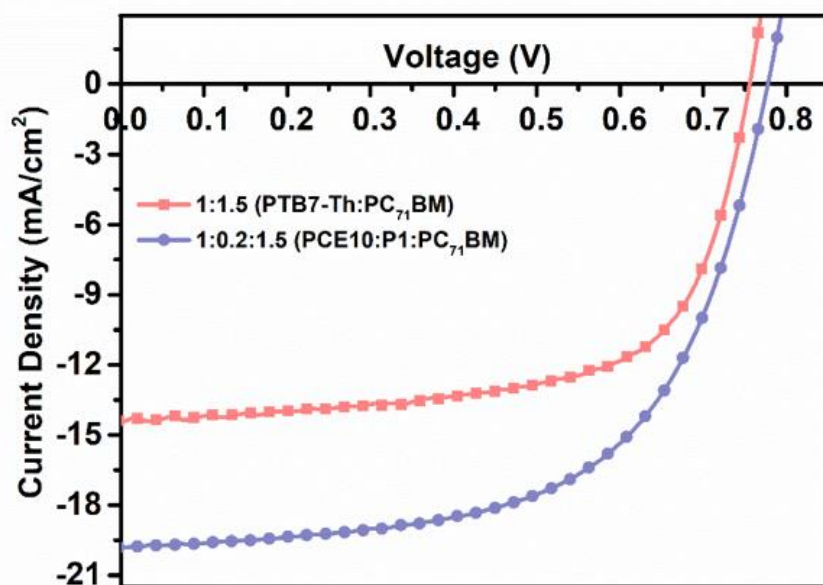


Figure 6.4 J-V curves of PTB7-Th:PC<sub>71</sub>BM and PTB7-Th:P1:PC<sub>71</sub>BM

The doping of second donor P1 is primarily responsible for the increase in EQE in the band. This was done in order to allow the ternary active layer to achieve complementary absorption in the visible light. EQE vs. wavelength graph was shown in Figure 6.5.

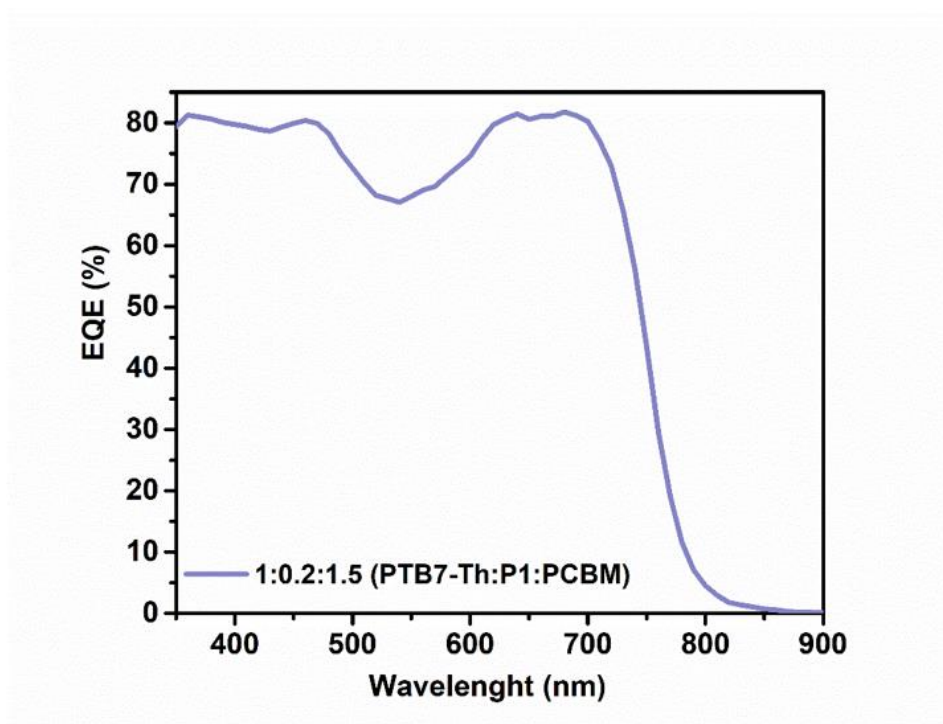


Figure 6.5 EQE graph for the best working device

Table 6.1 Key performance parameters of TB-OSCs comprising PTB7-Th:P1:PC<sub>71</sub>BM

Ratio(PTB7-Th-P1-PCBM70)	PCE	FF (%)	Current Density (mA/cm <sup>2</sup> )	Voc (V)
0:1:2	3.50*	47	9.45	0.79
1:0:1.5	7.12	65	14.41	0.76
1:0.15:1.5	7.29	65	14.44	0.77
1:0.2:1.5	9.26	60	19.80	0.78
1:0.3:1.5	7.14	46	21.33	0.73

Images from TEM and AFM were analyzed for morphology and topography. Figure 6.6 shows 100 nm-scale TEM images of the active layer containing PTB7-Th, P1, and PTB7-Th:P1. The bright regions are regions rich in polymers, while the dark regions are regions rich in PCBM. The film image produced by PTB7-Th, a commercial polymer that is frequently used in literature, is almost perfect. Interpenetrating networks for a homogeneous film are clearly visible in Figure 6.6a. For polymer P1, on the other hand, this cannot be said because aggregated polymers damage the film's homogeneity and may result in reduced charge separation and diffusion. Fortunately, polymer P1 and PTB7-Th could dissolve in



the same solvent and matched well. It can be seen that when compared to PTB7-Th, the morphology did not deteriorate with the TB-OSC film shown in Figure 6.6c. Roughness values are shown below while AFM images are provided in Figure 6.7. The fact that the roughness value does not vary significantly within the TB-OSC structure is further evidence that the donors used are compatible.

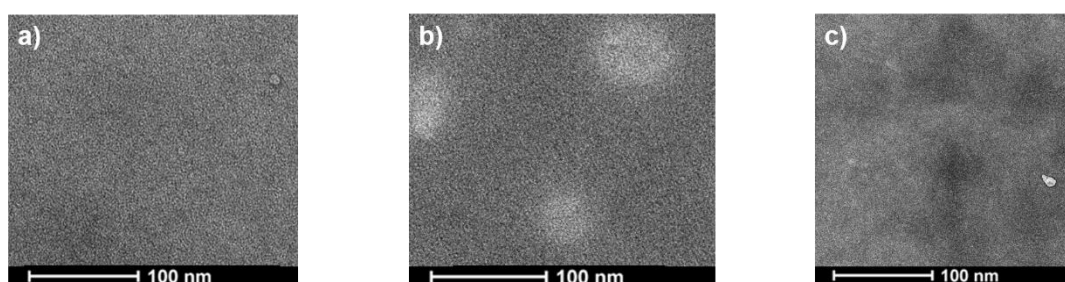


Figure 6.6 TEM images of light-harvesting layers of PTB7-Th, P1 and PTB7-Th:P1

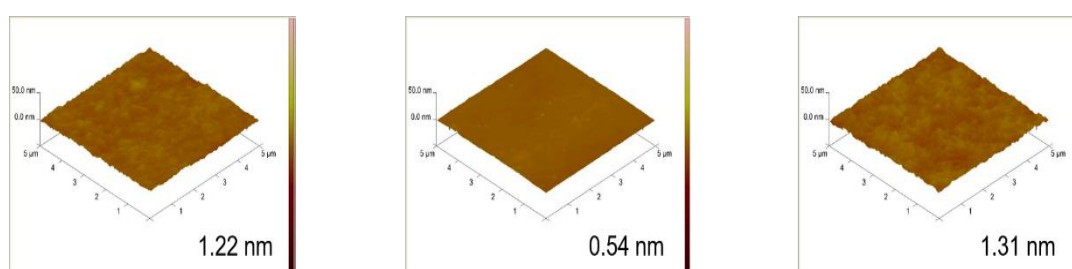


Figure 6.7 AFM images of light-harvesting layers of PTB7-Th, P1 and PTB7-Th:P1

## 6.4 Conclusion

In summary, high-performance D1:D2:A ternary OSCs were developed to improve  $J_{SC}$  by incorporating the polymer donor P1 into a binary blend film consisting of a PTB7-Th and a fullerene acceptor PC<sub>71</sub>BM. The device comprised of a ternary mix with a 1:0.2:1.5 ratio has a PCE of 9.26% and a  $J_{sc}$  of 19.80 mA/cm<sup>2</sup>. Given that the absorption ranges of P1 and PTB7-Th are 350-600 nm and 550-750 nm, respectively, the increase in  $J_{SC}$  is mostly due to the complementing absorption of

two donors. The improvement in the performance parameters has been explained on the basis of the TEM and AFM studies.

## CHAPTER 7

### CONCLUSIONS

Using conjugated polymers or small molecules, optoelectronic devices were designed and fabricated in the three chapters of this thesis. The purpose of these three studies is to build optoelectronic devices with greater efficiency with a rational molecular design.

In the first chapter, electrochemical, optical and photovoltaic properties of three conjugated polymers comprising BDT and TPD and the effect of monofluorination substitution of benzothiadiazole was examined. The effect of substituting the alkoxy group with alkylthienyl on the performance of BHJ OSCs was also discussed. Additionally, morphological and topographical analyses were performed to validate the findings. This chapter is also concerned with the molecular weights of polymers; hence, the GPC analysis has been accomplished. With values of 9.21% PCE, 60.33 FF, and 0.95V  $V_{OC}$ , P-FBDT displayed the highest photovoltaic performance among the synthesized polymers. This study reveals that in addition to polymer structure, molecular weight and morphology are major factors to PCE value.

In the second chapter, three different small molecules (SeDF-G, SeDF-B and SeDF-YG) were designed in the D-A-D structure and selenium was used in the donor unit to examine the spin orbit coupling effect. In this study, optoelectronic, photophysical, theoretical and device properties were examined. A comparison was made with the devices obtained by using phenoxazine instead of phenoselenazine in the donor unit of SeDF-G and SeDF-YG molecules, and it was observed that the spin-orbit coupling effect increased the device performance. Theoretical studies revealed that the difference between singlet and triplet energy levels is sufficient for RISC, that the molecules have dual conformation, and that the equatorial

conformer shows TADF property, while the axial conformer shows classical fluorescence emission. Since TADF approach is very new in terms of literature, synthesizing new molecules with this feature, performing material characterizations, developing device applications and characterizing these molecules have filled an important knowledge gap on this subject. In this study, it was observed that the heavy atom effect increased the device efficiency up to three times.

The third and final chapter covers TBOSCs, two polymer donors (P1 and PTB7-Th) complementary in the UV-VIS spectrum were used in this study. In TBOSC logic, when absorption increases in photoactive layer in device, it will increase in  $J_{SC}$ . TBOSCs require a blend of three different organic compounds, which can be difficult to optimize in terms of their absorption spectra and charge transport properties. The best working device was obtained when suitable solvent and optimum conditions were provided. Thanks to the complementary absorptions of the polymers used, the  $J_{SC}$  value increased (from 14.41 mA/cm<sup>2</sup>) to 19.80 mA/cm<sup>2</sup>), resulting in a higher PCE value (from 7.12% to 9.26%). In order to strengthen and support the findings obtained in this chapter, AFM and TEM analyzes were performed.

## CHAPTER 8

### OUTLOOK

This PhD thesis includes three chapters and the aim of all three studies is to obtain more efficient optoelectronic devices, OSCs and OLEDs. Under this heading, there are directions about how the studies in this thesis can be developed.

-In the first chapter, the results of using random polymers containing BDT and TPD in OSCs are presented. This work was patented by the Turkish Patent Institute. The intramolecular interactions of sulfur and oxygen or hydrogen and oxygen atoms on TPD boost intramolecular charge transfer (ICT) and improve molecular geometry (planarity).<sup>148</sup> Studies of polymers containing TPD with nonfullerene acceptor have been reported recently in the literature.<sup>149</sup> Combining the polymers in this study with non-fullerene acceptors may give promising results. At the same time, performing stability and electron-hole mobility in the first chapter will enrich the study.

-In the second chapter, it was reported that increasing spin orbit coupling increases device efficiency. This work has been published in *Advanced Functional Materials*. Since the TADF OLED concept is a very new topic, there are still very few studies in the literature in this field. The phenoselenazine donor used in this study can also be tested with different acceptors and an outstanding contribution to the literature can be made. As a contribution to this study, different materials in HTL and ETL can be used and their effect on the device can be examined.

-The third chapter of the study explores the use of a photoactive layer that contains two different polymer donors and one acceptor. The goal is to increase the PCE by expanding the absorption region. Stability and hole and/or electron mobility are two important factors that are often investigated in order to further understand the performance of TBOSCs systems. Stability refers to the ability of the TBOSC

device to maintain its performance over time, despite being exposed to environmental factors such as light and heat. Researchers often conduct long-term stability tests to see how well the TBOSC device holds up over time. Hole and/or electron mobility refer to the ability of the TBOSC device to transport electrical charges, specifically holes and electrons. High hole and electron mobility is important for efficient charge collection and thus, high device efficiency. Researchers often use a technique called time-of-flight (TOF) to measure the mobility of holes and electrons in the TBOSC device.

Investigating stability and hole and/or electron mobility in TBOSCs can help researchers to better understand the underlying mechanisms that govern the device's performance. For example, a low stability value may indicate that the device is particularly sensitive to environmental factors, while a low hole or electron mobility value may indicate that the device is not efficiently transporting charges. By understanding these factors, researchers can work to improve the performance of TOSCs and make them more viable for commercial use.

## REFERENCES

1. Cevher SC, Hizalan G, Alemdar Yilmaz E, et al. A comprehensive study: Theoretical and experimental investigation of heteroatom and substituent effects on frontier orbitals and polymer solar cell performances. *J Polym Sci.* 2020;58(19):2792-2806. doi:10.1002/pol.20200513
2. Fukuda K, Yu K, Someya T. The Future of Flexible Organic Solar Cells. *Adv Energy Mater.* 2020;10(25):2000765. doi:10.1002/aenm.202000765
3. Karakurt O, Alemdar E, Erer MC, et al. Boosting the efficiency of organic solar cells via plasmonic gold nanoparticles and thiol functionalized conjugated polymer. *Dye Pigment.* 2022;208:110818. doi:10.1016/j.dyepig.2022.110818
4. Sharif P, Alemdar E, Ozturk S, et al. Rational Molecular Design Enables Efficient Blue TADF–OLEDs with Flexible Graphene Substrate. *Adv Funct Mater.* Published online September 22, 2022:2207324. doi:10.1002/adfm.202207324
5. Salehi A, Fu X, Shin D, So F. Recent Advances in OLED Optical Design. *Adv Funct Mater.* 2019;29(15):1808803. doi:10.1002/adfm.201808803
6. Singh Dhayal S, Nain A, Kumar A, Kumar A. Recent trends in selection of small molecules for OFET applications: A mini review. *Mater Today Proc.* Published online August 2022. doi:10.1016/j.matpr.2022.08.205
7. Pope Martin, Swenberg Charles E. *Electronic Processes in Organic Crystals and Polymers.* Oxford Science Publication; 1999.
8. Coropceanu V, Cornil J, da Silva Filho DA, Olivier Y, Silbey R, Brédas J-L. Charge Transport in Organic Semiconductors. *Chem Rev.* 2007;107(4):926-952. doi:10.1021/cr050140x
9. International Energy Agency (IEA). *World Energy Outlook 2022.*; 2022. <https://www.iea.org/reports/world-energy-outlook-2022>
10. Yang X, Pang J, Teng F, Gong R, Springer C. The environmental co-benefit and economic impact of China's low-carbon pathways: Evidence from linking bottom-up and top-down models. *Renew Sustain Energy Rev.* 2021;136:110438. doi:10.1016/j.rser.2020.110438
11. Taghizadeh-Hesary F, Taghizadeh-Hesary F. The Impacts of Air Pollution on Health and Economy in Southeast Asia. *Energies.* 2020;13(7):1812. doi:10.3390/en13071812
12. Garrett-Peltier H. Green versus brown: Comparing the employment impacts of energy efficiency, renewable energy, and fossil fuels using an input-output model. *Econ Model.* 2017;61:439-447.

doi:10.1016/j.econmod.2016.11.012

13. Sepe A, Rong Z, Sommer M, et al. Structure formation in P3HT/F8TBT blends. *Energy Environ Sci.* 2014;7(5):1725-1736. doi:10.1039/C3EE44125C
14. Szent-Györgyi A. Internal Photo-Electric Effect and Band Spectra in Proteins. *Nature.* 1946;157(4000):875-875. doi:10.1038/157875b0
15. Eley DD. Phthalocyanines as Semiconductors. *Nature.* 1948;162(4125):819-819. doi:10.1038/162819a0
16. Carswell DJ, Ferguson J, Lyons LE. Photo- and Semi-conductance in Molecular Single Crystals. *Nature.* 1954;173(4407):736-736. doi:10.1038/173736a0
17. Chiang CK, Fincher CR, Park YW, et al. Electrical Conductivity in Doped Polyacetylene. *Phys Rev Lett.* 1977;39(17):1098-1101. doi:10.1103/PhysRevLett.39.1098
18. Lin Y, Li Y, Zhan X. Small molecule semiconductors for high-efficiency organic photovoltaics. *Chem Soc Rev.* 2012;41(11):4245. doi:10.1039/c2cs15313k
19. Lin Y, Zhan X. Oligomer Molecules for Efficient Organic Photovoltaics. *Acc Chem Res.* 2016;49(2):175-183. doi:10.1021/acs.accounts.5b00363
20. Palomares E, Billon L, Viterisi A. Crystallinity and Molecular Packing of Small Molecules in Bulk-Heterojunction Organic Solar Cells. *Appl Sci.* 2022;12(11):5683. doi:10.3390/app12115683
21. Sharif P, Alemdar E, Ozturk S, et al. Rational Molecular Design Enables Efficient Blue TADF–OLEDs with Flexible Graphene Substrate. *Adv Funct Mater.* 2022;32(47):2207324. doi:10.1002/adfm.202207324
22. Ajayan J, Nirmal D, Mohankumar P, Saravanan M, Jagadesh M, Arivazhagan L. A review of photovoltaic performance of organic/inorganic solar cells for future renewable and sustainable energy technologies. *Superlattices Microstruct.* 2020;143:106549. doi:10.1016/j.spmi.2020.106549
23. Zhang M, Zhu L, Zhou G, et al. Single-layered organic photovoltaics with double cascading charge transport pathways: 18% efficiencies. *Nat Commun.* 2021;12(1):309. doi:10.1038/s41467-020-20580-8
24. Sariciftci NS, Smilowitz L, Heeger AJ, Wudl F. Photoinduced Electron Transfer from a Conducting Polymer to Buckminsterfullerene. *Science (80-).* 1992;258(5087):1474-1476. doi:10.1126/science.258.5087.1474
25. Yu G, Gao J, Hummelen JC, Wudl F, Heeger AJ. Polymer Photovoltaic Cells: Enhanced Efficiencies via a Network of Internal Donor-Acceptor Heterojunctions. *Science (80-).* 1995;270(5243):1789-1791.



doi:10.1126/science.270.5243.1789

26. Zhang F, Zhuo Z, Zhang J, et al. Influence of PC60BM or PC70BM as electron acceptor on the performance of polymer solar cells. *Sol Energy Mater Sol Cells*. 2012;97:71-77. doi:10.1016/j.solmat.2011.09.006
27. Tang CW. Two-layer organic photovoltaic cell. *Appl Phys Lett*. 1986;48(2):183-185. doi:10.1063/1.96937
28. Shaheen, S. and DG. *Photovoltaics: Organic-Based Solar Cells.*; 2009.
29. Zhang Y, Kan B, Sun Y, et al. Nonfullerene Tandem Organic Solar Cells with High Performance of 14.11%. *Adv Mater*. 2018;30(18):1707508. doi:10.1002/adma.201707508
30. Liu G, Xia R, Huang Q, et al. Tandem Organic Solar Cells with 18.7% Efficiency Enabled by Suppressing the Charge Recombination in Front Sub-Cell. *Adv Funct Mater*. 2021;31(29):2103283. doi:10.1002/adfm.202103283
31. Meng L, Zhang Y, Wan X, et al. Organic and solution-processed tandem solar cells with 17.3% efficiency. *Science (80- )*. 2018;361(6407):1094-1098. doi:10.1126/science.aat2612
32. Wang J, Zheng Z, Zu Y, et al. A Tandem Organic Photovoltaic Cell with 19.6% Efficiency Enabled by Light Distribution Control. *Adv Mater*. 2021;33(39):2102787. doi:10.1002/adma.202102787
33. Ma Q, Jia Z, Meng L, et al. Promoting charge separation resulting in ternary organic solar cells efficiency over 17.5%. *Nano Energy*. 2020;78:105272. doi:10.1016/j.nanoen.2020.105272
34. Zeng Y, Li D, Xiao Z, et al. Exploring the Charge Dynamics and Energy Loss in Ternary Organic Solar Cells with a Fill Factor Exceeding 80%. *Adv Energy Mater*. 2021;11(31):2101338. doi:10.1002/aenm.202101338
35. Wadsworth A, Moser M, Marks A, et al. Critical review of the molecular design progress in non-fullerene electron acceptors towards commercially viable organic solar cells. *Chem Soc Rev*. 2019;48(6):1596-1625. doi:10.1039/C7CS00892A
36. Jung S, Cho Y, Kang S-H, Yoon S-J, Yang C. Effect of Third Component on Efficiency and Stability in Ternary Organic Solar Cells: More than a Simple Superposition. *Sol RRL*. 2022;6(2):2100819. doi:10.1002/solr.202100819
37. Bi P, Zhang S, Chen Z, et al. Reduced non-radiative charge recombination enables organic photovoltaic cell approaching 19% efficiency. *Joule*. 2021;5(9):2408-2419. doi:10.1016/j.joule.2021.06.020
38. Doumon NY, Yang L, Rosei F. Ternary organic solar cells: A review of the role of the third element. *Nano Energy*. 2022;94:106915. doi:10.1016/j.nanoen.2021.106915

39. Yeh N, Yeh P. Organic solar cells: Their developments and potentials. *Renew Sustain Energy Rev.* 2013;21:421-431. doi:10.1016/j.rser.2012.12.046
40. Cheng Y-J, Yang S-H, Hsu C-S. Synthesis of Conjugated Polymers for Organic Solar Cell Applications. *Chem Rev.* 2009;109(11):5868-5923. doi:10.1021/cr900182s
41. Liang Y, Yu L. Development of Semiconducting Polymers for Solar Energy Harvesting. *Polym Rev.* 2010;50(4):454-473. doi:10.1080/15583724.2010.515765
42. Scharber MC, Mühlbacher D, Koppe M, et al. Design Rules for Donors in Bulk-Heterojunction Solar Cells—Towards 10 % Energy-Conversion Efficiency. *Adv Mater.* 2006;18(6):789-794. doi:10.1002/adma.200501717
43. Tanaka H, Shizu K, Miyazaki H, Adachi C. Efficient green thermally activated delayed fluorescence (TADF) from a phenoxazine–triphenyltriazine (PXZ–TRZ) derivative. *Chem Commun.* 2012;48(93):11392. doi:10.1039/c2cc36237f
44. Nakanotani H, Masui K, Nishide J, Shibata T, Adachi C. Promising operational stability of high-efficiency organic light-emitting diodes based on thermally activated delayed fluorescence. *Sci Rep.* 2013;3(1):2127. doi:10.1038/srep02127
45. Endo A, Sato K, Yoshimura K, et al. Efficient up-conversion of triplet excitons into a singlet state and its application for organic light emitting diodes. *Appl Phys Lett.* 2011;98(8):083302. doi:10.1063/1.3558906
46. Lee J, Shizu K, Tanaka H, Nomura H, Yasuda T, Adachi C. Oxadiazole- and triazole-based highly-efficient thermally activated delayed fluorescence emitters for organic light-emitting diodes. *J Mater Chem C.* 2013;1(30):4599. doi:10.1039/c3tc30699b
47. Li J, Nakagawa T, MacDonald J, et al. Highly Efficient Organic Light-Emitting Diode Based on a Hidden Thermally Activated Delayed Fluorescence Channel in a Heptazine Derivative. In: *Renewable Energy and the Environment*. OSA; 2013:DM1E.3. doi:10.1364/SOLED.2013.DM1E.3
48. Takahashi T, Shizu K, Yasuda T, Togashi K, Adachi C. Donor–acceptor-structured 1,4-diazatriphenylene derivatives exhibiting thermally activated delayed fluorescence: design and synthesis, photophysical properties and OLED characteristics. *Sci Technol Adv Mater.* 2014;15(3):034202. doi:10.1088/1468-6996/15/3/034202
49. Zhang Q, Li J, Shizu K, et al. Design of Efficient Thermally Activated Delayed Fluorescence Materials for Pure Blue Organic Light Emitting Diodes. *J Am Chem Soc.* 2012;134(36):14706-14709. doi:10.1021/ja306538w

50. Zhang D, Duan L, Li C, et al. High-Efficiency Fluorescent Organic Light-Emitting Devices Using Sensitizing Hosts with a Small Singlet-Triplet Exchange Energy. *Adv Mater.* 2014;26(29):5050-5055. doi:10.1002/adma.201401476
51. Yang Z, Mao Z, Xie Z, et al. Recent advances in organic thermally activated delayed fluorescence materials. *Chem Soc Rev.* 2017;46(3):915-1016. doi:10.1039/C6CS00368K
52. Murawski C, Leo K, Gather MC. Efficiency Roll-Off in Organic Light-Emitting Diodes. *Adv Mater.* 2013;25(47):6801-6827. doi:10.1002/adma.201301603
53. Reineke S, Walzer K, Leo K. Triplet-exciton quenching in organic phosphorescent light-emitting diodes with Ir-based emitters. *Phys Rev B.* 2007;75(12):125328. doi:10.1103/PhysRevB.75.125328
54. Wang Y, Yun JH, Wang L, Lee JY. High Triplet Energy Hosts for Blue Organic Light-Emitting Diodes. *Adv Funct Mater.* 2021;31(12):2008332. doi:10.1002/adfm.202008332
55. Kaji H, Suzuki H, Fukushima T, et al. Purely organic electroluminescent material realizing 100% conversion from electricity to light. *Nat Commun.* 2015;6(1):8476. doi:10.1038/ncomms9476
56. Pope M, Kallmann HP, Magnante P. Electroluminescence in Organic Crystals. *J Chem Phys.* 1963;38(8):2042-2043. doi:10.1063/1.1733929
57. Yersin H, Rausch AF, Czerwieńiec R, Hofbeck T, Fischer T. The triplet state of organo-transition metal compounds. Triplet harvesting and singlet harvesting for efficient OLEDs. *Coord Chem Rev.* 2011;255(21-22):2622-2652. doi:10.1016/j.ccr.2011.01.042
58. Chaskar A, Chen H-F, Wong K-T. Bipolar Host Materials: A Chemical Approach for Highly Efficient Electrophosphorescent Devices. *Adv Mater.* 2011;23(34):3876-3895. doi:10.1002/adma.201101848
59. Masui K, Nakanotani H, Adachi C. Analysis of exciton annihilation in high-efficiency sky-blue organic light-emitting diodes with thermally activated delayed fluorescence. *Org Electron.* 2013;14(11):2721-2726. doi:10.1016/j.orgel.2013.07.010
60. Tagare J, Vaidyanathan S. Recent development of phenanthroimidazole-based fluorophores for blue organic light-emitting diodes (OLEDs): an overview. *J Mater Chem C.* 2018;6(38):10138-10173. doi:10.1039/C8TC03689F
61. Jankus V, Data P, Graves D, et al. Highly Efficient TADF OLEDs: How the Emitter-Host Interaction Controls Both the Excited State Species and Electrical Properties of the Devices to Achieve Near 100% Triplet Harvesting and High Efficiency. *Adv Funct Mater.* 2014;24(39):6178-6186.

doi:10.1002/adfm.201400948

62. Holmes RJ, Forrest SR, Tung Y-J, et al. Blue organic electrophosphorescence using exothermic host-guest energy transfer. *Appl Phys Lett*. 2003;82(15):2422-2424. doi:10.1063/1.1568146
63. Duan L, Qiao J, Sun Y, Qiu Y. Strategies to Design Bipolar Small Molecules for OLEDs: Donor-Acceptor Structure and Non-Donor-Acceptor Structure. *Adv Mater*. 2011;23(9):1137-1144. doi:10.1002/adma.201003816
64. Zhang M, Zhu L, Zhou G, et al. Single-layered organic photovoltaics with double cascading charge transport pathways: 18% efficiencies. *Nat Commun*. 2021;12(1):1-10. doi:10.1038/s41467-020-20580-8
65. Zhou Y, Kurosawa T, Ma W, et al. High Performance All-Polymer Solar Cell via Polymer Side-Chain Engineering. *Adv Mater*. 2014;26(22):3767-3772. doi:10.1002/adma.201306242
66. Wang Y, Liu Y, Chen S, Peng R, Ge Z. Significant Enhancement of Polymer Solar Cell Performance via Side-Chain Engineering and Simple Solvent Treatment. *Chem Mater*. 2013;25(15):3196-3204. doi:10.1021/cm401618h
67. Zhang Q, Kelly MA, Bauer N, You W. The Curious Case of Fluorination of Conjugated Polymers for Solar Cells. *Acc Chem Res*. 2017;50(9):2401-2409. doi:10.1021/acs.accounts.7b00326
68. Yasa M, Depci T, Alemdar E, Hacıoglu SO, Cirpan A, Toppare L. Non-fullerene organic photovoltaics based on thienopyrroledione comprising random copolymers; effect of alkyl chains. *Renew Energy*. 2021;178:202-211. doi:10.1016/j.renene.2021.06.087
69. Zhao F, Wang C, Zhan X. Morphology Control in Organic Solar Cells. *Adv Energy Mater*. 2018;8(28):1703147. doi:10.1002/aenm.201703147
70. Xie Y, Yang F, Li Y, et al. Morphology Control Enables Efficient Ternary Organic Solar Cells. *Adv Mater*. 2018;30(38):1803045. doi:10.1002/adma.201803045
71. Liao H-C, Ho C-C, Chang C-Y, Jao M-H, Darling SB, Su W-F. Additives for morphology control in high-efficiency organic solar cells. *Mater Today*. 2013;16(9):326-336. doi:10.1016/j.mattod.2013.08.013
72. Zhao DW, Tan ST, Ke L, et al. Optimization of an inverted organic solar cell. *Sol Energy Mater Sol Cells*. 2010;94(6):985-991. doi:10.1016/j.solmat.2010.02.010
73. Vincent P, Shin S-C, Goo JS, et al. Indoor-type photovoltaics with organic solar cells through optimal design. *Dye Pigment*. 2018;159:306-313. doi:10.1016/j.dyepig.2018.06.025
74. Zhu L, Zhang M, Zhou G, et al. Efficient Organic Solar Cell with 16.88%

- Efficiency Enabled by Refined Acceptor Crystallization and Morphology with Improved Charge Transfer and Transport Properties. *Adv Energy Mater.* 2020;10(18):1904234. doi:10.1002/aenm.201904234
75. Azzouzi M, Kirchartz T, Nelson J. Factors Controlling Open-Circuit Voltage Losses in Organic Solar Cells. *Trends Chem.* 2019;1(1):49-62. doi:10.1016/j.trechm.2019.01.010
  76. Elumalai NK, Uddin A. Open circuit voltage of organic solar cells: An in-depth review. *Energy Environ Sci.* 2016;9(2):391-410. doi:10.1039/c5ee02871j
  77. Qi B, Wang J. Fill factor in organic solar cells. *Phys Chem Chem Phys.* 2013;15(23):8972-8982. doi:10.1039/c3cp51383a
  78. Qiu D, Adil MA, Lu K, Wei Z. The Crystallinity Control of Polymer Donor Materials for High-Performance Organic Solar Cells. *Front Chem.* 2020;8(November):1-21. doi:10.3389/fchem.2020.603134
  79. Zou Y, Najari A, Berrouard P, et al. A Thieno[3,4- c ]pyrrole-4,6-dione-Based Copolymer for Efficient Solar Cells. *J Am Chem Soc.* 2010;132(15):5330-5331. doi:10.1021/ja101888b
  80. Bang S, Park J, Kang S, et al. Dyes and Pigments Thienopyrroledione and benzodithiophene / thiophene-based random terpolymer for polymer solar cells with improved fill factor. *Dye Pigment.* 2017;140:229-235. doi:10.1016/j.dyepig.2017.01.049
  81. Cevher SC, Hizalan G, Alemdar Yilmaz E, et al. A comprehensive study: Theoretical and experimental investigation of heteroatom and substituent effects on frontier orbitals and polymer solar cell performances. *J Polym Sci.* 2020;58(19):2792-2806. doi:10.1002/pol.20200513
  82. Liang Y, Feng D, Wu Y, et al. Highly Efficient Solar Cell Polymers Developed via Fine-Tuning of Structural and Electronic Properties. *J Am Chem Soc.* 2009;131(22):7792-7799. doi:10.1021/ja901545q
  83. Huo L, Zhang S, Guo X, Xu F, Li Y, Hou J. Replacing Alkoxy Groups with Alkylthienyl Groups: A Feasible Approach To Improve the Properties of Photovoltaic Polymers. *Angew Chemie Int Ed.* 2011;50(41):9697-9702. doi:10.1002/anie.201103313
  84. Liu P, Zhang K, Liu F, et al. Effect of Fluorine Content in Thienothiophene-Benzodithiophene Copolymers on the Morphology and Performance of Polymer Solar Cells. *Chem Mater.* 2014;26(9):3009-3017. doi:10.1021/cm500953e
  85. Warnan J, El Labban A, Cabanetos C, et al. Ring Substituents Mediate the Morphology of PBDTPD-PCBM Bulk-Heterojunction Solar Cells. *Chem Mater.* 2014;26(7):2299-2306. doi:10.1021/cm500172w

86. Liao S-H, Jhuo H-J, Cheng Y-S, Chen S-A. Fullerene Derivative-Doped Zinc Oxide Nanofilm as the Cathode of Inverted Polymer Solar Cells with Low-Bandgap Polymer (PTB7-Th) for High Performance. *Adv Mater.* 2013;25(34):4766-4771. doi:10.1002/adma.201301476
87. Dou L, Gao J, Richard E, et al. Systematic Investigation of Benzodithiophene- and Diketopyrrolopyrrole-Based Low-Bandgap Polymers Designed for Single Junction and Tandem Polymer Solar Cells. *J Am Chem Soc.* 2012;134(24):10071-10079. doi:10.1021/ja301460s
88. Keles D, Erer MC, Bolayir E, et al. Conjugated polymers with benzothiadiazole and benzotriazole moieties for polymer solar cells. *Renew Energy.* 2019;139:1184-1193. doi:10.1016/j.renene.2019.03.018
89. Cevher SC, Unlu NA, Ozelcaglayan AC, et al. Fused structures in the polymer backbone to investigate the photovoltaic and electrochromic properties of donor-acceptor-type conjugated polymers. *J Polym Sci Part A Polym Chem.* 2013;51(9):1933-1941. doi:10.1002/pola.26553
90. Taskaya S, Cevher D, Bolayir E, et al. Electrochimica Acta Synthesis of selenophene substituted benzodithiophene and fluorinate d b enzothiadiazole base d conjugate d polymers for organic solar cell applications. *Electrochim Acta.* 2021;398:139298. doi:10.1016/j.electacta.2021.139298
91. Fei Z, Shahid M, Yaacobi-Gross N, et al. Thiophene fluorination to enhance photovoltaic performance in low band gap donor–acceptor polymers. *Chem Commun.* 2012;48(90):11130-11132. doi:10.1039/c2cc35079c
92. Putri SK, Kim YH, Whang DR, Lee MS, Kim JH, Chang DW. Step-by-step improvement in photovoltaic properties of fluorinated quinoxaline-based low-band-gap polymers. *Org Electron.* 2017;47:14-23. doi:10.1016/j.orgel.2017.04.025
93. Liu D, Zhao W, Zhang S, et al. Highly Efficient Photovoltaic Polymers Based on Benzodithiophene and Quinoxaline with Deeper HOMO Levels. *Macromolecules.* 2015;48(15):5172-5178. doi:10.1021/acs.macromol.5b00829
94. Shockley W, Queisser HJ. Detailed Balance Limit of Efficiency of p-n Junction Solar Cells. *J Appl Phys.* 1961;32(3):510-519. doi:10.1063/1.1736034
95. Rühle S. Tabulated values of the Shockley–Queisser limit for single junction solar cells. *Sol Energy.* 2016;130:139-147. doi:10.1016/j.solener.2016.02.015
96. Classen A, Einsiedler L, Heumueller T, et al. Absence of Charge Transfer State Enables Very Low VOC Losses in SWCNT:Fullerene Solar Cells. *Adv Energy Mater.* 2019;9(1):1-9. doi:10.1002/aenm.201801913
97. Gao M, Wang W, Hou J, Ye L. Control of aggregated structure of

- photovoltaic polymers for high-efficiency solar cells. *Aggregate*. 2021;2(5). doi:10.1002/agt2.46
98. Lou SJ, Szarko JM, Xu T, Yu L, Marks TJ, Chen LX. Effects of additives on the morphology of solution phase aggregates formed by active layer components of high-efficiency organic solar cells. *J Am Chem Soc*. 2011;133(51):20661-20663. doi:10.1021/ja2085564
  99. Yuan J, Zhai Z, Dong H, et al. Efficient Polymer Solar Cells with a High Open Circuit Voltage of 1 Volt. *Adv Funct Mater*. 2013;23(7):885-892. doi:10.1002/adfm.201201535
  100. Lee TH, Park SY, Walker B, et al. A universal processing additive for high-performance polymer solar cells. *RSC Adv*. 2017;7(13):7476-7482. doi:10.1039/c6ra27944a
  101. Riedel I, Parisi J, Dyakonov V, Lutsen L, Vanderzande D, Hummelen JC. Effect of Temperature and Illumination on the Electrical Characteristics of Polymer–Fullerene Bulk-Heterojunction Solar Cells. *Adv Funct Mater*. 2004;14(1):38-44. doi:10.1002/adfm.200304399
  102. Cowan SR, Roy A, Heeger AJ. Recombination in polymer-fullerene bulk heterojunction solar cells. *Phys Rev B*. 2010;82(24):245207. doi:10.1103/PhysRevB.82.245207
  103. Koster LJA, Mihailetchi VD, Ramaker R, Blom PWM. Light intensity dependence of open-circuit voltage of polymer:fullerene solar cells. *Appl Phys Lett*. 2005;86(12):123509. doi:10.1063/1.1889240
  104. Yang C, Zhang J, Liang N, et al. Effects of energy-level offset between a donor and acceptor on the photovoltaic performance of non-fullerene organic solar cells. *J Mater Chem A*. 2019;7(32):18889-18897. doi:10.1039/C9TA04789A
  105. Ziffer ME, Jo SB, Zhong H, et al. Long-Lived, Non-Geminate, Radiative Recombination of Photogenerated Charges in a Polymer/Small-Molecule Acceptor Photovoltaic Blend. *J Am Chem Soc*. 2018;140(31):9996-10008. doi:10.1021/jacs.8b05834
  106. Kumar P, Kannappan S, Ochiai S, Shin P-K. High-performance organic solar cells based on a low-bandgap poly-thienothiophene-benzodithiophene polymer and fullerene composite prepared by using the airbrush spray-coating technique. *J Korean Phys Soc*. 2013;62(8):1169-1175. doi:10.3938/jkps.62.1169
  107. Kumar P, Santhakumar K, Tatsugi J, Shin P-K, Ochiai S. Comparison of properties of polymer organic solar cells prepared using highly conductive modified PEDOT:PSS films by spin- and spray-coating methods. *Jpn J Appl Phys*. 2014;53(1S):01AB08. doi:10.7567/JJAP.53.01AB08
  108. Zheng Y, Wu R, Shi W, Guan Z, Yu J. Effect of in situ annealing on the

- performance of spray coated polymer solar cells. *Sol Energy Mater Sol Cells*. 2013;111:200-205. doi:10.1016/j.solmat.2013.01.011
109. Friend RH, Gymer RW, Holmes AB, et al. Electroluminescence in conjugated polymers. *Nature*. 1999;397(6715):121-128. doi:10.1038/16393
  110. Adachi C, Baldo MA, Thompson ME, Forrest SR. Nearly 100% internal phosphorescence efficiency in an organic light-emitting device. *J Appl Phys*. 2001;90(10):5048-5051. doi:10.1063/1.1409582
  111. Wallikewitz BH, Kabra D, Gélinas S, Friend RH. Triplet dynamics in fluorescent polymer light-emitting diodes. *Phys Rev B - Condens Matter Mater Phys*. 2012;85(4):22-25. doi:10.1103/PhysRevB.85.045209
  112. Zhu J, Han D, Wu X, Ting J, Du S, Arias AC. Highly Flexible Transparent Micromesh Electrodes via Blade-Coated Polymer Networks for Organic Light-Emitting Diodes. *ACS Appl Mater Interfaces*. 2020;12(28):31687-31695. doi:10.1021/acsami.0c07299
  113. Keum C, Murawski C, Archer E, Kwon S, Mischok A, Gather MC. A substrateless, flexible, and water-resistant organic light-emitting diode. *Nat Commun*. 2020;11(1):6250. doi:10.1038/s41467-020-20016-3
  114. Rodriguez-Serrano A, Rai-Constapel V, Daza MC, Doerr M, Marian CM. Internal heavy atom effects in phenothiazinium dyes: Enhancement of intersystem crossing via vibronic spin-orbit coupling. *Phys Chem Chem Phys*. 2015;17(17):11350-11358. doi:10.1039/c5cp00194c
  115. Kondakov DY, Sandifer JR, Tang CW, Young RH. Nonradiative recombination centers and electrical aging of organic light-emitting diodes: Direct connection between accumulation of trapped charge and luminance loss. *J Appl Phys*. 2003;93(2):1108-1119. doi:10.1063/1.1531231
  116. Lee SY, Yasuda T, Yang YS, Zhang Q, Adachi C. Luminous butterflies: Efficient exciton harvesting by benzophenone derivatives for full-color delayed fluorescence OLEDs. *Angew Chemie - Int Ed*. 2014;53(25):6402-6406. doi:10.1002/anie.201402992
  117. Hoover GC, Seferos DS. Photoactivity and optical applications of organic materials containing selenium and tellurium. *Chem Sci*. 2019;10(40):9182-9188. doi:10.1039/C9SC04279B
  118. Kim CL, Jeong J, Lee DR, et al. Dual Mode Radiative Transition from a Phenoselenazine Derivative and Electrical Switching of the Emission Mechanism. *J Phys Chem Lett*. 2020;11(14):5591-5600. doi:10.1021/acs.jpcclett.0c01580
  119. Hu YX, Miao J, Hua T, Huang Z, Qi Y, Zou Y. Selenium-integrated multi-resonance induced TADF emitters boost EQE of electroluminescence to 40 . 5 % with ultra-low efficiency roll-off. *Nat Portf*. Published online 2022:1-12.



120. de Sa Pereira D, Lee DR, Kukhta NA, et al. The effect of a heavy atom on the radiative pathways of an emitter with dual conformation, thermally-activated delayed fluorescence and room temperature phosphorescence. *J Mater Chem C*. 2019;7(34):10481-10490. doi:10.1039/C9TC02477H
121. Aksoy E, Danos A, Li C, Monkman AP, Varlikli C. Silylethynyl Substitution for Preventing Aggregate Formation in Perylene Diimides. *J Phys Chem C*. 2021;125(23):13041-13049. doi:10.1021/acs.jpcc.1c03131
122. Haase N, Danos A, Pflumm C, et al. Kinetic Modeling of Transient Photoluminescence from Thermally Activated Delayed Fluorescence. *J Phys Chem C*. 2018;122(51):29173-29179. doi:10.1021/acs.jpcc.8b11020
123. Hempe M, Kukhta NA, Danos A, et al. Vibrational Damping Reveals Vibronic Coupling in Thermally Activated Delayed Fluorescence Materials. *Chem Mater*. 2021;33(9):3066-3080. doi:10.1021/acs.chemmater.0c03783
124. Sem S, Jenatsch S, Stavrou K, Danos A, Monkman AP, Ruhstaller B. Determining non-radiative decay rates in TADF compounds using coupled transient and steady state optical data. *J Mater Chem C*. 2022;10(12):4878-4885. doi:10.1039/D1TC05594A
125. Marghad I, Kim DH, Tian X, et al. Synthesis by a Cost-Effective Method and Electroluminescence of a Novel Efficient Yellowish-Green Thermally Activated Delayed Fluorescent Molecule. *ACS Omega*. 2018;3(2):2254-2260. doi:10.1021/acsomega.7b01570
126. Xiang S, Guo R, Huang Z, et al. Highly efficient yellow nondoped thermally activated delayed fluorescence OLEDs by utilizing energy transfer between dual conformations based on phenothiazine derivatives. *Dye Pigment*. 2019;170:107636. doi:10.1016/j.dyepig.2019.107636
127. Tanaka H, Shizu K, Nakanotani H, Adachi C. Dual Intramolecular Charge-Transfer Fluorescence Derived from a Phenothiazine-Triphenyltriazine Derivative. *J Phys Chem C*. 2014;118(29):15985-15994. doi:10.1021/jp501017f
128. Wang K, Shi Y-Z, Zheng C-J, et al. Control of Dual Conformations: Developing Thermally Activated Delayed Fluorescence Emitters for Highly Efficient Single-Emitter White Organic Light-Emitting Diodes. *ACS Appl Mater Interfaces*. 2018;10(37):31515-31525. doi:10.1021/acsami.8b08083
129. Okazaki M, Takeda Y, Data P, et al. Thermally activated delayed fluorescent phenothiazine-dibenzo[a,j]phenazine-phenothiazine triads exhibiting tricolor-changing mechanochromic luminescence. *Chem Sci*. 2017;8(4):2677-2686. doi:10.1039/C6SC04863C
130. Lee DR, Lee KH, Shao W, Kim CL, Kim J, Lee JY. Heavy Atom Effect of Selenium for Metal-Free Phosphorescent Light-Emitting Diodes. *Chem Mater*. 2020;32(6):2583-2592. doi:10.1021/acs.chemmater.0c00078

131. Kukhta NA, Bryce MR. Dual emission in purely organic materials for optoelectronic applications. *Mater Horizons*. 2021;8(1):33-55. doi:10.1039/D0MH01316A
132. Furukawa T, Nakanotani H, Inoue M, Adachi C. electroluminescence efficiency and. Published online 2015:1-8. doi:10.1038/srep08429
133. Zhang Y, Forrest SR. Triplets contribute to both an increase and loss in fluorescent yield in organic light emitting diodes. *Phys Rev Lett*. 2012;108(26):1-5. doi:10.1103/PhysRevLett.108.267404
134. Kim Y-H, Wolf C, Cho H, Jeong S-H, Lee T-W. Highly Efficient, Simplified, Solution-Processed Thermally Activated Delayed-Fluorescence Organic Light-Emitting Diodes. *Adv Mater*. 2016;28(4):734-741. doi:10.1002/adma.201504490
135. 10. Advanced Optical Materials - 2021 - Chen - Highly Efficient and Solution-Processed Single-Emissive-Layer Hybrid White.pdf.
136. Angewandte Chemie - 2022 - Tang - Highly Robust CuI-TADF Emitters for Vacuum-Deposited OLEDs with Luminance up to 222 200.pdf.
137. Cui L-S, Gillett AJ, Zhang S-F, et al. Fast spin-flip enables efficient and stable organic electroluminescence from charge-transfer states. *Nat Photonics*. 2020;14(10):636-642. doi:10.1038/s41566-020-0668-z
138. Shi H, Jing W, Liu W, et al. Key Factors Governing the External Quantum Efficiency of Thermally Activated Delayed Fluorescence Organic Light-Emitting Devices: Evidence from Machine Learning. *ACS Omega*. 2022;7(9):7893-7900. doi:10.1021/acsomega.1c06820
139. Nobuyasu RS, Ward JS, Gibson J, et al. The influence of molecular geometry on the efficiency of thermally activated delayed fluorescence. *J Mater Chem C*. 2019;7(22):6672-6684. doi:10.1039/c9tc00720b
140. Etherington MK, Franchello F, Gibson J, et al. Regio and conformational isomerization critical to design of efficient thermally-activated delayed fluorescence emitters. *Nat Commun*. 2017;8:1-11. doi:10.1038/ncomms14987
141. Zhan L, Li S, Xia X, et al. Layer-by-Layer Processed Ternary Organic Photovoltaics with Efficiency over 18%. *Adv Mater*. 2021;33(12):2007231. doi:10.1002/adma.202007231
142. Hong L, Yao H, Wu Z, et al. Eco-Compatible Solvent-Processed Organic Photovoltaic Cells with Over 16% Efficiency. *Adv Mater*. 2019;31(39):1903441. doi:10.1002/adma.201903441
143. Zhang K, Ying L, Yip H-L, Huang F, Cao Y. Toward Efficient Tandem Organic Solar Cells: From Materials to Device Engineering. *ACS Appl Mater Interfaces*. 2020;12(36):39937-39947. doi:10.1021/acsami.0c09909

144. Jia Z, Qin S, Meng L, et al. High performance tandem organic solar cells via a strongly infrared-absorbing narrow bandgap acceptor. *Nat Commun.* 2021;12(1):178. doi:10.1038/s41467-020-20431-6
145. Liang Z, Tong J, Li H, et al. The comprehensive utilization of the synergistic effect of fullerene and non-fullerene acceptors to achieve highly efficient polymer solar cells. *J Mater Chem A.* 2019;7(26):15841-15850. doi:10.1039/C9TA04286E
146. Yuan M-C, Chiu M-Y, Chiang C-M, Wei K-H. Synthesis and Characterization of Pyrido[3,4- b ]pyrazine-Based Low-Bandgap Copolymers for Bulk Heterojunction Solar Cells. *Macromolecules.* 2010;43(15):6270-6277. doi:10.1021/ma100522a
147. Ye L, Zhang S, Zhao W, Yao H, Hou J. Highly Efficient 2D-Conjugated Benzodithiophene-Based Photovoltaic Polymer with Linear Alkylthio Side Chain. *Chem Mater.* 2014;26(12):3603-3605. doi:10.1021/cm501513n
148. Guo X, Zhou N, Lou SJ, et al. Bithiopheneimide–Dithienosilole/Dithienogermole Copolymers for Efficient Solar Cells: Information from Structure–Property–Device Performance Correlations and Comparison to Thieno[3,4- c ]pyrrole-4,6-dione Analogues. *J Am Chem Soc.* 2012;134(44):18427-18439. doi:10.1021/ja3081583
149. Yasa M, Toppare L. Thieno[3,4-c]pyrrole-4,6-dione-Based Conjugated Polymers for Nonfullerene Organic Solar Cells. *Macromol Chem Phys.* 2022;223(5):2100421. doi:10.1002/macp.202100421

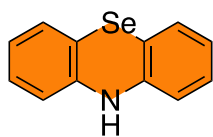


## APPENDICES

### A. Synthesis, Materials and Characterization

All chemicals and solvents were supplied by Tokyo Chemical Industry and Sigma Aldrich Chemical Co. Ltd. Toluene was dried over Na/benzophenone. N,N-dimethylformamide (DMF) was dried over barium oxides overnight followed by vacuum distillation. All reactions were carried out under nitrogen atmosphere unless otherwise specified. Merck Silica Gel 60 was used for purification of synthesized materials. Structural characterizations were performed by a Bruker Spectro Spin Avance DPX-400 spectrometer using trimethyl silane (TMS) as an internal reference in deuterated chloroform ( $\text{CDCl}_3$ ) and deuterated dimethyl sulfoxide (DMSO). High resolution mass spectra (HRMS) data were taken by Waters SYNAPT G1 with ESI-TOF-MS.

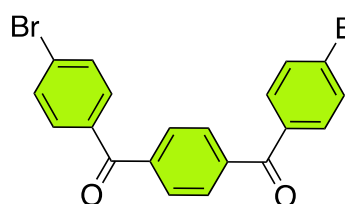
#### 10H-Phenoselenazine (1)



1

Diphenyl amine (10.00 g, 59.09 mmol), selenium dioxide (3.93 g, 35.5 mmol) and iodine (0.749 g, 2.95 mmol) were taken in a schlenk tube under inert atmosphere. The reaction medium was taken under inert atmosphere via nitrogen/vacuum cycles. A colloidal mixture of powdered selenium (2.33 g, 29.6 mmol) and sulfolene (10 mL) was added dropwise to the schlenk tube via a cannula. The reaction mixture was then stirred at 180 °C for 16 hours. Upon cooling to room temperature, the mixture was filtered through celite. The residue was washed sequentially with ethyl acetate (EtOAc), dichloromethane (DCM) and tetrahydrofuran (THF). The washings were combined, and the solvent was evaporated under reduced pressure. The crude product was purified by using column chromatography (Hexane:5/EtOAc:1, R<sub>f</sub>:0.43) followed by diffusion crystallization (chloroform-hexane) to yield the target compound as a gray powder (yield: 6.90 g, 48%). <sup>1</sup>H NMR (400 MHz, DMSO) δ (ppm) (ppm) 8.59 (s, 1H), 7.13 – 7.06 (m, 2H), 7.06 – 6.99 (m, 2H), 6.84 – 6.72 (m, 4H). <sup>13</sup>C NMR (100 MHz, DMSO) δ (ppm) (ppm) 142.0, 128.8, 127.8, 122.2, 115.1, 111.5.

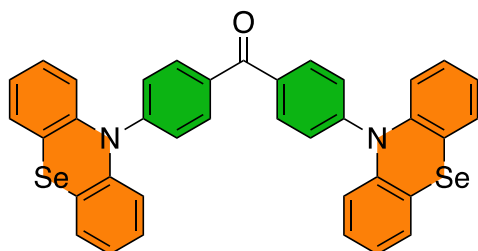
### 1,4-Bis (4-bromobenzoyl)-benzene (2)



**2**

Terephthaloyl chloride (2.60 g, 2.00 mmol) and bromobenzene (10 mL) were added to a Schlenk tube under inert atmosphere. Then, AlCl<sub>3</sub> (2.00 g, 14.9 mmol) was added portion wise to the mixture at room temperature. The reaction mixture was stirred for 9 hours and then heated to 90 °C for 2 hours. Then the mixture was cooled to room temperature and MeOH (100 mL) was added. The precipitates were collected by filtration and washed with MeOH. The attained white solids (yield: 2.90 g) were used without further purification.

### Bis(4-(10H-Phenoselenazin-10-yl)-phenyl)-methanone (SeDF-G)

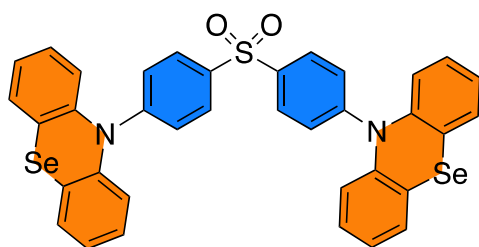


**SeDF-G**

Bis(4-bromophenyl)methanone (173 mg, 147 μmol), 10H-phenoselenazine (250 mg, 1.02 mmol), sodium tertbutoxide (245 mg, 2.54 mmol), tris(dibenzylideneacetone)dipalladium(0) (27.9 mg, 30.5 μmol) and tritert-butylphosphine (16.5 mg, 81.3 μmol) were introduced to a Schlenk tube under argon and dry toluene (7 mL) was added. The reaction temperature was raised to 125 °C and the reaction was followed using thin film chromatography. After 46 hours, the reaction mixture was cooled to room temperature and precipitated into 50 mL of cold MeOH. The yellow solid formed was filtered and was washed with cold MeOH. The crude product purified by using column chromatography (CHCl<sub>3</sub>/EtOAc/Petroleum ether, (1:1:2, R<sub>f</sub>:0.51) in silica and the crude product was recrystallized from (chloroform-methanol) to give the title compound as a yellow solid (90 mg, 82%). <sup>1</sup>H NMR (400 MHz, CDCl<sub>3</sub>) δ (ppm) 7.58 (d, *J* = 8.8 Hz, 4H), 7.53 (dd, *J* = 7.7, 1.1 Hz, 4H), 7.38 (d, *J* = 7.8 Hz, 4H), 7.28 (t, *J* = 7.3

Hz, 4H), 7.12 (t,  $J = 7.4$  Hz, 4H), 6.88 (d,  $J = 8.8$  Hz, 4H).  $^{13}\text{C}$  NMR (100 MHz,  $\text{CDCl}_3$ )  $\delta$  (ppm) 193.9, 148.9, 141.5, 131.8, 131.40, 130.7, 130.5, 127.7, 127.5, 126.3, 114.6. HRMS calcd. for  $(\text{C}_{37}\text{H}_{25}\text{N}_2\text{OSe}_2)$   $[\text{M} + \text{H}]^+$  : 673.0297; Found: 673.0297.

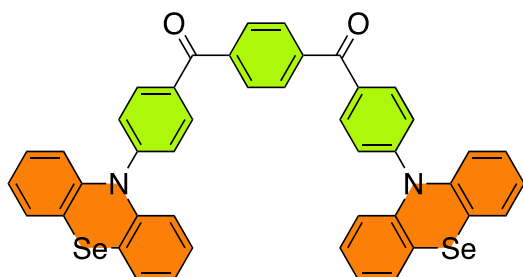
### 10,10'(sulfonylbis(4,1-phenylene))bis(10s-Phenoselenazine) (SeDF-B)



**SeDF-B**

10H-Phenoselenazine (145 mg, 590  $\mu\text{mol}$ ) and NaH (47 mg, 1.2 mmol) were added to a Schlenk tube under argon and dry DMF (3 mL) was added. The mixture was stirred at room temperature for 1 hour. Then, a solution of bis-(4-fluorophenyl)sulfone (75 mg, 295  $\mu\text{mol}$ ) in dry DMF (1 mL) was added to the reaction via a canula and the temperature was raised to 60  $^\circ\text{C}$ . The reaction was followed by using thin film chromatography. After 6 hours the reaction mixture was cooled to room temperature and diluted with water (200 mL). The mixture was extracted with chloroform (3x50 mL) and the combined organic phases were washed with brine (10x50 mL) and was dried over  $\text{Na}_2\text{SO}_4$ . The solvent was evaporated, and the crude product was purified using crystallization (chloroform-diethyl ether) followed by column chromatography (EtOAc/Hexane (2:3),  $R_f$ :0.62), and the product was obtained as a purple solid (yield:60 mg 28%).  $^1\text{H}$  NMR (400 MHz,  $\text{CDCl}_3$ )  $\delta$  (ppm) 7.57 – 7.50 (m, 8H), 7.41 (d,  $J = 7.5$  Hz, 4H), 7.32 – 7.27 (m, 4H), 7.14 (dd,  $J = 16.2, 8.7$  Hz, 4H), 6.78 (d,  $J = 8.9$  Hz, 4H).  $^{13}\text{C}$  NMR (100 MHz,  $\text{CDCl}_3$ )  $\delta$  (ppm) 149.60, 140.8, 132.7, 132.3, 131.7, 128.8, 128.40, 127.9, 126.9, 113.4. HRMS calcd. for  $(\text{C}_{36}\text{H}_{24}\text{N}_2\text{O}_2\text{SSe}_2)$   $[\text{M} + \text{H}]^+$  : 707.9889; Found: 707.9889.

**1,4-Phenylenebis((4-(10H-phenoselenazin-10-yl)phenyl)methanone) (SeDF-YG)**



**SeDF-YG**

1,4-Bis(4-bromobenzoyl)benzene (226 mg, 508  $\mu\text{mol}$ ), 10H-phenoselenazine (250 mg, 1.02 mmol), sodium tertbutoxide (245 mg, 2.54 mmol), tris (dibenzylideneacetone)dipalladium(0) (27.9 mg, 30.5  $\mu\text{mol}$ ) and tritert-butylphosphine (16.5 mg, 81.3  $\mu\text{mol}$ )

were introduced to a Schlenk tube under argon and dry toluene (7 mL) was added. The reaction temperature was raised to 125 °C and the reaction was followed using thin film chromatography. After 46 hours, the reaction mixture was cooled to room temperature and precipitated into 50 mL of cold MeOH. The yellow solid formed was filtered and was washed with cold MeOH. The crude product purified by using column chromatography ( $\text{CHCl}_3/\text{EtOAc}/\text{Petroleum ether}$ , (1:1:1, Rf:0.50) in silica and the crude product was recrystallized from (chloroform-diethyl ether) to give the title compound as a yellow solid (32 mg, 82%).  $^1\text{H NMR}$  (400 MHz,  $\text{CDCl}_3$ )  $\delta$  (ppm) 8.12 (d,  $J = 8.5$  Hz, 4H), 7.77 (d,  $J = 8.5$  Hz, 4H), 7.68 (d,  $J = 9.1$  Hz, 8H), 7.59 (dd,  $J = 7.9, 1.2$  Hz, 4H), 7.43 (td,  $J = 7.5, 1.4$  Hz, 4H), 7.26 (td,  $J = 7.6, 1.3$  Hz, 4H), 6.95 (d,  $J = 9.1$  Hz, 4H).  $^{13}\text{C NMR}$  (100 MHz,  $\text{CDCl}_3$ )  $\delta$  (ppm) 194.1, 166.3, 150.0, 142.4, 140.8, 132.1, 131.5, 129.2, 129.1, 128.3, 127.7, 126.7, 112.8. HRMS calcd. for ( $\text{C}_{44}\text{H}_{28}\text{N}_2\text{O}_2\text{Se}_2$ )  $[\text{M} + \text{H}]^+$  : 776.0486; Found: 776.0486.



## B. Computational Studies

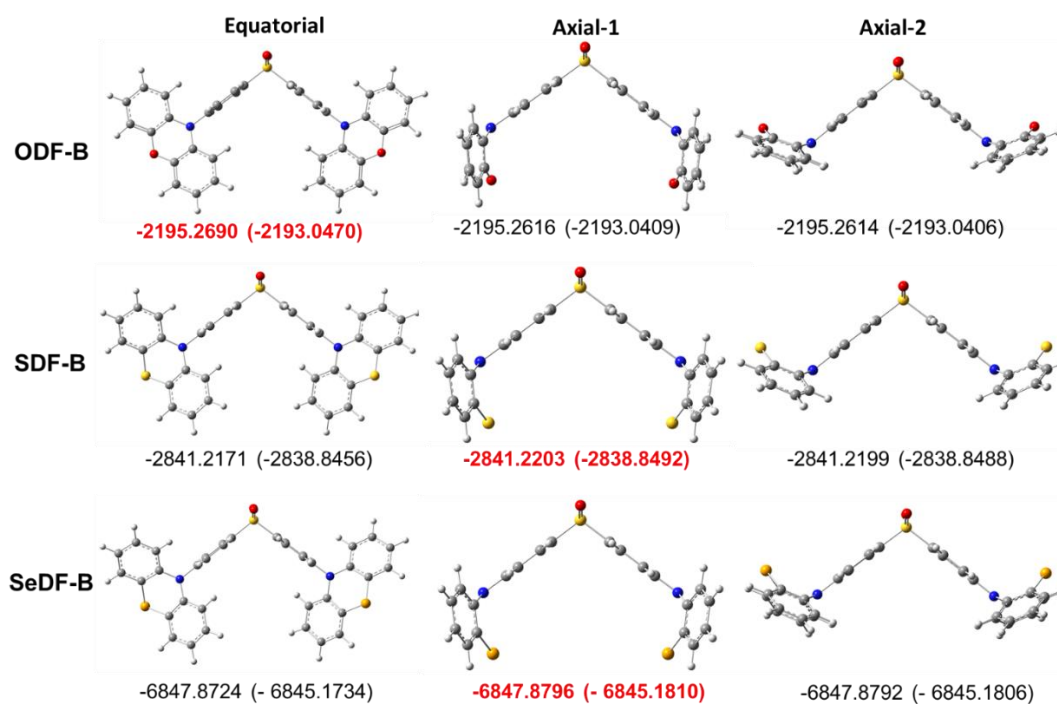


Figure A1. Total energy comparison for (O-S-Se)-DF-B structures in equatorial and axial conformation at B3LYP/6-311+(d,p). PBE0 functional based calculation results were given in parenthesis.

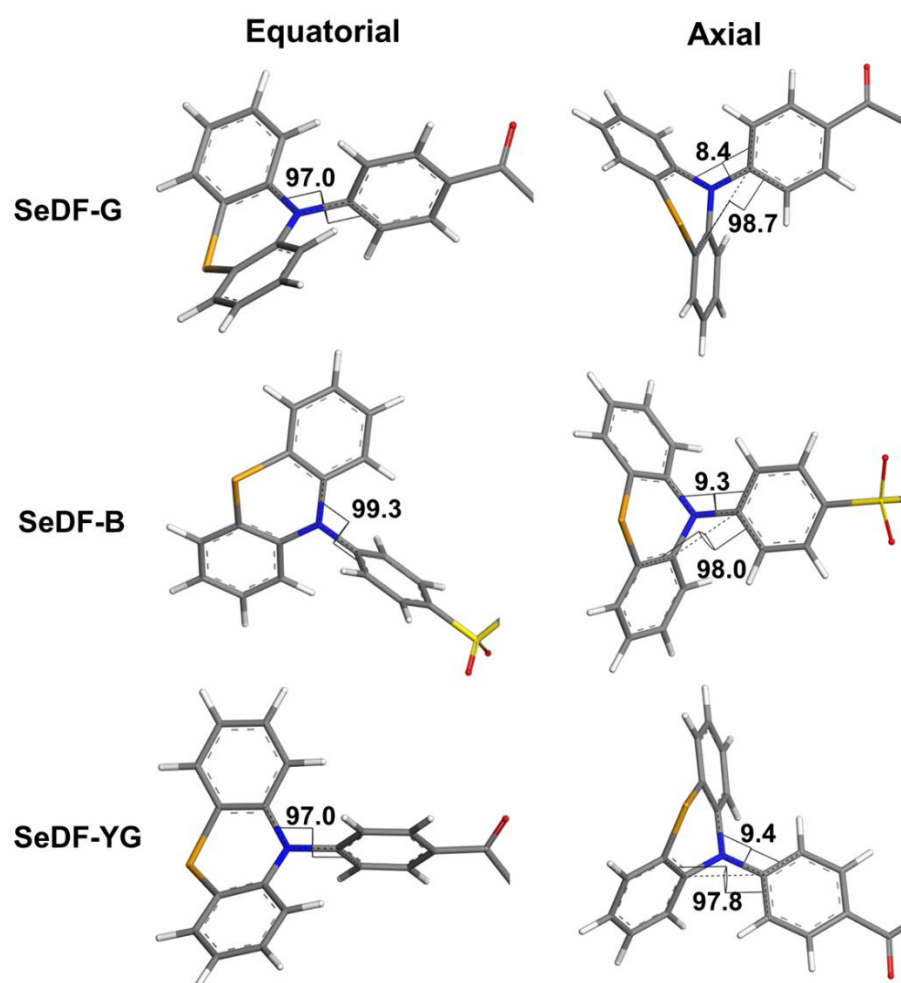


Figure A2. Dihedral angles between donor and acceptor units for two lowest energy conformations of SeDF-G, SeDF-B and SeDF-YG TADF materials.

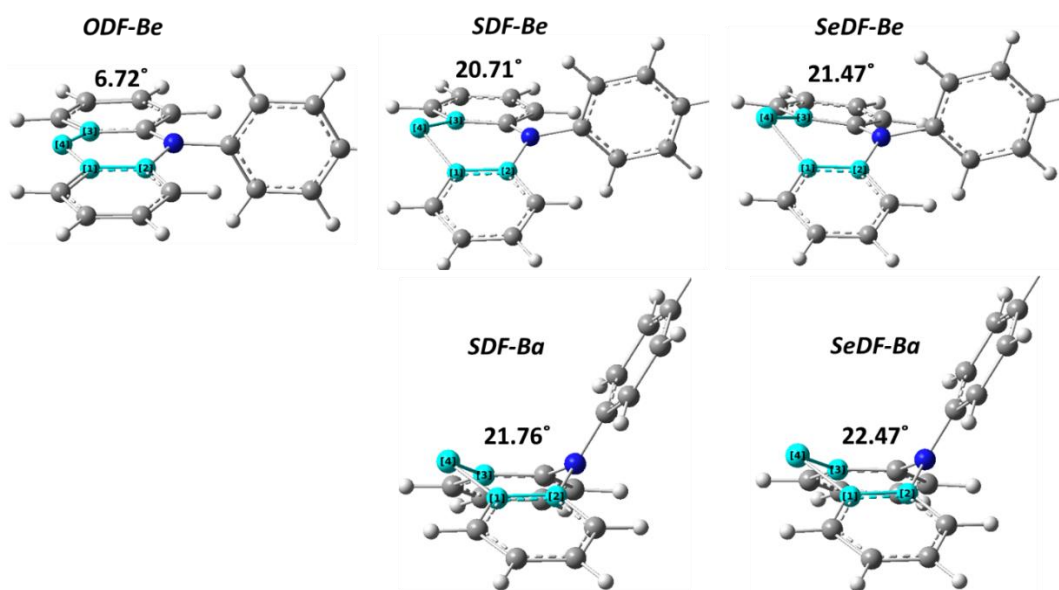


Figure A3. The dihedral angle of O-S-Se atoms with respect to the aromatic plane for equatorial and axial conformations.

Table A1. The percentage of LUMO and HOMO on acceptor unit at the center calculated by Mulliken molecular orbital composition method.

	<b>HOMO %</b>	<b>LUMO %</b>
<b>O-DF-Be</b>	0.25	98.46
<b>S-DF-Be</b>	2.67	97.45
<b>S-DF-Ba</b>	45.37	48.34
<b>Se-DF-Be</b>	3.61	96.33
<b>Se-DF-Ba</b>	47.29	44.03
<b>Se-DF-G</b>	45.90	83.37
<b>Se-DF-YG</b>	43.94	95.90

Table A2. HOMO and LUMO energy levels, first vertical singlet and triplet excitations, S1-T1 intersystem crossing energy values calculated by using B3LYP, PBE0 and CAM-B3LYP functionals and different basis sets.

<b>B3LYP</b>					
<b>6-311g(d,p)</b>					
	<b>HOMO</b>	<b>LUMO</b>	<b>S<sub>0</sub>-S<sub>1</sub></b>	<b>S<sub>0</sub>-T<sub>1</sub></b>	<b>ISC (S<sub>1</sub>-T<sub>1</sub>)</b>
SeDF-Ge	-5.34	-2.36	2.51	2.49	0.01
SeDF-Ga	-5.54	-1.38	3.59	2.85	0.74
SeDF-B	-5.45	-2.10	2.81	2.78	0.03
SeDF-YG	-5.55	-2.71	2.27	2.27	0.01
<b>PBE</b>					
<b>6-311g(d,p)</b>					
SeDF-Ge	-5.56	-2.23	2.72	2.69	0.02
SeDF-Ga	-5.76	-1.26	3.73	2.83	0.86
SeDF-B	-5.67	-1.98	2.99	2.91	0.08
SeDF-YG	-5.57	-2.58	2.52	2.51	0.01
<b>B3LYP</b>					
<b>6-311+g(d,p)</b>					
SeDF-Ge	-5.44	-2.50	2.46	2.45	0.01
SeDF-Ga	-5.64	-1.52	3.33	2.85	0.48
SeDF-Be	-5.54	-2.21	2.79	2.76	0.03
SeDF-B	-5.73	-1.30	3.47	3.20	0.27
SeDF-YG	-5.53	-2.25	2.73	2.71	0.02
<b>PBE0</b>					
<b>6-311+g(d,p)</b>					
SeDF-Ge	-5.64	-2.35	2.67	2.65	0.02
SeDF-Ga	-5.85	-1.35	3.31	2.85	0.46
SeDF-Be	-5.74	-2.10	2.93	2.87	0.06
SeDF-Ba	-5.94	-1.14	3.38	3.15	0.23
SeDF-YG	-5.98	-1.14	3.38	3.15	0.24
<b>B3LYP</b>					
<b>6-311++g(d,p)</b>					

SeDF-Ge	-5.44	-2.50	2.46	2.45	0.01
SeDF-Ga	-5.63	-1.55	3.53	2.84	0.68
SeDF-B	-5.54	-2.21	2.79	2.76	0.03
SeDF-YG	-5.45	-2.85	2.23	2.23	0.01
<b>PBE0</b>					
<b>6-311++g(d,p)</b>					
SeDF-Ge	-5.64	-2.35	2.67	2.65	0.02
SeDF-Ga	-5.84	-1.40	3.68	2.82	0.85
SeDF-B	-5.74	-2.08	2.97	2.89	0.08
SeDF-YG	-5.65	-2.71	2.47	2.46	0.01
<b>CAM-B3LYP</b>					
<b>6-311++g(d,p)</b>					
SeDF-Ge	-6.77	-1.28	3.69	3.02	0.67
SeDF-Ga	-6.97	-0.40	4.13	2.92	1.21
SeDF-B	-6.88	-1.03	3.80	3.07	0.74
SeDF-YG	-6.78	-1.65	3.63	2.87	0.76

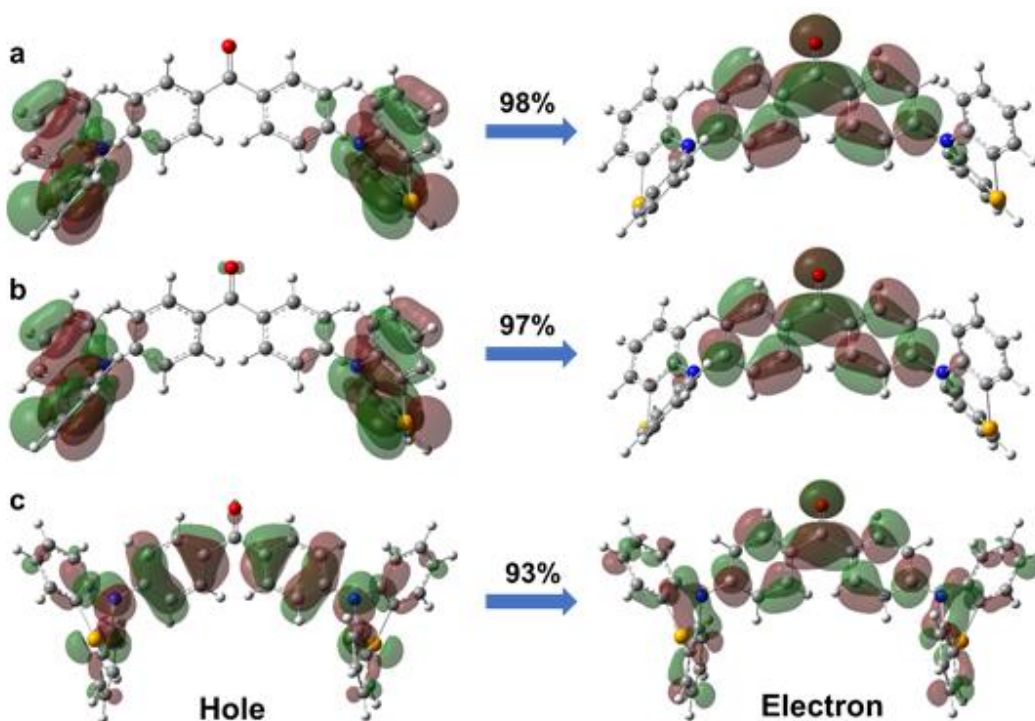


Figure A4. Natural transition orbitals (NTO) from HOMO to LUMO corresponding to the first singlet transition S0-S1 (a) and first triplet transition S0-T1 of equatorial SeDF-G (b) and first singlet S0-S1 excitation for axial SeDF-G (c). Hole refers to the highest occupied natural transition orbital and electron refers to the lowest unoccupied natural transition orbital. Similar results are valid for SeDF-B and SeDF-YG.

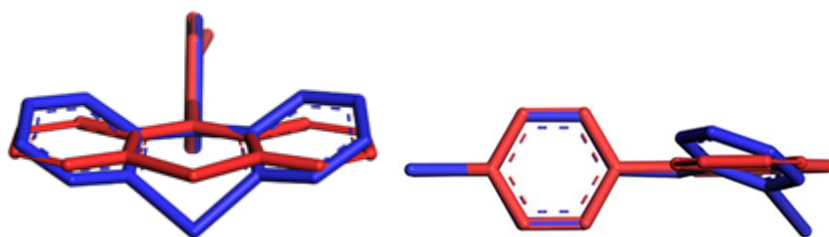


Figure A5. Improved planarity of the of the side group in the first singlet excited state optimized geometry observed for equatorial conformer.

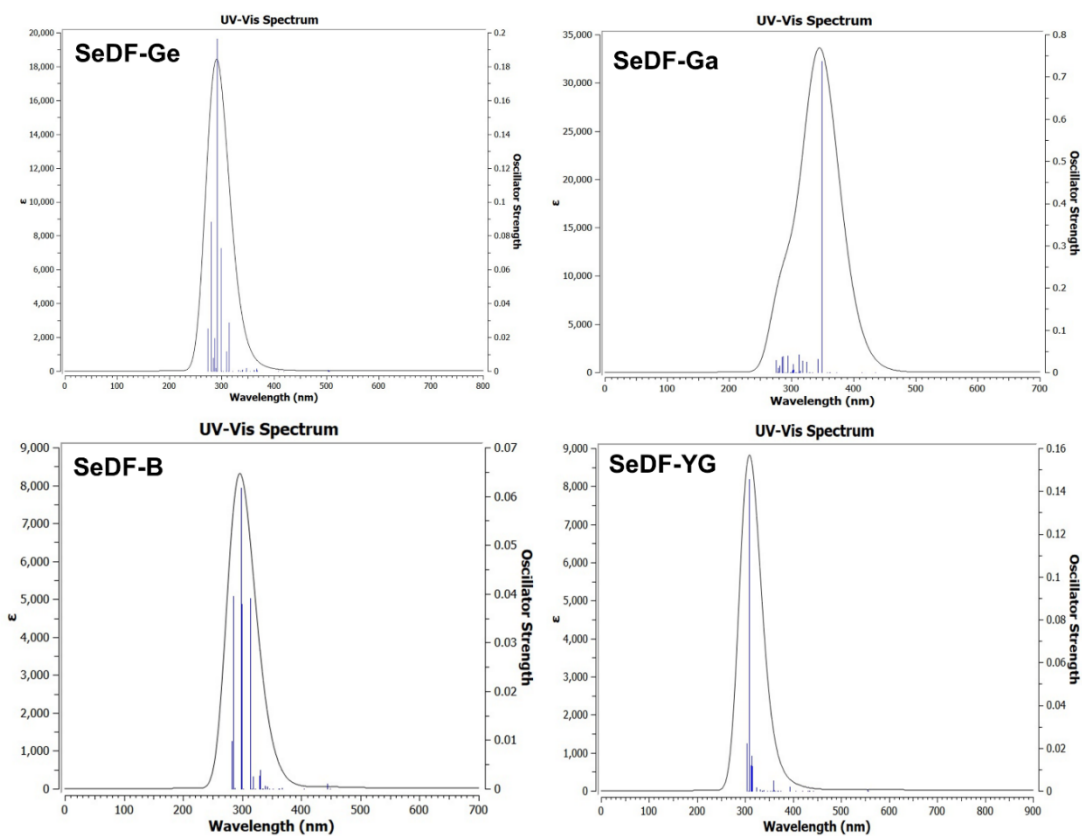


Figure A6. UV-Vis plot that demonstrated higher oscillator strength and molar absorption coefficient ( $\epsilon$ ) for the SeDF-G for both equatorial and axial conformations.

### C. Device Fabrication and Characterization

Table S4: PLQYs of equivalent films (10% TADF emitter in m-CBP host, under nitrogen in integrating sphere with 330 nm excitation)

Emitter	PLQY (%)
SeDF-G	7.6
SeDF-YG	8.5
SeDF-B	2.6

## Device Performance

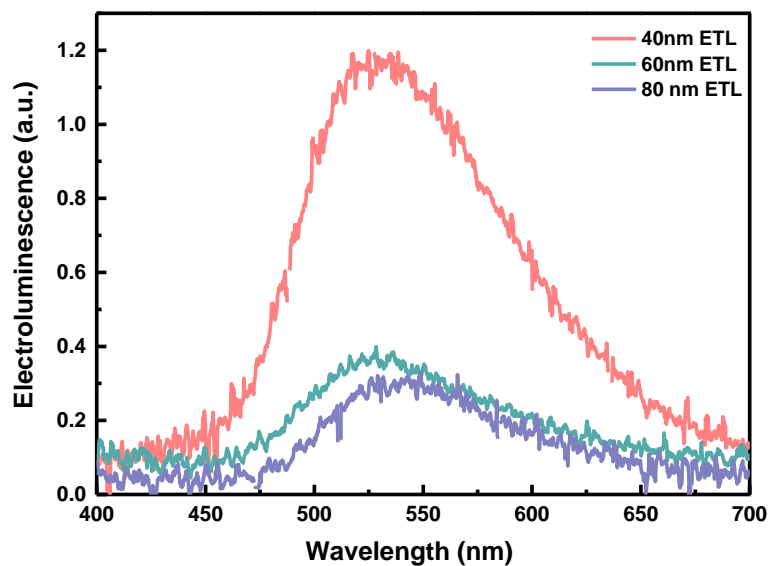


Figure A7. Electroluminescence vs wavelength graph for different ETL thicknesses with a device structure of ITO/NPD/m-CBP:SeDF-G/TPBi/LiF/Al.



## D. NMR Spectra

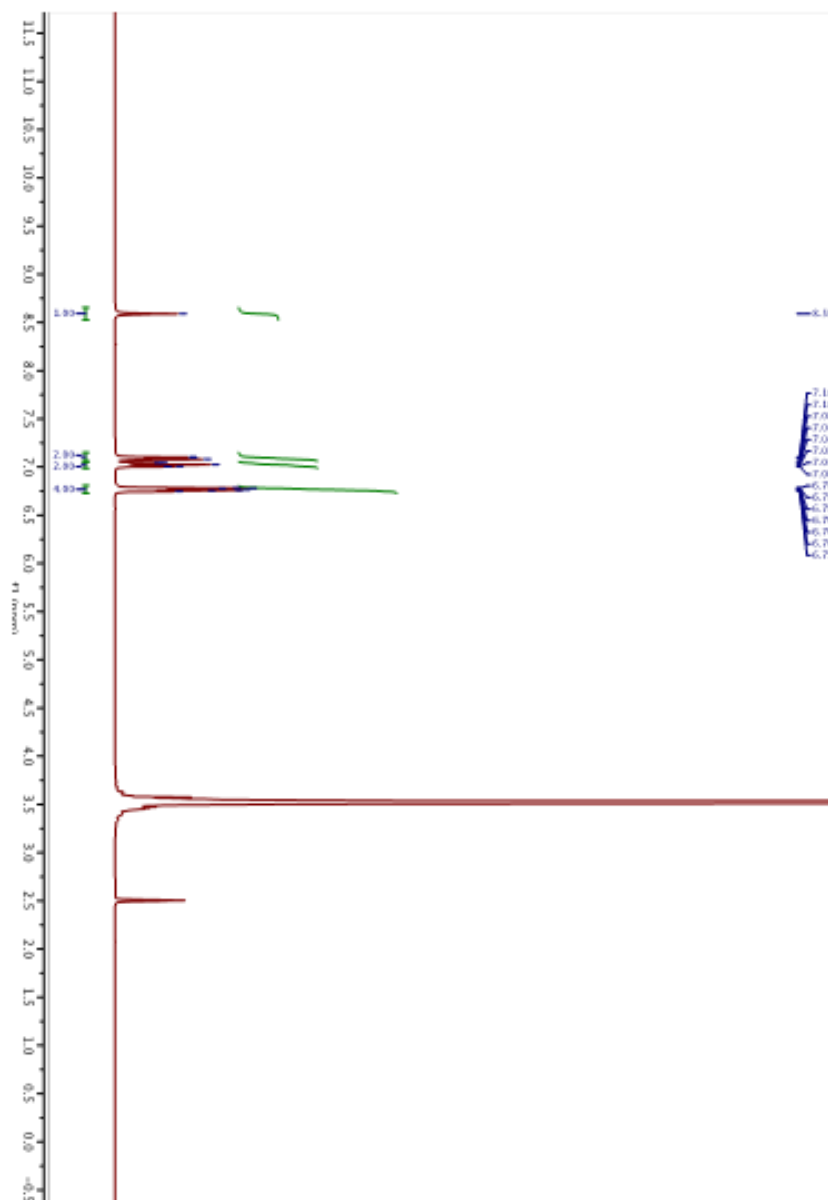


Figure A8.  $^1\text{H-NMR}$  Spectrum of Compound 1.

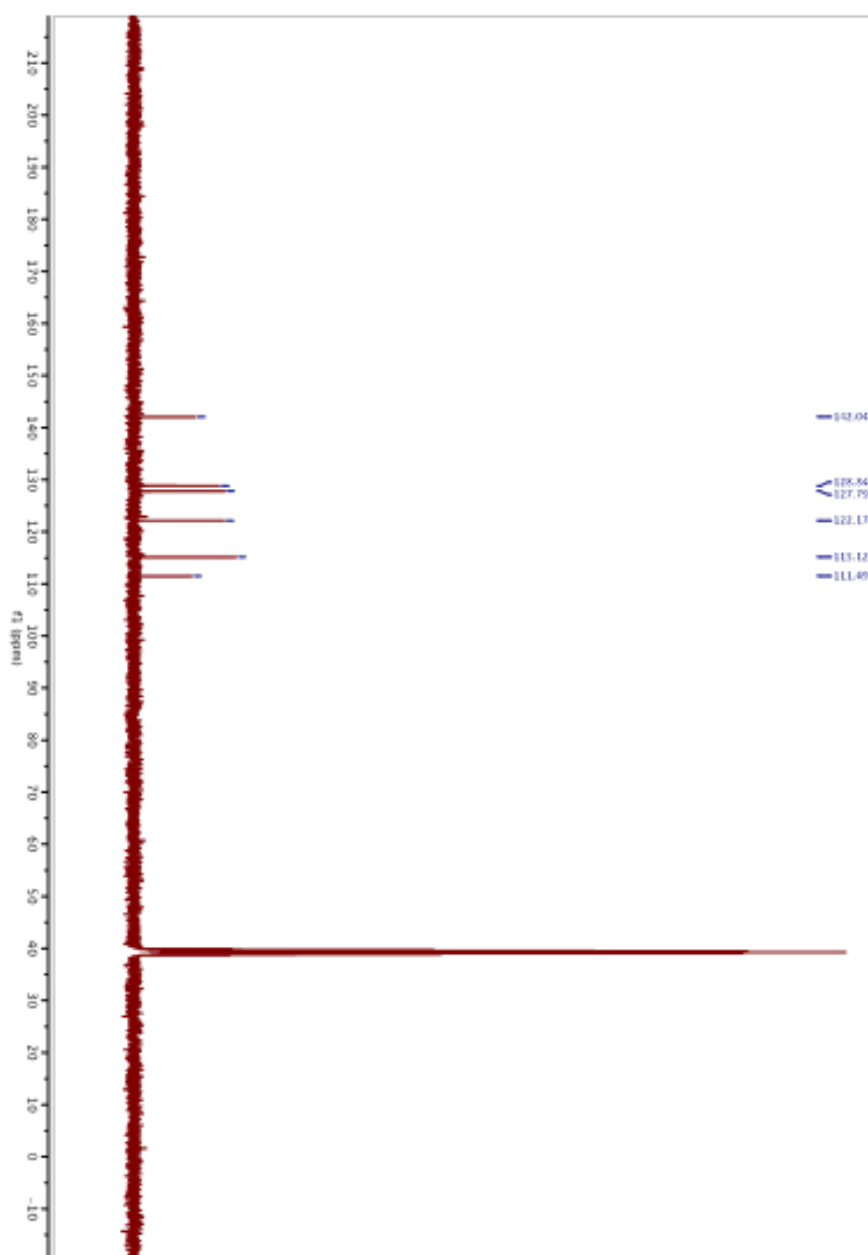


Figure A9.  $^{13}\text{C}$ -NMR Spectrum of Compound 1.

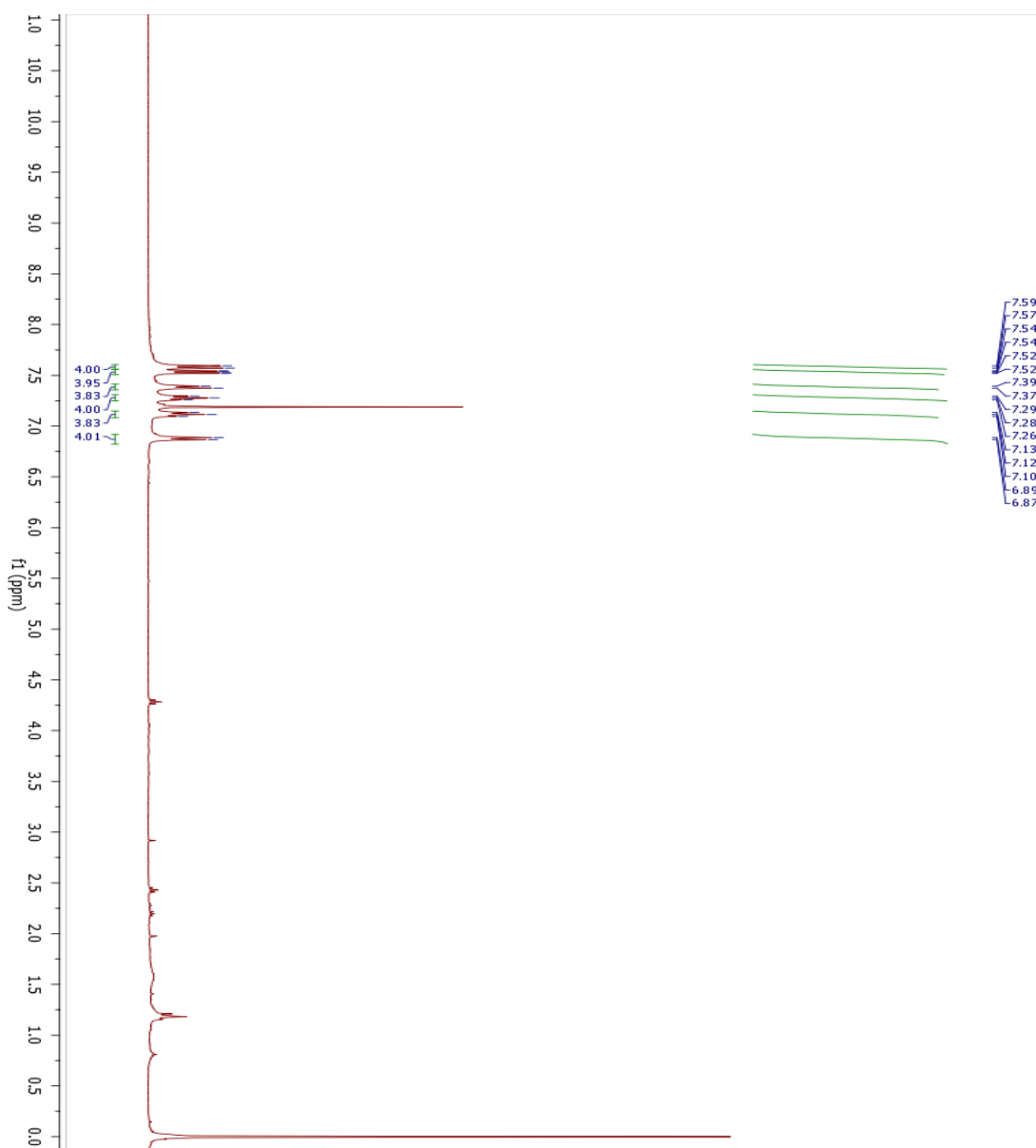


Figure A10.  $^1\text{H-NMR}$  Spectrum of Compound SeDF-G.

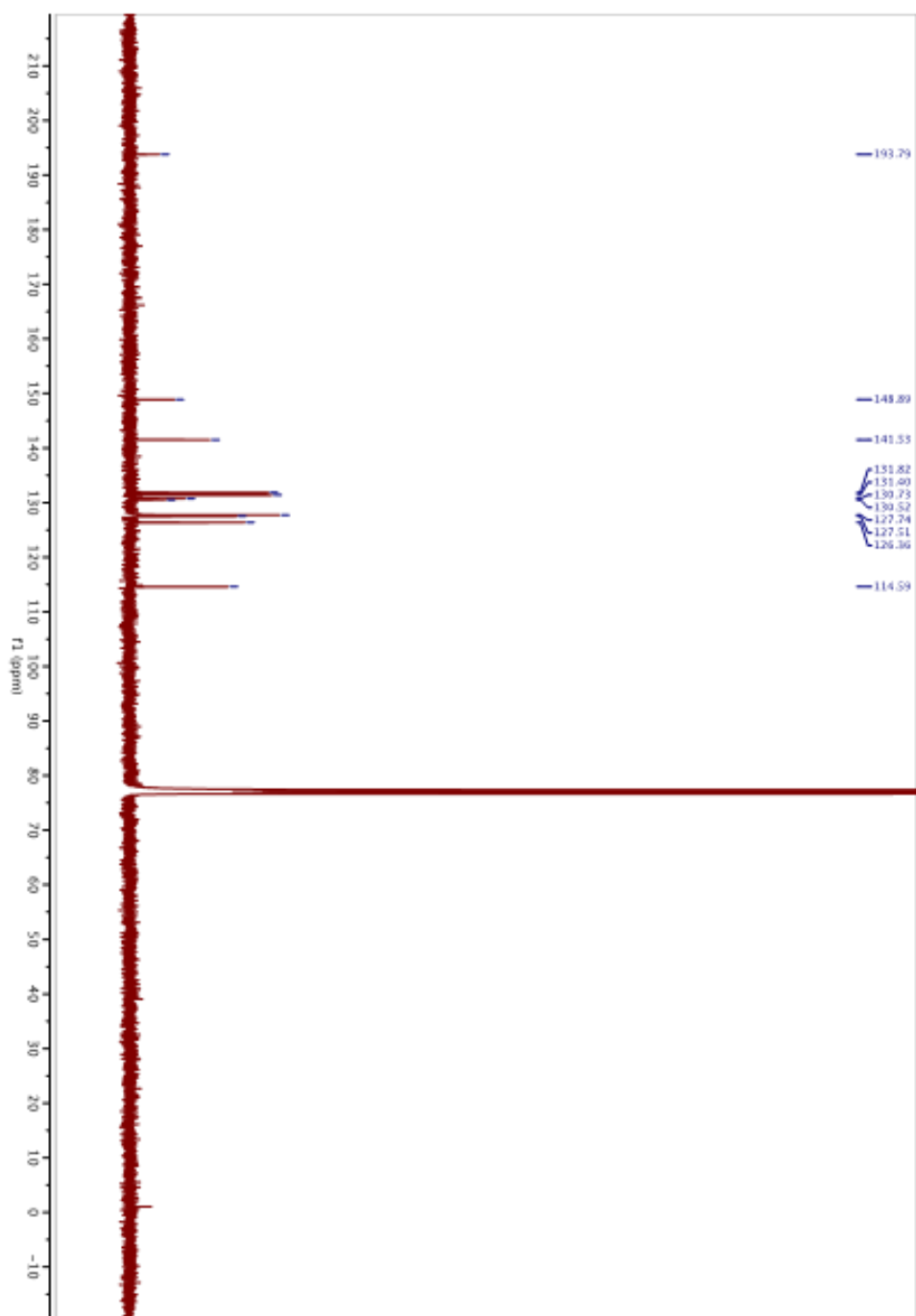


Figure A11.  $^{13}\text{C}$ -NMR Spectrum of Compound SeDF-G.

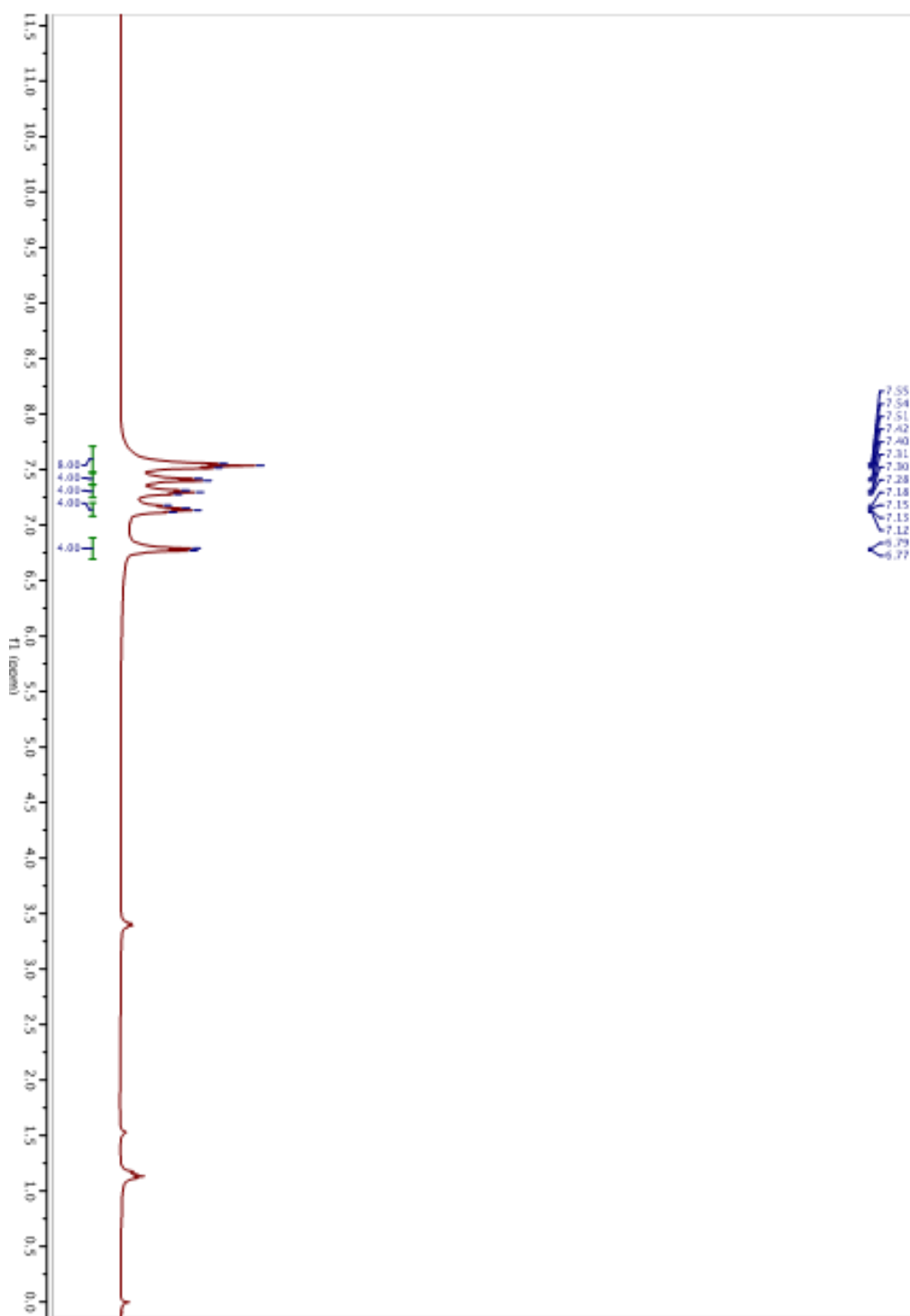


Figure A12.  $^1\text{H}$ -NMR Spectrum of Compound SeDF-B.

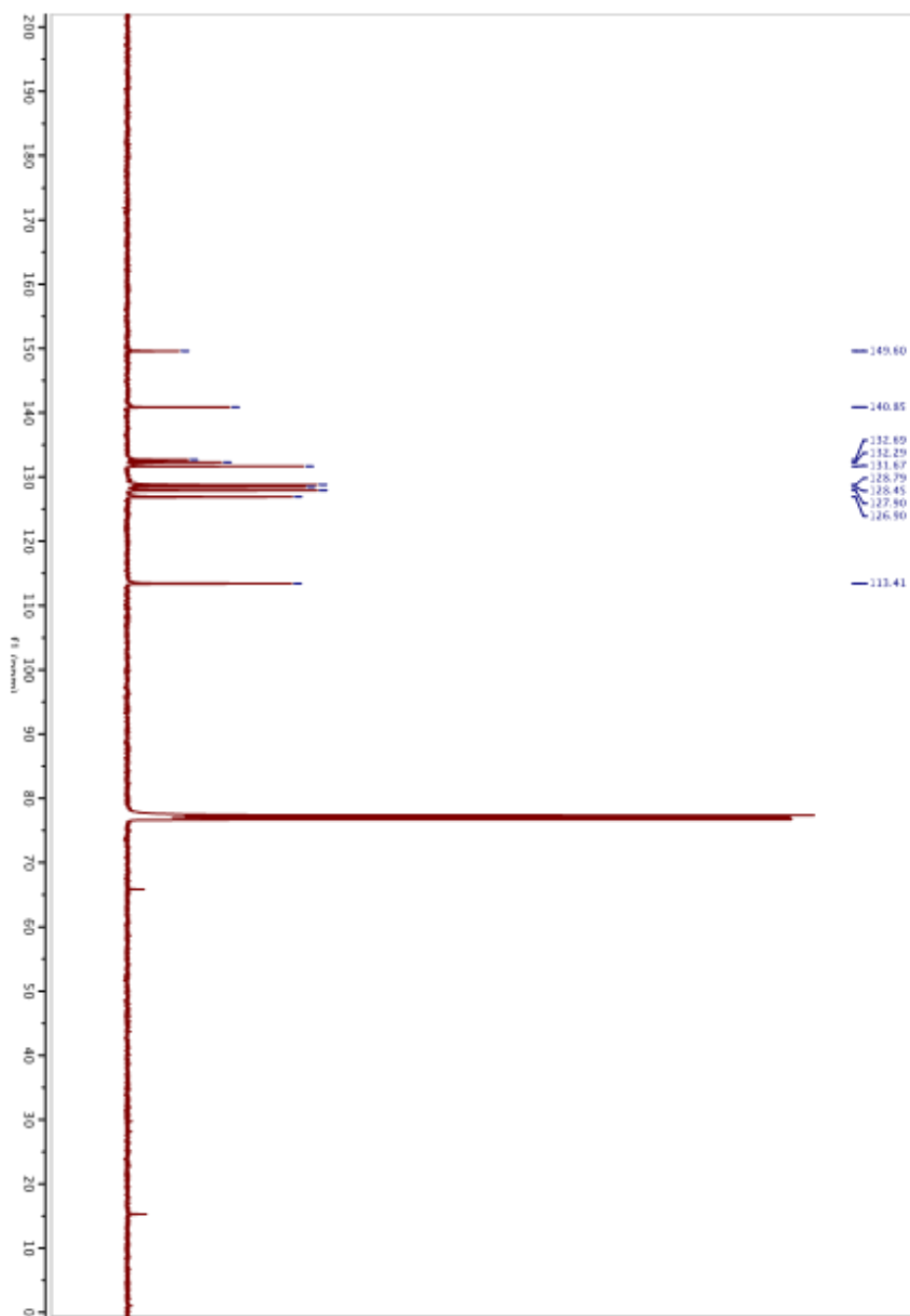


Figure A13.  $^{13}\text{C}$ -NMR Spectrum of Compound SeDF-B.

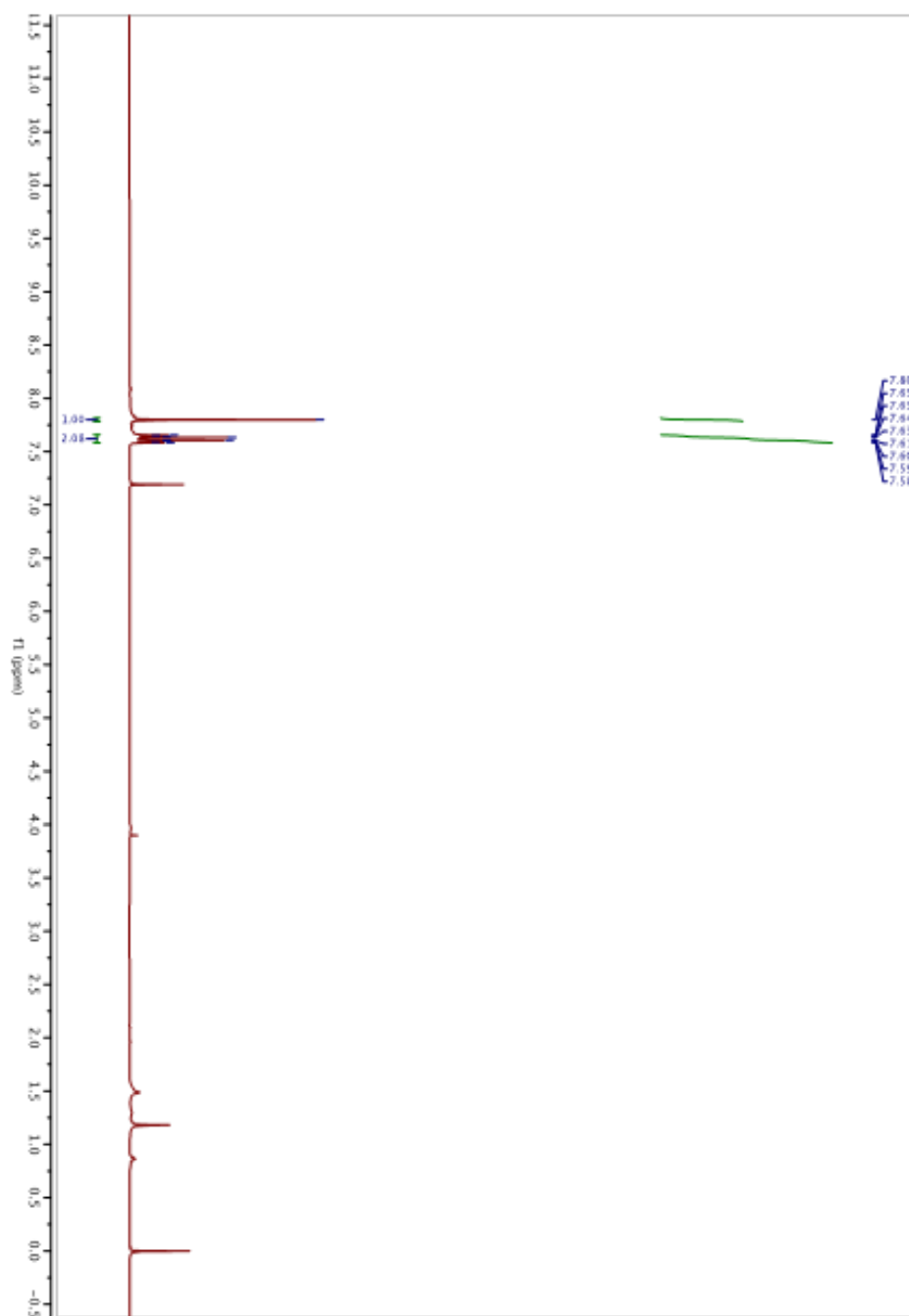


Figure A14.  $^1\text{H-NMR}$  Spectrum of Compound 2.

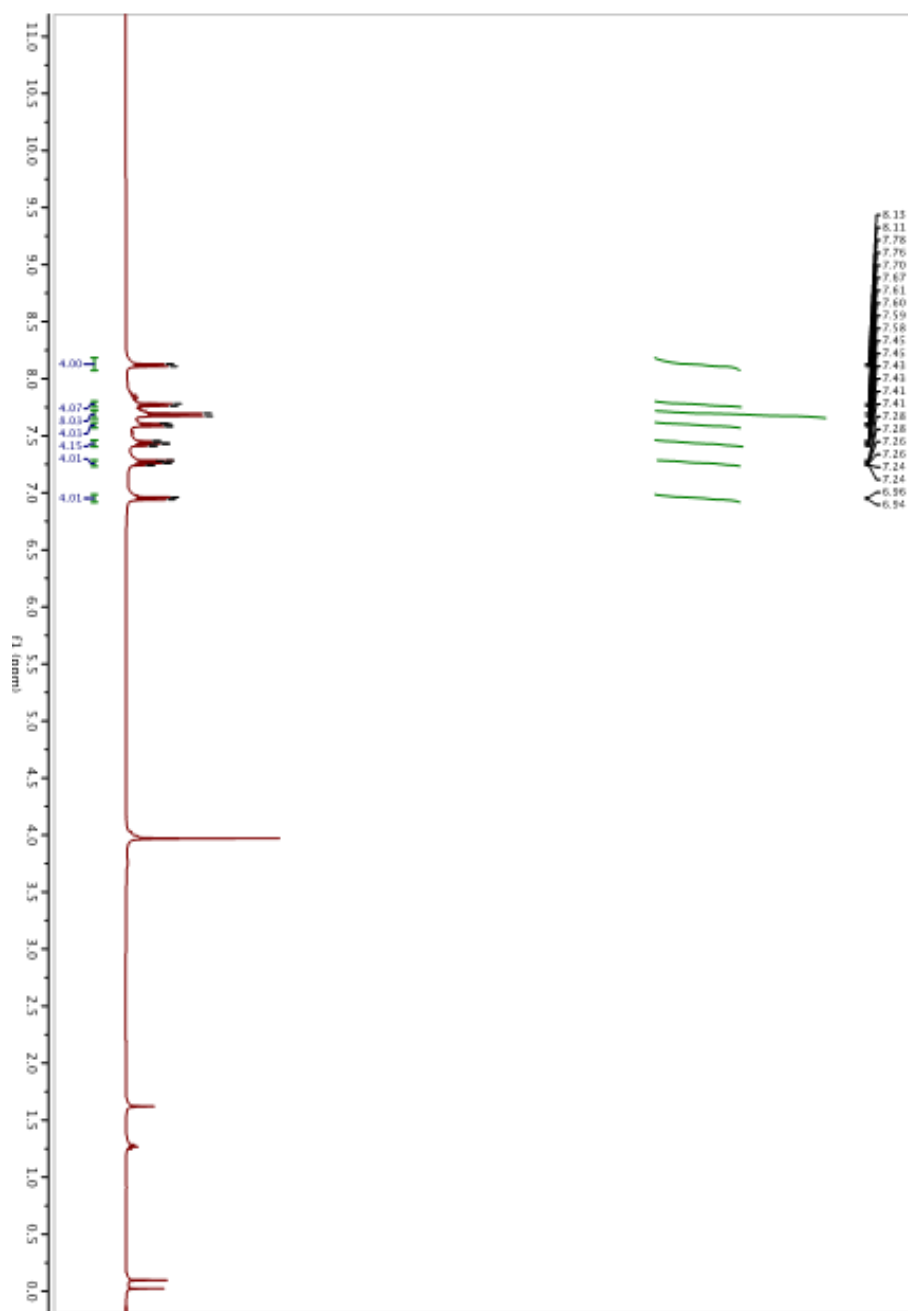


Figure A15.  $^1\text{H-NMR}$  Spectrum of Compound SeDF-YG.



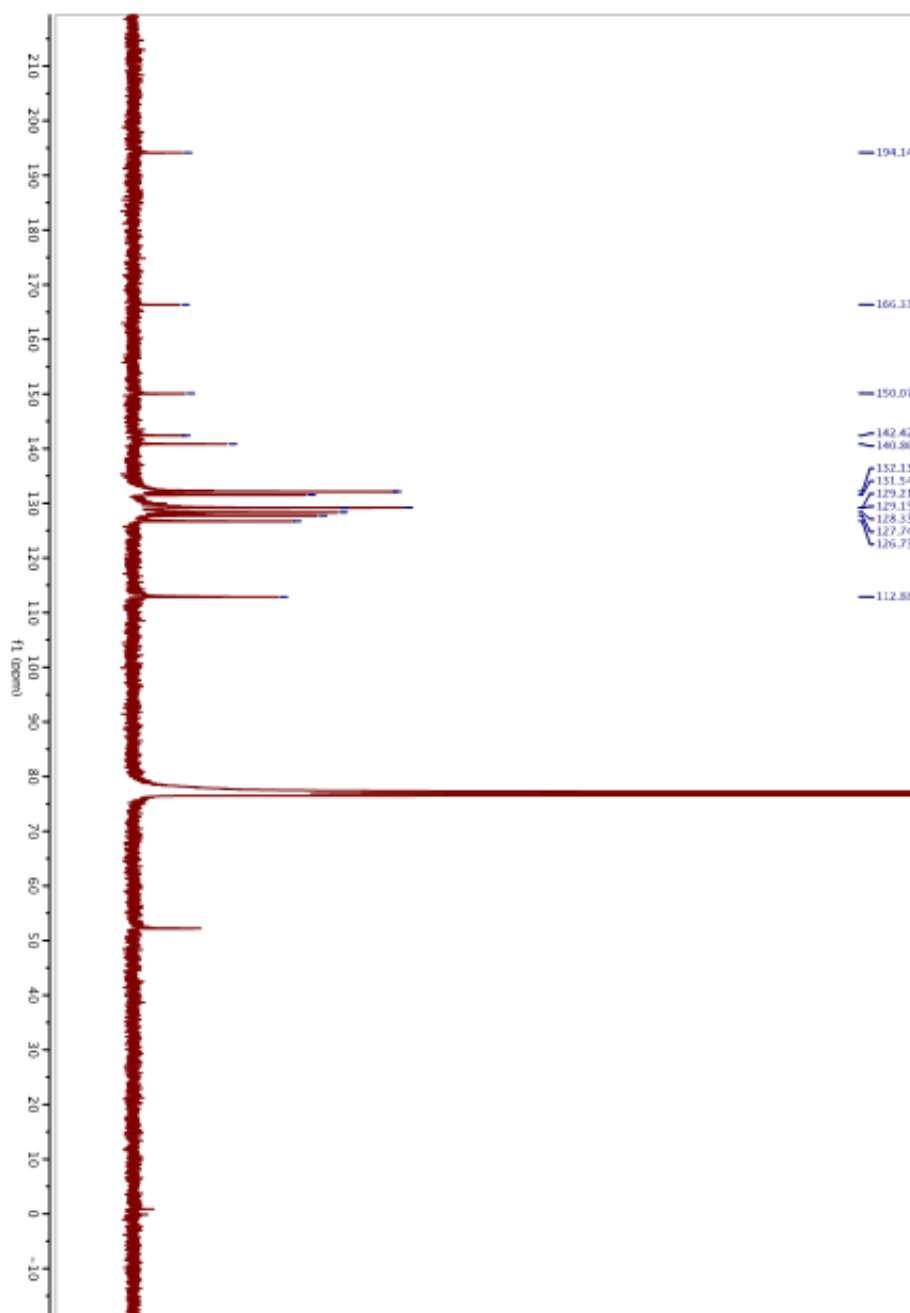


Figure A16.  $^{13}\text{C}$ - NMR Spectrum of Compound SeDF-YG.

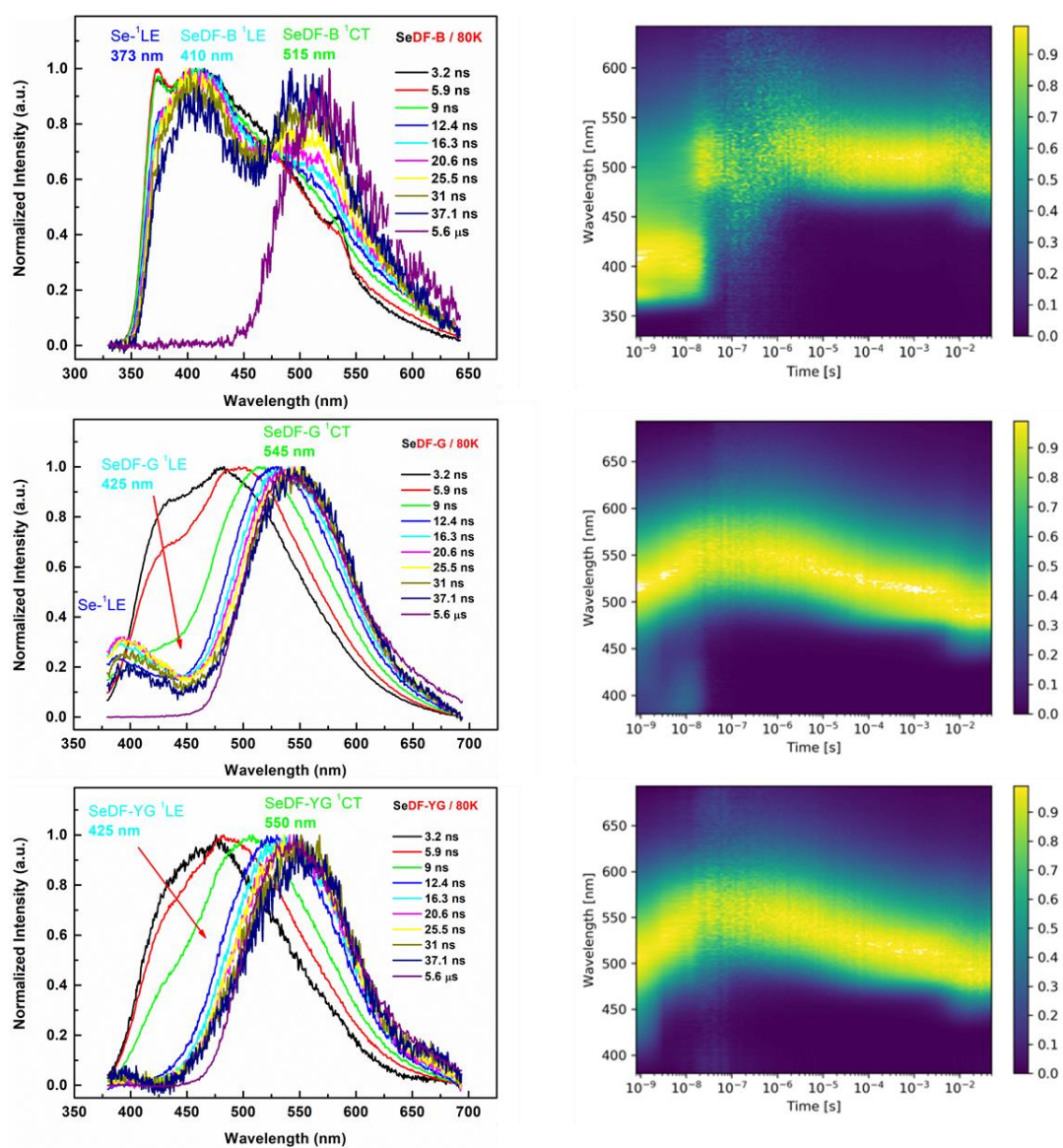


Figure A17. Normalized time-resolved spectral evolution of the molecules at 80K

## CURRICULUM VITAE

Surname, Name :Alemdar Yılmaz, Eda  
Nationality :Turkish (T.C.)  
e-mail

### EDUCATION

Degree	Institution	Year of Graduation
MS	METU Chemistry	2017
BS	METU Chemistry	2015
High School	Özel Düzce Fatih Anadolu Lisesi	2007

### WORK EXPERIENCE

Research Assistant in Chemistry Department (2015-2023)

### FOREIGN LANGUAGE

Advanced English

### PUBLICATIONS

1. **Eda Alemdar**, Parisa Sharif, Soner Ozturk, Omer Caylan, Tugba Hacıfendioglu, Goknur Buke, Murat Aydemir, Andrew Danos, Andrew P. Monkman, Erol Yildirim, Gorkem Gunbas, Ali Cirpan, Ahmet Oral, Rational Molecular Design Enables Efficient Blue TADF–OLEDs with Flexible Graphene Substrate. *Adv. Funct. Mater.* (2022), 32, 2207324.
2. Oguzhan Karakurt, **Eda Alemdar**, Mert Can Erer, Duygu Cevher, Selin Gulmez, Umut Taylan, Sevki Can Cevher, Gonul Hizalan Ozsoy, Bulend

- Ortac, Ali Cirpan, Boosting the efficiency of organic solar cells via plasmonic gold nanoparticles and thiol functionalized conjugated polymer, *Dyes and Pigments*, 208, (2022), 110818,
3. Mustafa Yasa, Tolga Depci, **Eda Alemdar Yilmaz**, Serife Ozdemir Hacioglu, Ali Cirpan, Levent Toppare, Non-fullerene organic photovoltaics based on thienopyrroledione comprising random copolymers; effect of alkyl chains, (2021), *Renewable Energy*, 178, 202-211
  4. Sevki Can Cevher, Gonus Hizalan, **Eda Alemdar Yilmaz**, Duygu Cevher, Yasemin Udum Arslan, Levent Toppare, Erol Yildirim, Ali Cirpan, (2020). A comprehensive study: Theoretical and experimental investigation of heteroatom and substituent effects on frontier orbitals and polymer solar cell performances. *Journal of Polymer Science*, 58(19), 2792-2806.
  5. Gulden Ozkul Atli, **Eda Alemdar Yilmaz**, Sultan Taskaya Aslan, Yasemin Udum, Levent Toppare, Ali Çirpan, (2020). Synthesis and characterization of optical, electrochemical and photovoltaic properties of selenophene bearing benzodithiophene based alternating polymers. *Journal of Electroanalytical Chemistry*, 862, 114014.
  6. **Eda Alemdar**, Mustafa Yasa, Ali Cirpan, Levent Toppare, Molecular design and theoretical characterization of benzodithiophene and quinoxaline based conjugated polymers for organic solar cells, Submitted to *Journal of Electroanalytical Chemistry*

#### **ACADEMIC CONFERENCES**

1. Polimer2018, Poster, Eskişehir, Turkey  
**Eda Alemdar**-Duygu Güven-Şevki Can Cevher-Eda Bolayır-Gönül Hizalan-Şerife O. Hacıoğlu-Levent Toppare-Ali Çirpan  
Benzodithiophene Bearing Polymers- Synthesis and Electrochemical Studies
2. PVCON2018, Poster, Ankara, Turkey

**Eda Alemdar**-Şevki Can Cevher-Gönül Hızalan-Şerife O. Hacıoğlu-Levent Toppare-Ali Çırpan

Bistriphenylamine- and Benzodithiophene- Based Random Conjugated Polymers in Ternary Blend Bulk Heterojunction Organic Solar Cells

3. PVCON2020, **Oral Presentation**, Ankara, Turkey

**Eda Alemdar Yılmaz**-Parisa Sharif-Görkem Günbaş-Ahmet Oral-Ali Çırpan

Efficient Green OLEDs based on Thermally Activated Delayed Fluorescence Butterfly-shape Emitter

4. NANOTR16, **Oral Presentation**, Ankara, Turkey

Eda Alemdar, Sevki Can Cevher, Duygu Cevher, Ali Cirpan

Effect of Fluorination Strategy and Side Chain Engineering on the Performance of Organic Solar Cells